

Copyright

by

David Birkett Haines

2021

The Dissertation Committee for David Birkett Haimes Certifies that this is the approved version of the following Dissertation:

The Interrogation of Auditory Activity and Molecular Genetics on the Development of Sound Localization Neurons

Committee:

Nace L. Golding, Supervisor

Richard Aldrich

Harold Zakon

Darrin Brager

**The Interrogation of Auditory Activity and Molecular Genetics on the
Development of Sound Localization Neurons**

by

David Birkett Haimes

Dissertation

Presented to the Faculty of the Graduate School of
The University of Texas at Austin
in Partial Fulfillment
of the Requirements
for the Degree of

Doctor of Philosophy

The University of Texas at Austin

August 2021

Dedication

I dedicate this body of work to my late father, Joel Bernard Haimes, who we lost in December of 2014. He inspired me as a coach, musician, and amazing father. Dad I wish you were here to see the end of my graduate school career, and to share in all the things that have happened since you passed. It's had its ups and downs, and I miss your unwavering support most of all. I love you and I miss you.

What a Long Strange Trip It's Been...

Acknowledgements

I would like to acknowledge all the people that have helped me get to where I am today, including those that are no longer with us. My family has been beside me every step of the way, my mother Jill has held our family together through everything, and my wonderful sisters, Cari and Andrea, who have always supported and cheered me on, even when they have no idea what my work is about. All of my friends along the way, from high school, college, and graduate school have always been there, in times of joy and sadness. I would also like to thank all my mentors in biology, but especially, Nela Breitreutz, Ken Belanger, Nace Golding, and Darrin Brager. The latter of whom went above and beyond throughout my graduate school career to help provide feedback on everything from experimental design, to writing and figure advice whenever I needed it. They have helped shaped the scientist I am today – thank you.

Lastly, I would like to acknowledge my wonderful fiancé, Elle Roberson, who has shared every step of my journey with me. She has provided every possible type of support imaginable throughout this bumpy ride: from emotional support, to scientific feedback, to gastrointestinal support with her endless baked goods. I love you dearly and cannot wait to be married to you!

Abstract

The Interrogation of Auditory Activity and Molecular Genetics on the Development of Sound Localization Neurons

David Birkett Haimes, Ph.D.
The University of Texas at Austin, 2021

Supervisor: Nace L. Golding

The body of work presented here is a series of manuscripts in varying states of publication that represent the work performed by the author. In brief, these works have focused on unraveling on a cellular level how the auditory brain builds a spatial map of one's environment discretely from sound stimuli which fundamentally lack spatial information. Neurons in the brain region known as the Medial Superior Olive (MSO) integrate differences in the arrival time of sound stimuli between two ears, while neurons in the Lateral Superior Olive (LSO) integrate differences in the intensity of sound stimuli. Cells in both regions use their unique strategies to compute spatial information, split based on the frequency of incoming sound. In the manuscripts presented here (Chapter 4), we demonstrate that neurons in the LSO do not strictly adhere to previous historical dogma (use of predominantly high frequency sounds), and instead show exquisite temporal resolution more like MSO neurons. Specifically, our work demonstrates a neural "vetoing" mechanism in which spatially precise inhibition overrides the integration of somatodendritic excitatory signals due to its localization on the axon initial segment of neurons. For the remaining work (Chapters 3 & 5), we discuss how MSO neurons exhibit a continuum of response properties, ranging from neurons with exquisite temporal precision, to neurons with incredibly slow properties that are poor coincidence detectors. These slow MSO neurons were previously assumed to be non-principal neurons, but throughout this body of work we demonstrate that all MSO neurons are principal neurons that exist along a continuum of firing response properties and all project to downstream auditory centers. Furthermore, we deeply investigate how this continuum of response properties arises: whether through development, auditory activity, or an interdependence. Interestingly, the diversity of MSO response properties arises predominantly through developmental changes to the transcriptome of cells. The spectrum of response properties is almost entirely filled out, and only minorly fine-tuned by auditory activity. Together, this data heavily implies that MSO neurons are fated to become coincidence detectors, but across a much wider range of temporal disparities than previously appreciated.

Table of Contents

List of Figures	x
Chapter 1: Introduction	1
Sound Localization	1
The Superior Olive Complex.....	4
The Lateral Superior Olive	5
The Medial Superior Olive	6
Biophysical Specializations of MSO Neurons.....	6
Development of the Auditory System	8
Spike Generation.....	10
The Axon Initial Segment.....	11
Chapter 2: Threshold Detection in Heterogeneous Populations of Neurons	17
Introduction to Threshold	17
A C-based User interface for Threshold Detection	20
Multiple Threshold Peaks in Heterogeneous Populations	22
Chapter 3: Physiological diversity influences detection of stimulus envelope and fine structure in neurons of the medial superior olive.....	28
Acknowledgements.....	28
Author Contributions Statement	29
Abstract.....	30
Significance Statement	31
Introduction.....	31
Materials and Methods.....	34

Results.....	40
Discussion.....	51
Figures	57
Chapter 4: Glycinergic axonal inhibition subserves acute spatial sensitivity to sudden increases in sound intensity	66
Author Contribution to the work:	66
Abstract.....	67
Introduction.....	67
Results.....	69
Discussion.....	82
Materials and Methods.....	86
Figure and Supplement Legends.....	99
Chapter 5: Regulated gene expression, not auditory activity, drives the development of sound localization neurons.	113
Abstract.....	115
Significance Statement	116
Introduction.....	117
Results.....	119
Discussion.....	126
Online Methods.....	130
Figures and Figure Legends.....	139
Chapter 6: Conclusions and Future Directions	154
Conclusions.....	154
Recommendations for Future Work	156

References.....	158
Chapter 1 References.....	158
Chapter 2 References.....	163
Chapter 3 References.....	165
Chapter 4 References.....	170
Chapter 5 References.....	176

List of Figures

Figure 1.1: Different mechanisms of sound localization in the auditory system – reproduced from Grothe et al. (2010) for visual clarity.....	15
Figure 1.2: Major ascending connections in the auditory brain [reproduction].....	16
Figure 2.1: The Threshold Analysis Panel Contains User-Friendly Elements.....	24
Figure 2.2: Threshold Detection Using Third Derivative Peaks.	25
Figure 2.3: Annotation Functions Help Reduce Methodological Bias.....	26
Figure 2.4: Analysis of Third Derivative Peak 1 and Peak 2 Thresholds in Heterogeneous Auditory Neurons.....	27
Figure 4.1. Sharp ITD-sensitivity to clicks in LSO but not MSO.	100
Figure 4.2. Precise timing and interaction of IPSPs and EPSPs in LSO neurons.....	102
Figure 4.3. Weak ITD-tuning in MSO neurons results from a breakdown of coincidence detection for transients.....	105
Figure 4.4. <i>In vitro</i> recordings reveal powerful inhibition for synaptically-evoked but not for simulated IPSPs.....	106
Figure 4.5. Glycinergic innervation of the axon initial segment of LSO neurons.	108
Figure 4.6. Electron microscopy reveals synaptic terminals on an LSO principal cell’s axon initial segment.	109
Figure 4.7. ITD-tuning in a two-compartment LSO neuron model.	110
Figure 4.8. LSO neurons show graded latency-intensity changes which disambiguate spatial tuning.....	112
Figure 5.1: Intrinsic firing properties of MSO principal neurons change significantly after hearing onset in Mongolian gerbils.	140
Figure 5.2: Experimental design tests the intersection of hearing activity and development on intrinsic neuron properties.....	141

Figure 5.3: Firing heterogeneity changes with development age and hearing status.	143
Figure 5.4: Single action potential parameters change with age and hearing loss.	145
Figure 5.5: 3'-mRNA-sequencing of micro-dissected MSOs shows major change in the transcriptome across development, but not in response to hearing loss.	146
Figure 5.6: Pre- and post- hearing changes to the transcriptome strongly implicate a switch in ion channel expression and post-translational pathways.....	148
Figure 5.7: Posthearing repetitive neurons are not undifferentiated prehearing repetitive neurons.....	150
Figure 5.8: Machine-learning algorithms accurately predict firing type from ion channel transcript abundance data.	152

Chapter 1: Introduction

SOUND LOCALIZATION

Sound localization is a crucial computation performed by the brain to determine the origin of sound in space. This mapping of space is fundamental for processes such as localizing prey (or vice versa) in a predator-prey relationship (Hoy, 1992), in early developmental language acquisition (Brown & Balkany, 2007; Isaiah et al., 2014), and for discriminating sounds in complicated acoustic environments, such as cocktail parties (Arons, 1992; Pollack & Pickett, 1957). Unlike other sensory systems, such as the visual system where space is discretely mapped by the retina or the somatosensory system, the auditory system maps frequency, and therefore must generate a spatial map *de novo*.

Research has demonstrated that sound localization is one of the first neural computations in the auditory brain pathway, where unique nuclei, or clusters of neurons, transform acoustic information into spatial information (Ashida & Carr, 2011; Catherine E. Carr & Christensen-Dalsgaard, 2016). The main region demonstrated to do this in mammals is the Superior Olive Complex (SOC), located within the hindbrain, and is a grouping of several brain regions: the Medial Superior Olive (MSO), Lateral Superior Olive (LSO), and Trapezoid Bodies (TB – medial nucleus and lateral nucleus - MNTB, LNTB). In avian species, the sound localization is performed in the nucleus laminaris (NL), although the details of how it generates a spatial map differs from the mammalian SOC in an interesting case of convergent evolution (C.E. Carr & Soares, 2002). While much research has been done primarily on sound localization as it pertains to the SOC, i.e., on azimuthal sound localization, it is important to note that other sound localization pathways generate essential information along other spatial planes. For example, the auditory system can discriminate cues along the altitudinal plane, but is comparatively less precise than the

azimuthal plane, and is often determined by spectral notches, or transformations induced by the pinna (ear) as sound reflects and rebounds as it is directed into the ear canal. However, for the sake of brevity, this chapter, and the work that follows will primarily focus on azimuthal sound localization in the SOC, as it provides a discrete neural framework through which neuron structure-function relationships are extremely specialized to provide precise spatial acuity.

As I will focus primarily on the mammal here, the SOC will generally be referred to as the region that generates spatial information along the azimuth. Previous theories ranging as far back as over a century ago have described a duplex theory of sound (Rayleigh, 1907), and argue that sound localization is differentially calculated depending on the incoming frequency of sound. Anatomically, this theory was supported as the SOC has two discrete anatomical correlates for low and high frequency sound localization: the MSO relies on low-frequency cues and extracts timing differences, while the LSO receives higher-frequency cues and extracts differences in sound intensity, or level. Typically, this frequency separation in the duplex theory has been split at $\sim 1.5\text{-}3\text{kHz}$, where the phase-locking ability of neurons, or the ability of a neuron to respond in-phase with the phase of the incoming sound stimuli, breaks down (Grothe et al., 2010) (**Figure 1.1** – a copy of the figure from Grothe et al. 2010, displayed here for clarity). This splitting of frequency along the two primary sound localization pathways has persisted as a theory for nearly a century, although recent work has demonstrated that this dichotomy is no longer as clear cut as once believed (Franken et al., 2018; P. X. Joris & Yin, 1995). Rather, more recent interpretations discuss an overlapping of feature processing across pathways, rather than the previous belief and adherence to a perfect separation of information streams based on a hard frequency cutoff and discrete segregation between the MSO and LSO.

For these two pathways to localize sound, neurons integrate differences in sound arriving at the left ear versus the right ear. For the MSO, neurons rely on interaural time differences (ITDs), while the LSO relies on differences in intensity generated by a “sound shadow” due to the shape of the head (Rayleigh, 1877), which generates an interaural level difference (ILD) (Grothe et al., 2010) (**Figure 1.2** – a reproduction of the major auditory circuitry in the brain duplicated here for anatomical reference). These pathways fundamentally rely on the effect that a head shape has on sound, also known as a head-related transfer function (HRTF), and is unique across different species of mammals. Interestingly, mammals with unique head sizes and audiograms (the range of frequency-intensity combinations an animal hears best over), exhibit different sized LSO and MSO nuclei, with controversial theories from an evolutionary perspective arguing the reasoning why one nuclei is enlarged relative to another (Grothe et al., 2010; Masterton et al., 1967). Moreover the size of the head is directly proportional to the range of detectable ITDs for a given species (Masterton et al., 1967). Some rodent models exhibit diminished numbers of MSO cells, and rely highly on the LSO, as they communicate in ultra-sonic frequency ranges, and the size of their heads are better suited to high frequency level differences. Other models for auditory perception, like the cat, exhibit a fully developed LSO and MSO (as well as other SOC nuclei). Yet other models, however, like the Mongolian gerbil, contain an enlarged MSO relative to the size of the LSO, as they exhibit an audiogram more closely related to human hearing, and like humans, rely fundamentally on lower frequency auditory stimuli.

THE SUPERIOR OLIVE COMPLEX

The Superior Olive Complex is a group of nuclei that are developmentally closely related, deriving from the same rhombomere (Marrs et al., 2013). Classically, the LSO and MSO are prime targets to study, although nuclei that provide well-timed inhibition to the MSO/LSO, like the MNTB/LNTB, are also extensively studied as they exhibit a wealth of specialized properties directly implicated in their function. Together, these nuclei function as an early way-station in the auditory pathway to extract spatial information from sound. Incoming sounds are transduced into electrical signals at the cochlea, deconstructed and mapped by frequency, where they then propagate through spiral ganglion neurons to the cochlear nucleus, the first brain region in the central auditory system. Here, a variety of cell types exhibit well-documented structure-function relationships, ranging from unique dendritic architecture to synaptic specializations, to precise intrinsic properties. These cells extract a range of unique sound features from sound stimuli, with one subset, the Bushy cells, coming in two varieties (globular or spherical), that directly project to the SOC. These specialized cells are entirely engulfed with synaptic contacts, which helps provide the precise timing of inputs to the SOC needed to perform ITD calculations.

The SOC, receiving bushy cell input from both the ipsilateral and contralateral cochlear nuclei, becomes the first region to integrate binaural signals. Several decades ago, Lloyd Jeffress postulated a theoretical wiring diagram for how cells in the brain could be set up to receive binaural signals, integrate the signals based on arrival time difference, and thus an array of neurons tuned to slightly different ITDs would generate a spatial map (Jeffress & A., 1948). This theory has proven remarkably accurate for several avian species, and conceptually has helped build our understanding of the mammalian sound localization circuitry. In the following subsections, I will focus discretely on the mammalian LSO and MSO as they pertain to sound localization.

The Lateral Superior Olive

The LSO is the primary region of neurons that integrate differences in level, or intensity, of sound. Anatomically, LSO neurons receive excitatory input from the ipsilateral cochlear nucleus (through spherical bushy cells), and inhibitory input from the contralateral cochlear nucleus, by way of the MNTB (Philip X Joris et al., 1998; Smith et al., 1991; Tollin, 2003). Together these signals are integrated, with ILD sensitivity determining whether an individual neuron will fire, and thus the output relates to the spatial origin of sound. ILD integration for higher frequencies (general ranges are ~2-4kHz up to 16-20kHz) is believed to be a common mammalian pathway, with a comparatively longer evolutionary timeline (Nothwang, 2016; Tollin, 2003).

As a fascinating comparison to the MSO, discussed further below, the LSO requires temporal precision to integrate ILDs with iso-frequency inputs (Guinan et al., 1972), or else disparate sounds would be integrated and generate miscellaneous information about the acoustic environment. Therefore, LSO cells also exhibit characteristics, such as membrane properties, related to temporal precision (P. X. Joris & Yin, 1995), but the nature of their intrinsic integration is distinct from the MSO, as they fundamentally perform a subtractive computation. For a given sound source, LSO neurons in the hemisphere closer to the source will receive excitation from the ipsilateral cochlear nucleus, while simultaneously receiving inhibition from the contralateral source. Together, the intrinsic properties of LSO neurons and synaptic arrangement/polarity yield neurons that are sensitive to both timing and intensity differences. These properties specialize LSO neurons such that their ILD sensitivity is reflected in their output – overall firing rate, with different cells tuned to a corresponding ILD (Tollin, 2003; Tollin & Yin, 2002).

In parallel with the ongoing work discussed in the later chapters of this text, recent questions in the LSO surround functional diversity of neurons. Particularly through recent

work (Franken et al., 2018), arguments surrounding the nature of principal vs non-principal cell-types of the gerbil LSO arise. Using a combination of anatomical reconstructions, electron microscopy, and *in vivo* recordings, they discuss how firing patterns from certain principal LSO neurons favor onset responses, rather than non-principal sustained or “chopper-like” firing patterns has caused a revisiting of questions of cell-type. Similar to our work discussed in **Chapter 3**, where we find a diversity of firing responses in MSO principal cells, this work in the LSO parallels our emerging understanding that principal neurons may be defined as a single functional class with a broad array of properties along a given parameterized axis. As Franken et al. describe it, “our results contribute to an emerging picture of the auditory brainstem composed of parallel circuits,” where complex stimuli are deconstructed and processed separately, but in parallel. This broadening of a cell type definition in turn emphasizes a need to explore previously ignored “non-principal” cell types, that may simply represent diverse information extracted from a given feature of sound.

The Medial Superior Olive

The MSO contains an array of fusiform-shaped neurons arranged along the topographic axis of frequency (tonotopic axis). Anatomically, MSO neurons have a stereotyped simple circuit, with bilateral excitation arising from ipsi- and contra-lateral cochlear nuclei bushy cells targeted onto the dendrites, and feed-forward inhibition generated by way of the trapezoid bodies targeted onto the soma.

Biophysical Specializations of MSO Neurons

MSO neurons exhibit a constellation of biophysical specializations, all of which function to tightly control spike generation. As the site where low-frequency sound

localization computation occurs, MSO neurons have been shown to compute ITDs within an incredibly narrow window of time, on the order of *microseconds*, with mammals reportedly utilizing ITDs down into the 10-40 μ s range (Brughera et al., 2013; Hartmann et al., 2013; Rosskothén-Kuhl et al., 2021). This narrow window for integration of binaural signals is generated by enrichment of specific potassium channels (predominantly Kv1 channels), as well as hyperpolarization-activated conductances (HCN channels). These conductances, some of which are tonically active at rest, along with leak channels, push passive membrane properties to incredibly low input resistances (<5-10M Ω) and fast time constants (~0.300 ms), and therefore act to filter monaural signals, as well as binaural signals that arrive disparate in time (Golding & Oertel, 2012; Khurana et al., 2011; Mathews et al., 2010; Roberts et al., 2013).

These input signals, arising from the cochlear nucleus and trapezoid bodies (TBs), are spatially arranged on MSO neurons in a unique pattern to further aid in filtering properties. For MSO neurons, the coincident arrival of binaural signals is integrated through the spatial arrangement of excitatory synapses on bipolar dendrites, segregated such that each dendrite receives input from one ear. Inhibitory synapses are exclusively localized to the somas (Grothe et al., 2010). As determined by Pecka et al. (2008) using *in vivo* recordings, the impact of the inhibitory glycinergic signaling arising from the TBs, demonstrates that precisely timed inhibition both sharpens ITD sensitivity, but can generate a shift in the ITD function of MSO neurons, yielding a range of ITDs to spatially map an acoustic environment. Excitatory inputs, however, are arranged exclusively on the dendrites of MSO neurons and generate precisely timed excitatory post-synaptic potentials (EPSPs) (Callan et al., 2021; vanderHeijden et al., 2013). These EPSPs propagate through enlarged diameter dendrites, and due to the spatial gradients of Kv1 and HCN channels,

their relative timing is preserved, rather than lost due to cable filtering (Golding & Oertel, 2012; Khurana et al., 2011; Mathews et al., 2010).

DEVELOPMENT OF THE AUDITORY SYSTEM

The auditory system is a prime system to study how coding and neural properties change throughout development as it is relatively easy to make discrete manipulations, and in many experimental rodent models, neonatal/juvenile animals are born deaf and have delayed hearing onsets until nearly the second week after birth. The concept of “hearing onset” describes the phenomenology that typically-studied rodent models (mice, rats, gerbils), are born with closed ear canals. After a week and a half, depending on the species, tissue in the ear canal undergo morphogenetic changes and increases in apoptosis that open the ear canal (Clause et al., 2014; Echteler et al., 1989). These dramatic changes occur typically over the first week after hearing onset, with animals steadily increasing in responsiveness to high-frequency stimuli. Due to the nature of sound waves, high-frequency sounds are more easily deflected and distorted by the pinna and tissue blockage, while low-frequency sounds, even before and throughout hearing onset, can be conducted through bone conduction – the resonance of bones in the skull with these frequencies. This developmental progression can be manipulated to study a variety of topics, including the effects of hearing loss, monaural vs. binaural signaling, critical development periods, and others. Generally, animals can be surgically deafened, earplugged, lesioned, or treated with ototoxic chemicals which degrade hair cells within the cochlea (the cells which transduce sound pressure waves into electrical activity).

Recent work by the Bergles group has extensively shown that although hearing onset is delayed in common experimental animal models, the developing auditory system is not quiescent. Interestingly, their work demonstrates that supporting cells in the developing cochlea release ATP, triggering a cascade of activity locally in nearby hair cells (specifically inner hair cells – IHCs), which in turn stimulates activity that propagates through spiral ganglion neurons (SGNs) in contact with IHCs, and directly into the central auditory nervous system (Sun et al., 2018; Tritsch et al., 2007; Tritsch & Bergles, 2010). This “spillover” mechanism establishes local activity in spatially grouped IHCs, and as the activity spreads into the auditory system, is vital for establishing the patterning of the auditory system. Moreover, neurons and their connections are spatially organized based on the frequency of their inputs (known as tonotopy) – and this tonotopic map is believed to be established through these waves of local activity (Clause et al., 2014; Kandler et al., 2009).

Additionally, while the wiring of the auditory system is established throughout a pre-hearing window of development, it is known that neurons in discrete nuclei undergo dramatic changes themselves. Electrophysiological work shows that shortly after hearing onset, intrinsic and synaptic properties within the MSO and LSO change significantly. The intrinsic properties that allow the MSO to precisely filter non-coincident activity change considerably after hearing onset, with passive membrane properties (membrane resistance) dropping by nearly an order of magnitude. Furthermore, potassium conductances sharply increase, while somatic sodium conductances decrease, the latter of which minimally boosts EPSPs to preserve temporal fidelity. These changes are mirrored at the transcriptional level, as many ion channels are differentially expressed during development (Ehmann et al., 2013). It has also been shown that markers of cell-type identity, particularly calcium-binding proteins such as Parvalbumin, have increased expression only in the

mature MSO (Franzen et al., 2020; Lohmann And B C M & Friauf, 1996). Additionally, synaptic rearrangement shifts the spatial arrangement of excitation and inhibition into their segregated dendritic and somatic locations, respectively, in the mature MSO (Magnusson et al., 2005).

The auditory system in general is a prime location for studying developmental changes to neural circuits. The MSO provides a unique substrate to study how factors like development and changes to normal auditory activity shift sound localization properties, as behaviorally, sound localization exhibits improvements in spatial acuity with development (Werner & Gray, 1998). By modulating the normal progression of hearing onset through ear plugging, surgical deafening, or other methodologies that alter sound stimuli, like omni-directional noise exposure, the MSO demonstrates compensatory changes in dendritic morphology (Feng & Rogowski, 1980), ITD coding, and synaptic innervation patterns (Kapfer et al., 2002; Pecka et al., 2008). More broadly, compensatory changes are seen throughout the wiring of the auditory system globally, as deafening shifts the size of tonotopic lamina (Clause et al., 2014; Kandler et al., 2009). It remains an open question, however, how exactly this intersection of developmentally-driven genetic/cellular regulatory pathways and activity act in concert to establish an array of precise neuronal properties. The relative contribution of activity and gene expression on changing synaptic and intrinsic neuron properties is ripe for future investigations.

SPIKE GENERATION

Neurons fundamentally transform information through the processing of inputs, and depending on the function of the individual neuron, make a binary decision to generate an action potential. This action potential (AP) is a response to the inputs and provides salient information to subsequent neurons in the circuit. This critical juncture of action

potential generation therefore is a tightly regulated phenomenon, involving anatomical and physiological specializations. The inability of a neuron to generate a spike at the correct time, or conversely, by spiking too often when it should not, has a wide range of potential consequences. Anomalous spiking functionally represents a severe breakdown of information processing, as mis-timed or mis-cued spikes may, depending on the circuit, reinforce incorrect behaviors, generate epileptic activity, or lead to incorrect assessment of environmental cues. The severity of any information breakdown has a wide range, and thus spike generation is a relatively conserved process in neurons.

The Axon Initial Segment

Spike generation, the all-or-none decision making computation performed by neurons has, historically been associated with the axon of neurons. Originally, the axon hillock, the trunk shaped region of the proximal axon that connects to the soma, or cell body, was believed to be the site of AP generation. However, work over recent decades has implicated a region known as the Axon Initial Segment (AIS), found just distal to the hillock, to be the primary region that controls spiking. The AIS is a molecularly defined region proximal to the first node of ranvier, where myelination begins. It is defined by a series of specific proteins that extend for discrete lengths along the proximal axon, including but not limited to, specific cytoskeletal proteins (AnkyrinG, Beta4-Spectrin), scaffolding proteins (Psd93), and voltage-gated ion channels (Nav1.1, Nav1.2, Nav1.6, Kcnq2/3, Kv1.1, Kv1.2) (Gasser et al., 2012; Jones & Svitkina, 2016; Nelson & Jenkins, 2017; Van Beuningen et al., 2015; Yang et al., 2007). Some of these proteins are highly conserved and vital to a functioning AIS, such as AnkyrinG (AnkG) – the “master regulator” of the AIS, while others (particularly the voltage-gated ion channels) demonstrate localization patterns throughout the entire somatodendritic compartments of neurons, not solely the AIS (C. Y.-M. Huang & Rasband, 2018).

Studies demonstrate that the AIS, consisting of a periodic cytoskeletal structure, and providing scaffolding for high densities of voltage-gated ion channels, is a prime location to regulate spike generation. Structurally, the AIS is typically small in diameter (reducing the membrane capacitance, particularly relative to the soma), and due to a high density of channels, particularly voltage-gated sodium channels, acts to tightly regulate threshold, the voltage above which a neuron will fire an action potential. Interestingly, across brain regions and neuron types, this threshold parameter is equally diverse and reflects not just how the neuron transforms information, but is directly related to differences in AIS parameters, such as its overall length, size, or specific ion channel composition. For instance, studies reveal that often the specific isoform of sodium channels expressed within the AIS changes with developmental time. Other investigations have directly shown that the AIS is a plastic structure: structural parameters, such as the proximal distance before the AIS begins may shift in response to activity. This has direct functional implications, as in the avian auditory system, neurons that respond to different sound frequencies have longer or shorter overall AIS lengths (Grubb & Burrone, 2010; Kuba, 2012; Kuba et al., 2006, 2014).

Furthermore, as the primary output region of a neuron, the AIS is an evolutionarily conserved structure with a unique developmental progression. Developing neurons are relatively unpolarized, i.e.: inputs and outputs are not fully unidirectional, where neurites (initial outgrowths) are not yet functionally determined as a dendrite or an axon (Bentley & Banker, 2016; Vitriol et al., 2012; Zhong et al., 2014). A series of intracellular signaling events is required to specify one neurite into the future axon of the neuron. These events then lead to a series of trafficking steps, upon which AnkG and other proteins are targeted to the future axon, which in turn prevents AIS-specific proteins from being mis-targeted to future dendrites. Conversely, dendrite-specific proteins are barricaded from entering into

the developing future axon (Y.-M. Huang & Rasband, 2016). Together, these pathways yield a fully functional AIS with select localization of cytoskeletal and associated proteins that provides unidirectional output for the cell.

As further evidence that the AIS is a plastic structure, experiments have tested what happens when the AIS, or more distal portions of the axon are damaged. Fascinatingly, the axon, if the damage is irreparable or too traumatic, no longer undergoes typical regrowth and regeneration pathways (Hoogenraad & Bradke, 2009; Shi et al., 2003; Stoler & Fleidervish, 2016). Instead, the damaged axon becomes de-differentiated and developmental pathways are potentially upregulated to specify a new axon for the neuron. The extent to which a neuron can undergo these re-specification pathways has been shown predominantly in developing neurons, but whether mature neurons may be triggered to utilize this pathway, or if it could be used to further aid regenerative cell pathways remain open, yet critical questions for future studies.

Work in later chapters, specifically **Chapters 3 and 4**, will demonstrate findings pertaining to the structure of the axon initial segment in the MSO and LSO. The experiments performed in those chapters specifically addresses two questions. The first was to understand whether the MSO also exhibits systematic differences in AIS structure (particularly length and proximal spacing), similar to those seen in the avian auditory system. Particularly, the question is whether there are systematic differences in structural AIS parameters that directly correlated with the present or absence of repetitive firing neurons in the MSO. This stems from the idea that slight modifications to the AIS may yield major alterations to the spike pattern generated within these neurons, as the AIS is explicitly linked to spike generation. The second question addressed in this body of work regarded whether synapses could directly alter the computational properties of an LSO neuron. Based on other evidence of axo-axonal synapses (synapses that directly contact the

axon initial segment, rather than the somatodendritic compartment) such as in chandelier cells and other brain regions (Howard et al., 2005; Wefelmeyer et al., 2015), the work directly asked if this might structural arrangement might also be true for neurons of the LSO.

In conclusion, it is the hopes that the reader, following this introduction, will see a broader perspective of how we investigated myriad cellular properties of superior olive complex neurons. The subsequent chapters will cover the work documented in three individual manuscripts pertaining to the topics discussed here. For chapters relating to structural parameters and spike generation see **Chapters 2, 3, 4**, as they directly provide evidence on reproducibly measuring threshold (**Chapter 2**) and structural parameters about the AIS (**Chapters 3, 4**) in MSO/LSO neurons. For evidence on electrophysiological characterizations of SOC neurons, please see **Chapters 3, 4, 5**, which contain relevant information from *in vitro* as well as *in vivo* recordings from SOC neurons. Finally, for a perspective on shifting gene expression in MSO neurons throughout development and in models of hearing loss, we direct the reader to **Chapter 5**.

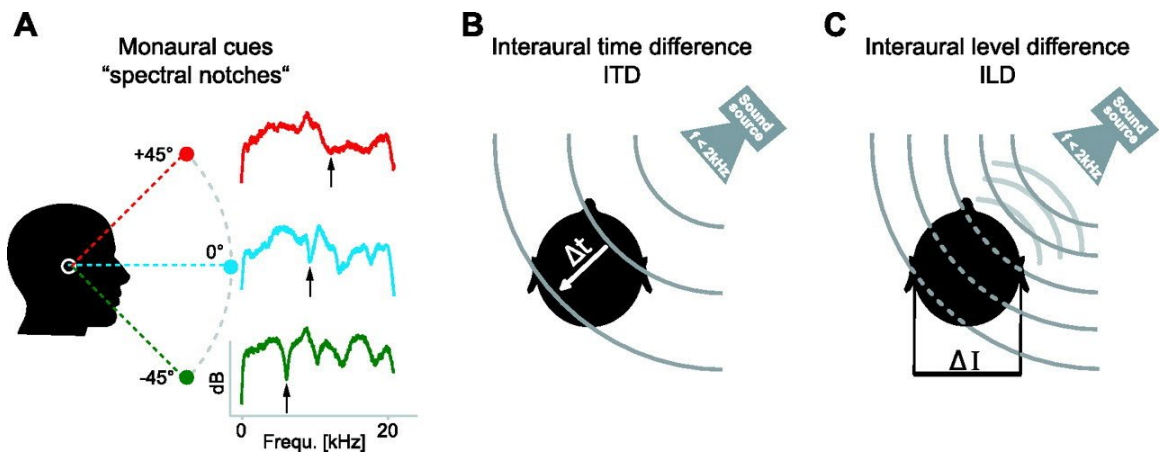


Figure 1.1: Different mechanisms of sound localization in the auditory system – reproduced from Grothe et al. (2010) for visual clarity.

A reproduction of a figure from Grothe et al. (2010) discussing the use of different sound features and frequencies for the use in sound localization computations. Briefly, altitudinal sound localization cues are determined through monaural cues, while azimuthal cues are generated through interaural time differences (ITDs) and interaural level differences (ILDs).

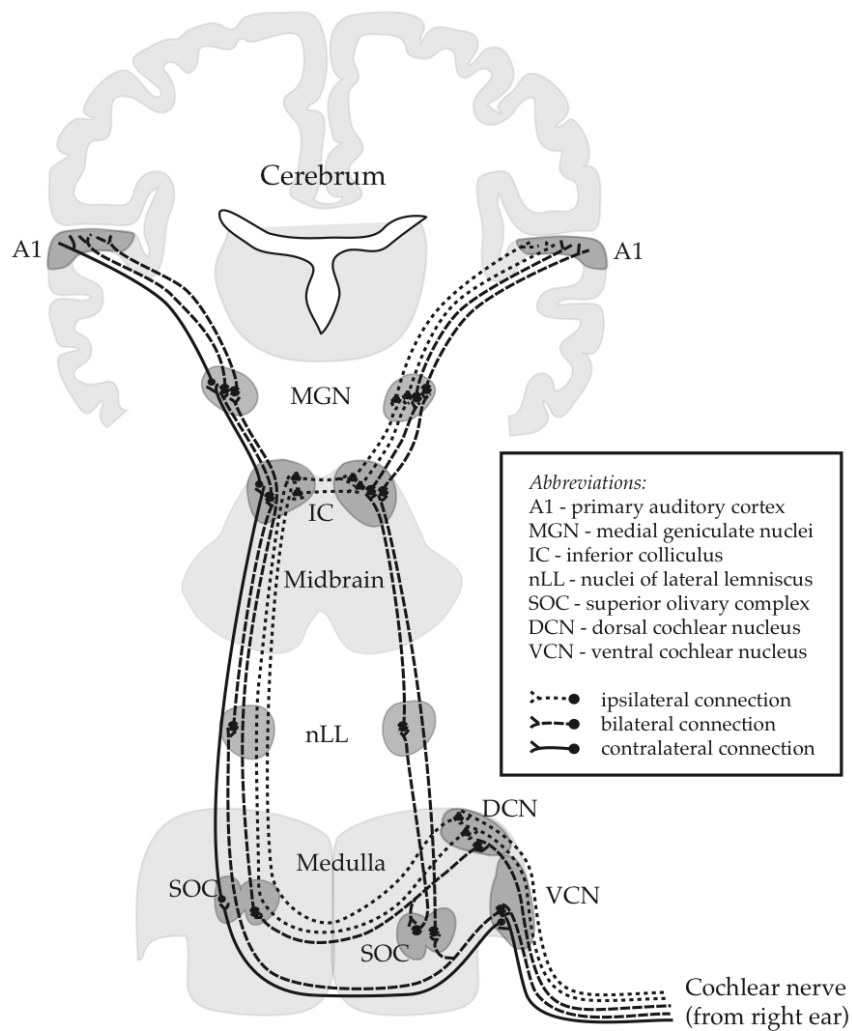


Figure 1.2: Major ascending connections in the auditory brain [reproduction]

Diagram of the major brain regions comprising the ascending auditory circuitry of the brain. The regions discussed here (the Medial Superior Olive – MSO; and the Lateral Superior Olive – LSO) are components of the SOC.

Reproduction from

<<http://www.tulane.edu/~h0Ward/BrLg/CentralAudPathway.html#id5>>, original image from Netter’s Atlas of Human Neuroscience. Author:David L. Felten, Chapter:Sensory Systems Page:228

Chapter 2: Threshold Detection in Heterogeneous Populations of Neurons

INTRODUCTION TO THRESHOLD

Threshold is a crucial parameter in neurons. As described in the introduction, it is a measurement linked to spike generation, and the major decision point for a neuron: whether to fire an action potential and transmit information or not. This all-or-nothing line is the basis of all information processing in the brain. Most neurons integrate, process, and filter incoming information, whether from a sensory stimulus transduced into an electrical signal, or from other neurons releasing neurotransmitters at a synapse and evoking a post-synaptic response. Exactly what information is transformed, and how is determined by the intrinsic properties of neurons. For neurons performing an integrative computation, threshold may require precise summation of inputs, either temporally or spatially, such as determining if two cues are linked (like in behavioral reward experiment), or whether processed information arrives on the same dendritic arbor. For other neurons, that filter incoming signals, threshold may instead determine whether a signal has a great enough amplitude, i.e.: only responding when a sound is above a certain loudness. While this is a gross simplification, threshold acts as an inherent information transfer function, and thus accurate measurement of it is crucial to our understanding of neural function throughout the brain.

Threshold has historically been measured through a variety of ways, and for the purposes of this chapter, I will primarily focus on methodologies used in whole-cell current clamp electrophysiology recordings. As a major technique used to record and measure the intrinsic properties of neurons, experimenters often will inject a series of current ramps, square pulses, or other shapes that mimic the physiological input that a neuron receives. By adjusting amplitude and temporal dynamics of the current injected into a neuron, it is

possible to elicit a voltage response from the neuron. Often these responses will be sub-threshold in nature (not elicit an action potential), until eventually the increasing stimulus rate, amplitude, etc. reaches a minimal point that evokes the first action potential, a strong, rapid depolarization of the membrane voltage with active conductances driven by a variety of voltage-gated ion channels. This voltage response, or waveform, is often analyzed and measured based on how quickly it rises or falls, how wide it is, or how high its amplitude is. While all of these parameters inform the experimenter about the ion channels the neuron may contain, threshold is one crucial measurement that may be made.

Normal methods of interpreting and measuring threshold by electrophysiologists are diverse and oddly dependent upon training lineage. Some labs, particularly those who record from similar neurons, use *a priori* methods of threshold detection. That is, a predetermined value is utilized, and when either the voltage waveform, or some derivative of the voltage signal in time, is assessed for when it crosses this value. This approach is incredibly fast, and reliable when used on homogenous populations of neurons with similar intrinsic properties. When switching to a different, equally homogenous population, this methodology excels by adjusting the *a priori* value, and often confirming that the detected threshold value “looks reasonable.” Furthermore, some detection methods, in order to avoid the use of an *a priori* determinant of threshold, use automated, custom written code to automatically try to detect components of the first or second derivative, or peaks within a specific time range. However, throughout the remainder of this chapter, I will emphasize a modified methodology, developed in part from Sekerli et al. (2004), which enables an experimenter to more precisely detect threshold, particularly in heterogenous populations of neurons, which, at the cost of automation time, drastically improves accuracy in non-homogenous samples.

As is becoming increasingly apparent in neuroscience, many brain regions contain neurons with a variety of properties, unique morphologies, expression of various neural markers or calcium-binding proteins, and various other specializations. In our current work, we currently describe neurons of the MSO, a previously assumed homogenous nucleus, which in fact has a single principal neuron type with a tremendous diversity of response properties. These neurons are strikingly similar in their anatomy, circuitry, transcriptomes, and passive properties, but divergent in the number, size, and shape of action potentials they fire. This diversity of responses crucially makes *a priori* methods of detecting threshold inaccurate, and thus inaccurate.

To address this issue, I have adapted a new protocol (Sekerli et al., 2004), which involves a transformation of the voltage response into the third derivative of voltage. In this form, where a voltage in time $V(t)$ signal is derived into $V'''(t)$, strong changes in the inflection of a signal may be detected. This $V'''(t)$ signal essentially generates a local maximum for the signal when the inflection of the action potential is changing at the fastest rate. Crucially, this local maximum coincides with the inflection, or “elbow” at the base of the AP, often where seasoned electrophysiologists can estimate threshold to be, as strong depolarizing currents determine the upswing of an action potential. For neurons with more complex spike waveforms, however, this methodology both standardizes and improves over other methods of threshold detection, particularly compared to *a priori* methods that cannot handle diverse samples, and automated methods, which can be inaccurate when multiple peaks are present in the third derivative. The latter case will be described in detail in a subsequent section, **Multiple Threshold Peaks in Heterogenous Populations**. As the primary goal is to standardize threshold detection, not just across experiments, but across labs and disciplines, the aim of the work presented below was to create a user-friendly interface and discuss the principals behind threshold detection. Furthermore, it is our hope

that focusing on critical parameters, like threshold, and how they are measured, we will greatly improve the reproducibility of peer-reviewed experiments.

A C-BASED USER INTERFACE FOR THRESHOLD DETECTION

Primary input to the analysis suite is in the form of a series of action potential waveforms, preferably those recorded using a threshold current injection, defined here as the current injection that results in a failure to generate a spike in ~50% of trials. To highlight the functionality of this analysis suite, we provide a brief overview of its daily usage, with an example display shown in **Figure 2.1**. Primarily, spikes can be displayed as group data, or individual spikes, with the left-hand displays providing a view of the original $V(t)$ signal, and with each subsequent derivative below it: the first, second, and third derivatives of $V(t)$ respectively. The right-hand displays provide areas to actively measure threshold, with a modular display of the $V(t)$ waveform on top, the third derivative $V'''(t)$ in the middle, and the analysis parameters displayed in the table on the bottom (visible in **Figure 2.2**). After starting the software from a series of spikes, the software appears as in **Figure 2.1**, the table is initialized using the buttons along the top of the panel, by clicking “Initialize Analysis Waves,” displayed using “Override Wave Display,” and finally set to analyze the set number of input waves using “Redimension Waves.”

Analysis is performed by placing a cursor on peaks of the third derivative right-hand window. Using the window start and window end parameters to zoom in on action potential scales all windows accordingly. **Figure 2.2** provides a display of the software in action, with the updated analysis wave table displayed, and a cursor placed on the second peak. As peaks are saved using “Save Peak 1/2” to save only the amplitude, or “Get All 1/2” for several additional measurements, such as time or voltage derivative, the data is saved in the table below. Furthermore, annotations are made in the graph above, with *Line*

C indicating a saved peak 1 entry, and *Line D* indicating a saved peak 2 entry. As data is saved for each spike, iterating through the input waveforms using the “Rheo number” display box, the table of values is filled. Finally, general action potential parameters can be determined based on the measured threshold, such as spike amplitude relative threshold, maximum depolarization rate, and halfwidth – all by clicking “Finish Spike Data.” An output display is generated by clicking “Average Waves,” upon which the values from the table will be averaged, providing a summary of the spike parameters for the action potentials provided by the researcher. All of the data is stored in cases where the researcher wishes to access individual spike data as well.

If a researcher is uncertain how the third derivative peak detection method provided here compares to their current methodology, we also provide several features to help approximate and visualize the differences in measurement accuracy. For example, the “Approximate from Dv1” button allows a researcher to test an *a priori* value, which can be set within the software, with future integrations of the software being designed to test input values against the second derivative or based on other currently used detection methods. Additionally, we have integrated a button, “Annotate PPP,” designed to generate a phase-plane plot, which displays the first derivative of voltage versus the membrane voltage. These plots, commonly used electrophysiologists, provide an easy view of how the action potential changes as a function of voltage, and threshold is easily seen (**Figure 2.3** - right panel) as the “kink” annotated by the solid line. Interestingly, compared to other threshold detection methods, few are able to detect the second peak in the third derivative (dotted line in the phase-plane plot), a change believed to be implicated in a secondary activation during action potential generation.

MULTIPLE THRESHOLD PEAKS IN HETEROGENEOUS POPULATIONS

We find that use of the third derivative peak detection method for threshold detection performs equally well as past methods for homogenous populations of neurons. It is superior, however, particularly in heterogeneous populations of neurons, and for neurons that exhibit two peaks in the third derivative (see **Figure 2.2** – cursor). Often for cells where the peaks are of similar amplitude, upon multiple trials the relative heights between the first and second peaks may fluctuate such that one has a greater amplitude for only a portion of the trials. This leads to mismeasurement of threshold for methods that rely on code which automates the measurement process. With our methodology, we report that not only does accuracy improve, but further hypotheses on spike generation arise.

The curiosity of two unique, slightly temporally separated peaks in the third derivative suggests to us that there are two sequential activations of currents within a neuron. Previous studies in the literature indicate the axon initial segment (AIS) is a prime spatial region for controlling spike generation (Adachi et al., 2015; Fukaya et al., 2017; González-Cabrera et al., 2017). It is uniquely poised a small diameter region with high densities of voltage-gated ion channels, but voltage-gated sodium channels in particular. Some neurons, however, exhibit further expression of voltage-gated sodium channels within the somatic compartment, but because it acts as a large capacitive sink, is a poor region to regulate spike generation. Based on the observations made here, along with previous descriptions of bi-lobed phase-plane plots, and further evidence of sodium channel activation (Colbert & Johnston, 1996; Park et al., 2013; Yang et al., 2016), we believe that the first and second peak of the third derivative correspond to the initial segment, and somatic activation of sodium channels, respectively. Furthermore, we posit that the measurements of these peaks, their relative ratios, and general separation in high

quality recordings may provide useful insight into the expression of sodium channels in these regions, and generally how spike generation is spatially regulated.

Previous work suggests that with increasing somatic sodium channels, the amplitude of the spike, and potentially overall firing pattern of a spike may be altered (Evans et al., 2015; French et al., 1990; Fukaya et al., 2017; Hu & Jonas, 2014; Raman et al., 1997; Shu et al., 2007). For instance, in the MSO, previous work demonstrates that somatic expression of sodium channels reaches incredibly low levels in order to minimally boost EPSPs, while simultaneously decreasing levels of back propagating action potentials (Scott et al., 2010). Moreover, these neurons fire action potentials that barely reach amplitudes of 10-15mV, and in third derivative threshold analysis, exhibit small first peaks, and no secondary peak. Furthermore, in our recent work discussed in **Chapters 3 and 5**, the heterogeneous population of MSO neurons provides an interesting diversity of peak 1 and peak 2 amplitudes. In particular, the first and second peak differences can be seen in **Figure 2.4**. While these data all exhibit a strong linear correlation, the general cartesian space occupied by different firing types (here: P- Phasic; R- Repetitive; PH – Prehearing, a juvenile repetitive firing type) on average is different. Put simply, the center of the points for a given group is different in terms of each peaks' voltage, and the spread along these axes is also different. As this software develops, and further experiments provide on the potential temporal separation of AIS vs. somatic activation of sodium channels, our goal is to further expand the work presented here, particularly by developing novel metrics that help interpret the ratio and relative timing differences of these peaks.

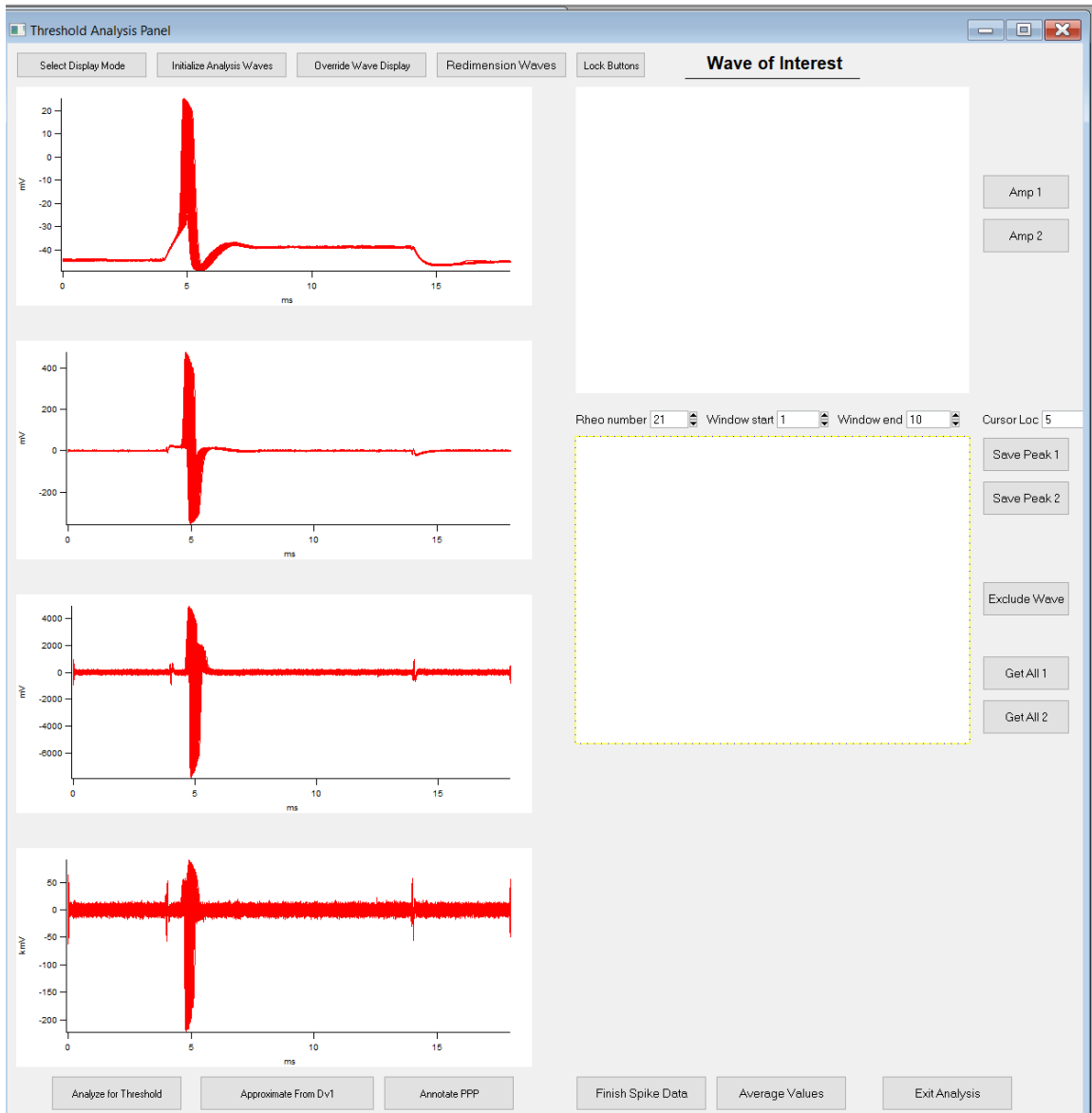


Figure 2.1: The Threshold Analysis Panel Contains User-Friendly Elements.

Here we provide an example of the Graphic User Interface (GUI) built in Igor Pro, a C-based coding language. The panel, while still in development, provides a variety of analysis features. Here we show the startup configuration, with graphs displayed starting top left are the voltage waveform recorded by the user, followed by sequential derivatives below it: the first, second, and third derivatives of voltage in order. The right side provides the user-interface aspect of the software, with a scalable window, and the ability to use a cursor to save data.

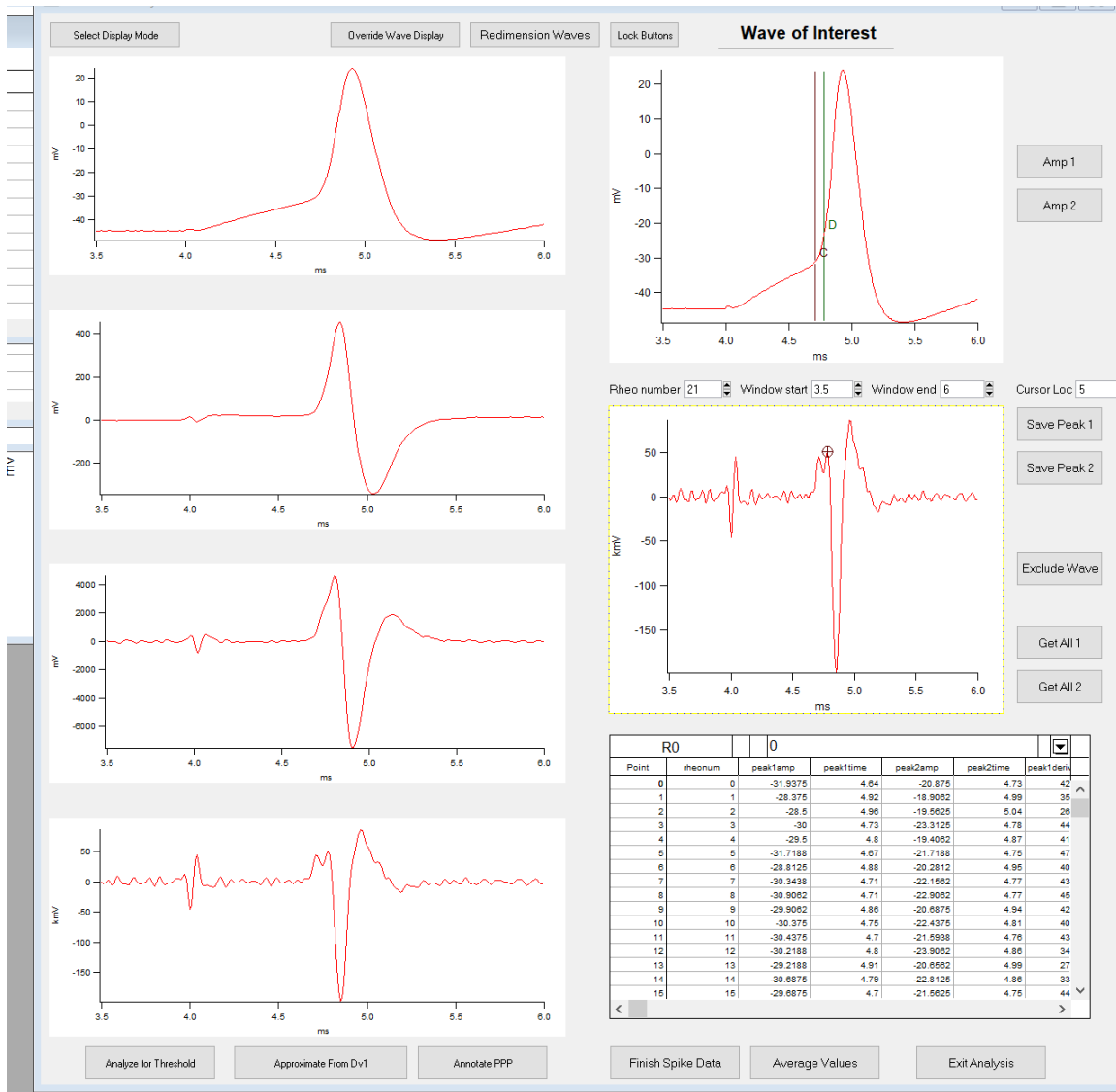


Figure 2.2: Threshold Detection Using Third Derivative Peaks.

Here we show the analysis of a spike, with window size already set on the right-hand set of graphs, and an active cursor placed on the second peak in the third derivative. Display mode has been toggled to show only the spike and its sequential derivatives along the left-hand side. Active analysis is ongoing on the right side, with a cursor placed on the third derivative graph to analyze two peaks.

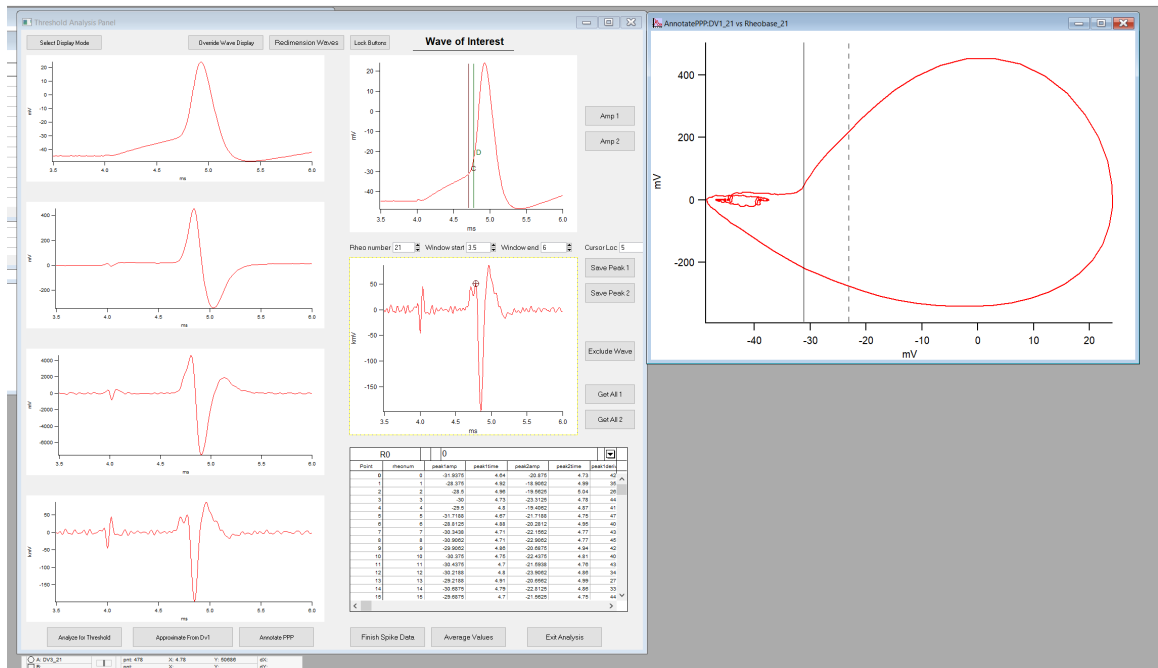


Figure 2.3: Annotation Functions Help Reduce Methodological Bias.

As an additional feature of the GUI, we have added methods to compare past threshold detection methods, with the third derivative method discussed here. Of note, users can test *a priori* first derivative detection methods against ours to determine whether an improvement in measurement accuracy is gained. Furthermore, phase-plane plot annotations can be generated, as displayed on the right, to determine where the third derivative peak detection is in dV/dt vs voltage space.

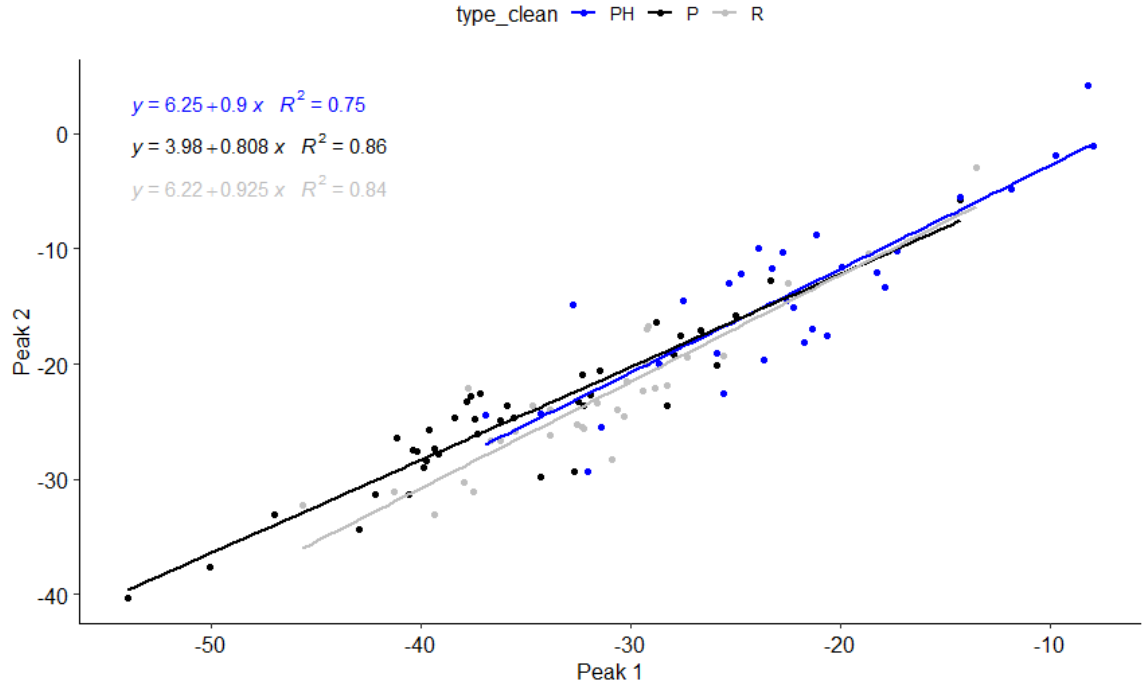


Figure 2.4: Analysis of Third Derivative Peak 1 and Peak 2 Thresholds in Heterogeneous Auditory Neurons.

Analyzing three subsets of a heterogeneous firing population of MSO neurons (prehearing – blue [**PH**]; post hearing phasic/single AP neurons [**P**]– black; post hearing repetitive neurons [**R**] – grey). Amplitudes at which first and second peak appear are directly correlated. Populations generally exist in discrete spaces along trend lines, with small phasic (black) neurons at more hyperpolarized amplitudes for both the first and second peaks. With neurons that fire more repetitively, both peaks occur at more depolarized amplitudes.

Chapter 3: Physiological diversity influences detection of stimulus envelope and fine structure in neurons of the medial superior olive

Brian J. Bondy^{1,2*}, David B. Haimes^{1,2*}, and Nace L. Golding^{1,2‡}

Department of Neuroscience, University of Texas at Austin, Austin, TX 78712
Center for Learning and Memory, University of Texas at Austin, Austin, TX 78712

‡To whom correspondence should be addressed

* These authors contributed equally to the work.

Corresponding author:

Nace L. Golding: University of Texas at Austin, Department of Neuroscience and Center for Learning and Memory, 1 University Station C7000, Austin TX 78712-0248, golding@austin.utexas.edu.

Number of pages: 45

Number of figures and tables: 8 figures, 0 tables.

Number of words: Abstract 199; Significance 119; Introduction 500; Methods 1812; Results 2602; Discussion 1579.

Conflict of interest: The authors report that they have no conflicts of interest.

ACKNOWLEDGEMENTS

This work was supported by NIH grants DC006788 (N.L.G.), F31 DC016525 and a Donald D. Harrington graduate fellowship (B.J.B), and F31 DC017377 (D.B.H). The authors would like to thank Dr. Matthew Rasband (Baylor College of Medicine) for kindly providing immunolabeling advice and the antibodies to Nav1.6 and AnkyrinG, Kenneth Ledford for assistance in writing code for data acquisition and analysis, and Dr. Michael Roberts for helpful discussions during early experiments, as well as collecting the phasic neuron *in vitro* ITD tuning data.

AUTHOR CONTRIBUTIONS STATEMENT

D.B.H performed the AIS immunohistochemistry and analyzed the resulting data. All other experiments were performed by B.J.B, and both B.J.B and D.B.H. analyzed the data. All figures were produced by B.J.B, D.B.H, and N.L.G. and B.J.B wrote the main manuscript text. All authors edited the manuscript.

ABSTRACT

The neurons of the medial superior olive (MSO) of mammals extract azimuthal information from the delays between sounds reaching the two ears (interaural time differences, or ITDs). Traditionally, all models of sound localization have assumed that MSO neurons represent a single population of cells with specialized and homogeneous intrinsic and synaptic properties that enable detection of synaptic coincidence on a time scale of tens to hundreds of microseconds. Here, using patch-clamp recordings from large populations of anatomically labeled neurons in brainstem slices from male and female Mongolian gerbils (*Meriones unguiculatus*), we show that MSO neurons are far more physiologically diverse than previously appreciated, with properties that depend regionally on cell position along the topographic map of frequency. Despite exhibiting a similar morphology, neurons in the MSO exhibit sub-threshold oscillations of differing magnitudes that drive action potentials at rates between 100-800 Hz. These oscillations are driven primarily by voltage-gated sodium channels and are distinct from resonant properties derived from other active membrane properties. We show that graded differences in these and other physiological properties across the MSO neuron population enable the MSO to duplex the encoding of ITD information in both fast, sub-millisecond time varying signals as well as slower envelopes.

SIGNIFICANCE STATEMENT

Neurons in the medial superior olive (MSO) encode sound localization cues by detecting *microsecond* differences in the arrival times of inputs from the left and right ears, and it has been assumed this computation is made possible by highly stereotyped structural and physiological specializations. Here we report using a large (>400) sample size that MSO neurons show a strikingly large continuum of functional properties despite exhibiting similar morphologies. We demonstrate that subthreshold oscillations mediated by voltage-gated Na⁺ channels play a key role in conferring graded differences in firing properties. This functional diversity likely confers capabilities of processing both fast, submillisecond-scale synaptic activity (acoustic “fine structure”), and slow-rising envelope information that is found in amplitude modulated sounds and speech patterns.

INTRODUCTION

Neurons of the medial superior olive (MSO) compare the arrival time of low-frequency sounds between two ears (interaural time differences, or ITDs), signaling the relative timing of binaural synaptic inputs with changes in firing rate (Goldberg and Brown, 1969; Yin and Chan, 1990) . The MSO provides an especially clear example of a neural representation of a sensory feature, with neurons tuned to different ITDs representing discrete horizontal locations. Additionally, the MSO is a system where there is a strong relationship between circuitry, the biophysical properties of single cells, and a neural computation.

The original model for ITD tuning, the Jeffress model, postulated an array of identical neurons whose ITD and frequency tuning is based solely on their respective inputs (Jeffress, 1948), and where systematic variations in axon length impart sensitivity to ITDs. The Jeffress model well describes the computation of the avian analog of the MSO, the nucleus laminaris (NL) (Carr and Konishi, 1988; Carr et al., 2015). However, the NL deviates from the Jeffress model in that there are striking differences in intrinsic electrical properties along the nucleus's tonotopic axis that have been proposed to aid effective neural coding over different frequency ranges. These gradients include intrinsic electrical properties (Koppl, 1994; Fukui and Ohmori, 2004; Wang et al., 2017) as well as dendritic (Smith and Rubel, 1979; Sanes et al., 1990) and axon initial segment morphology (Kuba et al., 2005; Kuba, 2012).

The Jeffress model does not appear to describe ITD processing in the mammalian MSO nearly as well as in its avian counterpart. Axonal labeling has revealed a lack of systematic axonal delay lines from the cochlear nucleus to the MSO (Karino et al., 2011), leading to the postulation of several other sources of internal delay (Brand et al., 2002; Joris and Yin, 2007). Evidence for a systematic map of ITD tuning is likewise weak (Yin and Chan, 1990), and evidence for tonotopic gradients of neuronal properties in the MSO, akin to those seen in the NL has been conflicting (Scott et al., 2007; Baumann et al., 2013). A further complication in the mammalian circuitry is the presence of so called “non-principal” neurons in the MSO, defined mostly on the basis of anatomical criteria (Stotler, 1953; Scheibel and Scheibel, 1974; Henkel and Spangler, 1983). What little data exists on the physiology of these cells suggests that they are less temporally precise than principal

neurons (Smith, 1995; Chirila et al., 2007). These cells have not been incorporated in any model of MSO processing.

Here, we have examined electrophysiological and anatomical features of cells in the gerbil MSO, with special emphasis on extensive sampling and localization along its 3-dimensional volume. Our data reveals a surprising and previously undescribed heterogeneity of intrinsic membrane and firing properties. Physiological and morphological features of MSO neurons do not define distinct “cell types”, but instead create a continuous spectrum of response characteristics which may enhance the detection and encoding of information of sounds with a broad range of rise times and other temporal features.

MATERIALS AND METHODS

All procedures were conducted in accordance with the Institutional Animal Care and Use Committee at The University of Texas at Austin, following guidelines of the National Institutes of Health. Mongolian gerbils (*Meriones unguiculatus*) were raised in a colony at the UT-Austin Animal Resource Center and maintained on a 50/50 day/night cycle with continual access to food and water.

Brain slice preparation. Approximately equal numbers of both male and female Mongolian gerbils (45% males and 55% females out of 330 animals that were documented) were anesthetized with isoflurane then decapitated after reflexes had ceased. Brains were removed in ACSF and a coronal blocking cut was made midway through the superior colliculus. For gerbils age P18-22, all steps were carried out in artificial cerebrospinal fluid (ACSF) warmed to 35°C, containing: 125mM NaCl, 25mM D-Glucose, 2.5mM KCl, 25mM NaHCO₃, 1.25mM NaH₂PO₄, 1.5mM MgSO₄, 1.5mM CaCl₂ (pH adjusted to 7.45 with NaOH, final osmolarity: 315mOsm). Slices were cut at 200 μm thickness, incubated in ACSF at 35° C for 30-45 min., and then cooled to room temperature for >30 min. Slicing typically produced 6-8 slices containing MSO. Following the preparation of slices, the sections immediately preceding and following the MSO were fixed for later reconstruction of the boundaries of the nucleus. ACSF for dissections and recordings was bubbled continuously with 95% O₂/5% CO₂. Dissections for gerbils older than P22 were carried out at room temperature. Following isoflurane anesthesia gerbils were perfused and subsequently sectioned in a Na⁺-free solution containing: 135mM N-Methy-D-Glucamine (NMDG), 20mM D-Glucose, 1.25mM KCl, 1.25mM KH₂PO₄, 2.5mM MgSO₄, 0.5mM

CaCl₂, and 20mM Choline Bicarbonate (pH adjusted to 7.45 using NMDG powder, final osmolarity: 310mOsm). Slices were incubated at 35°C in a recovery solution: 110mM NaCl, 25mM D-Glucose, 2.5mM KCl, 25mM NaHCO₃, 1.25mM NaH₂PO₄, 1.5mM MgSO₄, 1.5mM CaCl₂, 5mM N-Acetyl-L-Cystine, 5mM Sodium ascorbate, 3mM sodium pyruvate, and 2mM Thiourea (pH adjusted to 7.45 with NaOH, final osmolarity: 310) for 30-45 minutes, then moved to room temperature for >30 minutes before recording.

Electrophysiology. Whole-cell current-clamp recordings were made using Dagan BVC-700A amplifiers. Membrane voltage was filtered at 5 kHz, digitized at 50–100 kHz, and acquired using custom algorithms in IgorPro (WaveMetrics). Recording electrodes were pulled from thick-walled borosilicate glass (1.5/0.86mm OD/ID; 4-8MΩ) and filled with intracellular solution containing 115 mM K-gluconate, 4.42 mM KCl, 0.5 mM EGTA, 10 mM HEPES, 10 mM, Na₂Phosphocreatine, 4 mM MgATP, and 0.3 mM NaGTP, osmolality adjusted to 300 mOsm/L with sucrose, pH adjusted to 7.30 with KOH. Biocytin (0.1%) was added to allow for cell labeling. All membrane potentials shown in this paper are corrected for a 10 mV junction potential. Bridge balance and capacitance compensation were monitored in all recordings. All recordings were carried out at 35° C with oxygenated ACSF perfused at a rate of ~2-4 mL/min.

Data analyses for electrophysiology. Measurements of action potential shapes were made at rheobase. Rheobase spikes were acquired by finding a current step amplitude that would evoke an AP ~50% of the time. In most cases, at least 25 spikes were collected for analysis.

In vitro ITD experiments were carried out using custom code written in IGOR-Pro (Wavemetrics) using methods described previously (Roberts et al., 2013). Bilateral

synaptic stimuli with different timing offsets were presented randomly and interleaved with unilateral stimuli and current steps (input resistance measurements). Synaptic stimulation was performed using a constant current stimulator (Digitimer DS3) and glass electrodes with 50-100 μm tips placed on the near the LNTB for ipsilateral inhibitory stimulation, or near the center of the MNTB for contralateral inhibitory stimulation. Excitatory and inhibitory responses were isolated by adding 1 μM strychnine or 10 μM NBQX to the ACSF, respectively. Stimulation strength was adjusted so that ipsi- and contralateral evoked EPSPs were roughly equal in amplitude. Stimulation intensity was also adjusted so that AP probability at the best timing offset was close to, but less than 100%, to avoid saturation. *In vitro* ITD curves were normalized to maximal firing probability. Since stimulus-driven synaptic delays were dependent on electrode placement and thus arbitrary, the x axes of ITD curves were offset so that maximal firing probability was 0 ms ITD. To obtain averaged ITD curves from experiments where different offset intervals were used, all curves were resampled to a common time scale in 0.05 ms increments using a linear interpolation.

Fast Fourier transforms (FFTs) were carried out in IGOR to measure the frequency of membrane oscillations. The average voltage was used to plot the FFT vs membrane potential. Heatmaps were generated in Matlab, and smoothed by interpolating points at 1 Hz intervals, and at intervals $1/10^{\text{th}}$ of the existing voltage steps. Plots in the frequency domain were created by measuring the FFT of cell voltages depolarized to 2-7 mV below the cell's AP threshold, typically over a window of 60 ms. Some tonic neurons required larger windows due to the slower oscillations, in which case voltage in the frequency

domain was normalized to account for the extra time. For measurements of the change in voltage frequency with drug application (**Figure 3.7F**), voltage in the frequency domain was measured by integrating the values of the FFT in a 100 Hz window around the peak frequency. In other experiments, resonance frequency was measured from the peak of the impedance vs. time plot calculated from the voltage responses to a chirp current injection (~5 mV peak depolarization, 10s long at -60 mV). The frequency of the chirp increased linearly from 0 to a maximum value that was adjusted so that the resonant frequency occurred near the middle of the chirp.

Principal component analysis, and group analyses were performed in Rstudio (R 4.0.4). Briefly, 31 features were chosen for PCA, 12 electrophysiological and 19 morphological. Separate datasets were constructed for each feature and subjected to MICE (Multiple Imputation by Chained Equations) imputation to account for occasional missing measurements in some cells (mice v3.11.0) (van Buuren, 2001). Briefly, MICE imputation involves estimating missing data by performing linear regression on existing data and then predicting possible values. Multiple datasets are generated from these possible values, with pooling of these results leading to a single, final dataset. Data was centered and scaled with principal component analysis (stats v3.6.3) and visualized (factoextra v1.0.7).

Immunostaining. Following isoflurane anesthesia, the brainstems of Mongolian Gerbils (P22-28) were rapidly removed and drop fixed for 30-60m in ice-cold 4% paraformaldehyde. Brains were transferred to 20% Sucrose (in 0.1M PBS) overnight at 4°C, followed by a second night in 30% Sucrose. The tissue was sectioned on a cryostat at 20-35µm, then transferred to 0.1M PBS, mounted and dehydrated. For

immunohistochemistry, slides were rehydrated in 0.1M PBS for 10-15 min. and covered with phosphate buffer/Triton/Goat serum blocking solution (PBTGS; 10% goat serum, 0.3% Triton in 0.1M PBS) for 1.5 hours. The tissue was incubated (24-48 hours 4°C) with PBTGS containing mouse anti-HCN1 (1:200 – Neuromab) and either 1:100 rabbit anti-Nav1.6 or 1:200 rabbit anti-ankyrin-G (Courtesy of Dr. Matthew Rasband; Baylor College of Medicine). After primary incubation, the tissue was gently washed 3x with 0.1M PBS (5,10,15 min intervals) at RT and then incubated for 2 hours with PBTGS containing 1:250 goat anti-mouse Alexa568 (1:250; Abcam) and goat anti-rabbit Cy2 (1:250; Jackson Labs). Following secondary incubation, tissue was again washed 3x with 0.1M PBS. The third wash (15 min) was done in 0.05M PBS, dried and cover slipped with Fluoromount-G (Thermo Fisher).

Imaging. Images were taken on a Leica LSM (Leica TCS SP5 II) confocal microscope. Large images of the entire MSO were taken using tile scanning and z-stacks with an average of 0.7 μ m thin optical sections. Image parameters were set to provide sub-saturation of pixels in the axon initial segment. Fluorescence was excited by 488 and 543 nm lasers. Images were then reconstructed on NeuroLucida 360, and ankyrin-G positive AISs were demarcated by 20% maximal fluorescence cutoffs at the proximal and distal ends. Linear pixel plots, also known as Intensity Profiles (spatial distribution of pixel intensities within an image), were generated using a rolling average across the width of the AIS to help determine cutoffs. Measurements were also made between the axon emergence point on the soma or proximal dendrite, and the start of the fluorescent signal at the proximal end

of the AIS. Data from each individual tracing was plotted against relative location across the dorsal-ventral axis of the MSO.

Histology. In order to determine the precise ventral-dorsal position of each recorded neuron, cells were labeled by including 0.1% biocytin in the internal solution and post-experimental processing. Following each recording, the MSO and pipette location were either sketched under low power or imaged directly, after which the brain slices were stored in 4% PFA for 24-48 hours before being switched to a 1X PBS solution. Biocytin staining on 200 μm slices was performed using ABC and DAB staining kits from Vector Laboratories and processing was carried out according to the manufacturer instructions. Slices were mounted on slides using Mowiol mounting agent. Coverslips were sealed using nail polish after drying. Cells were reconstructed using a 100x objective and the SOC as well as other brain nuclei were traced using 4x or 10x objectives (Olympus BX51 light microscope) using NeuroLucida software. Truncated dendritic arbors were excluded unless the ending occurred $>100 \mu\text{m}$ from the soma. Low power drawings of slices, together with measurements of ventral-dorsal location were used to determine the identity of cells after biocytin staining was performed, in the event that not all recorded cells labeled properly. Biocytin staining typically produced a clear background labeling of the superior olivary complex nuclei, which was used to create a rough outline of the MSO under low power. Subsequently, ventral and dorsal ends of this outline were investigated under 100x magnification for any spindle-shaped cell bodies, which were traced. The absence of these spindle-shaped cell bodies was used as a further marker for the boundaries of the MSO, particularly for the dorsal end of the MSO. The ventral border of the MSO is marked by a

large fiber tract that separates the MSO from the ventral nucleus of the trapezoid body (VNTB), and often provided a very clear border. Thus, a combination of these fiber tracts, the locations of the LSO and VNTB, and the locations of spindle shaped neurons were used to determine the boundaries of the MSO. Since the ventral-dorsal length of the MSO varies along its rostral-caudal axis, ventral dorsal position is expressed as a cell's position along the normalized length of the MSO within a given slice. Any cell found to be outside of the marked region was excluded from all analyses.

Statistics. In all experiments, values are presented as mean \pm SEM, and statistical significance was assessed using a non-parametric ANOVA (Kruskal-Wallis) across the three firing types. Subsequent pairwise comparisons were performed using a two-sided Wilcoxon test. P values with no test specified are from the Wilcoxon test. Effect size is reported as Hedges's g value. Significance level was set at 0.05. Normality of distributions was not assumed. Numbers of replications of experiments are equal to the number of cells recorded/analyzed.

Data. The data is available at https://github.com/dhaimes-b/MSO_CellType_Diversity (commit f143e96).

RESULTS

To assess whether there are topographic differences in the physiology or morphology of MSO neurons, we made whole-cell recordings from 422 MSO neurons in coronal brainstem slices from gerbils of postnatal ages 18-68 days (P18-68), and

subsequently localized labeled neurons within the 3 dimensions of the nucleus through biocytin staining. Up to nine neurons were recorded across the tonotopic (ventral-dorsal) axis in a single slice, and as many as 16 cells could be recorded across multiple slices from a single gerbil. Out of the group of coronal slices, 337 were labeled well enough to localize within the MSO, and 270 of these neurons could be reconstructed fully. A further 72 cells recorded in horizontal slices were included in this study, but cell location data was not collected for these neurons.

MSO neurons have a continuum of diverse physiological properties

In our experiments, we observed a diversity in physiology and morphology not previously reported. We observed three general patterns of firing in response to step injections of current, although there was no discrete boundary between firing types. Figure 1A shows two examples from each group of neurons. 63% of cells displayed properties consistent with previous reports from MSO principal neurons, which we term “phasic neurons”: a single action potential (AP) in response to intracellularly injected current steps, a single phase afterhyperpolarization (AHP), a fast membrane time constant (Phasic (n=292): $\tau_m = 0.319 \pm 0.005$ ms), and low input resistance (Phasic (n=292): 10.5 ± 0.2 M Ω) (**Figure 3.1A,B,E; black traces or points**). We also observed a subset of neurons that fired repetitively, which we separated into two groups based on the pattern and shape of their APs, the “oscillator neurons” and “tonic neurons”.

Oscillator neurons (n=97) fired high-frequency AP trains at the beginning of the response to steps of current, followed by a period of silence marked by large, high-

frequency subthreshold oscillations (**Figure 3.1A,C; blue traces**). In roughly half of oscillator neurons these oscillations gave way to high-frequency spiking during responses to larger amplitude steps, with each AP displaying a single phase AHP. Any neuron that fired more than one AP in response to a current step was considered an oscillator neuron, unless it fit the criteria of a tonic neuron (see below). Oscillator neurons exhibited input resistances and time constants 3-5 times larger than phasic neurons (R_{in} , $34.6 \pm 2.69 \text{ M}\Omega$, $n=101$; τ_m , $0.94 \pm 0.09 \text{ ms}$, $n=74$, **Figure 3.1E**). APs in oscillator neurons were larger than phasic neurons (Oscillator ($n=95$): $68.3 \pm 0.8 \text{ mV}$ vs. Phasic ($n=253$): $34.9 \pm 0.8 \text{ mV}$, $p=6.27e-45$, $g=2.79$, **Figure 3.1F**), and exhibited a relatively higher voltage threshold for initiation (Oscillator ($n=95$): $-40.9 \pm 0.7 \text{ mV}$ vs. Phasic ($n=248$): $-46.5 \text{ mV} \pm 0.3 \text{ mV}$, $p=3.57e-18$, $g=1.12$, **Figure 3.1G**) despite a smaller rheobase (Oscillator ($n=95$): $585 \pm 20 \text{ pA}$ vs. Phasic ($n=253$): $1991 \pm 48 \text{ pA}$, $n=253$, $p=2.97e-47$, $g=2.22$). Finally, in response to subthreshold chirp stimuli ($\sim 5 \text{ mV}$ peak depolarization, 10s long; See Methods), oscillator neurons displayed maximal resonance at a lower frequency than phasic neurons (Oscillator ($n=42$): 100 Hz vs Phasic ($n=97$): 310 Hz , $p=4.61e-18$, $g = 2.77$; **Figure 3.1H**.)

Tonic neurons ($n=68$) fired more regularly and at lower frequency in response to current steps compared to oscillators (**Figure 3.1**, red vs. blue traces) and individual APs exhibited a distinctive two-phase AHP (**Figure 3.1D**). Any MSO neuron that fired repetitively and displayed a two-phase AHP was considered a tonic neuron. Tonic neurons ($n=50$) exhibited input resistances and time constants 3-5 fold higher than oscillator neurons (R_{in} , $102.4 \pm 10.5 \text{ M}\Omega$, $p=1.40e-20$, $g=1.15$; τ_m , $4.38 \pm 0.72 \text{ ms}$, $p=3.26e-13$, $g=1.04$; **Figure 3.1E**). AP threshold in tonic neurons was also elevated compared to phasic neurons

(Tonic (n=65): -42.4 ± 0.66 mV, $p=2.22e-9$, $g = 0.85$), despite far lower rheobase currents (Tonic (n=65): 287 ± 22 pA vs 1991 ± 48 pA, $p=6.34e-41$, $g = 2.53$), and were also significantly different from oscillator neurons' threshold ($p=8.22e-18$, $g=1.62$; **Figure 3.1G**). While oscillator neurons had a similar resting potential (V_{rest}) compared to phasic neurons (Oscillator (n=95): -60.2 ± 0.4 mV n=100 vs. Phasic (n=253): -59.1 ± 0.19 mV, $p=1.41e-2$, $g=0.38$), V_{rest} in tonic neurons was more negative (Tonic (n=65): -65.5 ± 0.72 mV, Tonic vs Oscillator, $p=2.98e-9$, $g=1.03$, Tonic vs Phasic, $p=1.35e-19$, $g=1.64$). These differences in V_{rest} further accentuated the differences in AP threshold relative to rest (Phasic (n=253): 12.7 ± 0.23 mV, Oscillator (n=95): 19.1 ± 0.48 mV, Tonic (n=65): 23.1 ± 0.64 mV, Kruskal-Wallis, $p=3.08e-47$, Phasic vs Oscillator: $g = 1.63$, Phasic vs Tonic: $g = 2.57$, Oscillator vs Tonic: $g = 0.77$).

While many physiological parameters showed systematic differences in properties across firing types, there was a high degree of overlap in values (**Figure 3.1E-H, All Category**). Neurons with intermediate properties were common. Oscillators without late APs tended to have properties more similar to phasic neurons. Many phasic neurons displayed overshooting APs (**Figure 3.1A**, right example) and some displayed noticeable subthreshold oscillations (data not shown).

While the majority of the neurons in this data set were recorded at P18-28 (Phasic, n=250; Oscillator, n=81; Tonic, n=65), all of these firing phenotypes were observed in older animals between P28 to P68, when both morphological and physiological features of MSO neurons have reached stability (Rautenberg et al., 2009; Mathews et al., 2010; Khurana et al., 2012) (Phasic, n=23; Oscillator, n=16; Tonic, n=3). We found that

electrophysiological features from this older age range fell within the range of values observed in animals from P18-P28 (e.g., first/third quartiles, mean; **Figure 3.2A**), although the large imbalances in sample sizes precluded formal statistical comparisons. When cells with phasic, oscillating and tonic firing patterns were compared using principal components analysis (PCA) of 12 primary electrophysiological parameters, the distributions were overlapping and formed a bimodal continuum (**Figure 3.2B**). Thus, electrophysiological criteria alone do not support phasic, oscillator and tonic neurons as distinct cell types within the MSO neuron population.

All MSO neurons are principal neurons

Figure 3.3A-D illustrates 4 example brainstem slices with reconstructed neurons. The yellow spindle shapes are non-labeled cell bodies that were marked under 100x magnification to aid in demarcating the boundaries of the MSO (see Methods). As with phasic neurons, oscillator and tonic neurons were located in the main column of cell bodies. In two cases, neurons were recorded outside of the cell body layer and in the indistinct territory between the MSO and neighboring nuclei like the LNTB. These cells were morphologically and physiologically distinct from the neurons described here and were not included in our analyses. While some dorsal oscillator and tonic neurons did not display an obvious bipolar dendritic architecture (red cell, **Figure 3.3B**), most cells displayed morphologies that have been described previously. Phasic neurons (n=220) were generally located throughout the nucleus, while oscillator and tonic neurons (oscillator, n=84; tonic, n=65) tended to be biased towards the dorsal and ventral ends of the nucleus (**Figure 3.3E**).

Furthermore, two cells with different firing types could be recorded directly adjacent to each other (**Figure 3.3A,D**), and all three firing types could be recorded in the same slice (**Figure 3.3A**).

The axons of phasic MSO neurons typically traveled dorsally, passing either between the superior periolivary nucleus (SPN) and the lateral superior olive (LSO) or through the SPN, en route to the inferior colliculus (**Figure 3.3A-D**, black neurons). The axons of oscillator and tonic neurons (**Figure 3.3A-D**, blue and red neurons) took a similar path. Many phasic neuron axons took a roundabout path out of the nucleus, often traveling ventral for some distance before turning dorsal (see **Figure 3.3C**, topmost neuron and D, most ventral phasic neuron). This pattern was also seen in oscillator neurons (**Figure 3.3A,C**) and tonic neurons (data not shown). As with phasic neurons, oscillator and tonic neurons' axons frequently sent local collaterals within the MSO, as well as collaterals in the SPN. All MSO neurons projected outside of the nucleus, indicating that there were no pure interneurons/non-principal neurons in the MSO. There were no axons that could be traced dorsal to the LSO (**Figure 3.3B**).

Dendritic morphology is a poor indicator of firing type

Although prior studies have highlighted the presence of discrete morphological cell types in the MSO (Stotler, 1953; Scheibel and Scheibel, 1974; Henkel and Spangler, 1983), quantitative analyses of 270 biocytin-labeled neurons revealed that dendritic morphology can vary across MSO neurons, and is an imperfect indicator of firing type (**Figure 3.4A-D**). Most MSO neurons exhibited a bipolar architecture with a similar pattern of tapering, dendritic length, and general complexity. It was observed that a small number of oscillator

and tonic neurons with longer dendritic arbors were present, particularly at the dorsal end of the nucleus, although many of these were excluded from analyses due to incomplete dendritic arbors. Overall however, there were no systematic differences in anatomical parameters along the tonotopic axis (Mean dendritic length: Phasic $R^2=0.013$, Oscillator $R^2=0.130$, Tonic $R^2=0.028$; Number of branch points: Phasic $R^2=0.016$, Oscillator $R^2=0.001$, Tonic $R^2=3e-04$) (**Figure 3.4B,C**). Principal component analysis on imputed data (see Methods; $n=223$ cells; 19 features), showed strong overlap of each firing type with solely morphological features (data not shown, but available at https://github.com/dhaimes-b/MSO_CellType_Diversity). Combining these morphological features with the electrophysiological features (**Figure 3.2B**), produced slightly more group separation in principal component analysis ($n=200$ cells; 31 features: 12 electrophysiological, 19 morphological), although strong overlap still existed (**Figure 3.4D**). Taken together, the anatomical results indicate that there are no strong trends in morphology along the tonotopic axis, and overall the data do not support the existence of separable anatomical cell types.

Oscillator and tonic neurons have slower synaptic kinetics

MSO neurons from all three firing types received bilateral excitation (**Figure 3.5A**). Electrical stimulation of bushy cell axons from the cochlear nucleus evoked EPSPs that were widest in tonic neurons, and narrowest in phasic neurons (Halfwidth: Phasic ($n=14$), 0.52 ± 0.015 ms; Oscillator ($n=14$), 1.42 ± 0.21 ms; Tonic ($n=6$), 3.74 ± 0.77 ms. Kruskal-Wallis $p=1.1e-05$, Wilcoxon: Phasic vs Oscillator $p=5.6e-05$, Phasic vs Tonic $p=2.1e-4$, Oscillator vs Tonic $p=4.0e-05$). The kinetics of EPSPs strongly

influenced a given neuron's sensitivity to the coincidence of bilaterally evoked synaptic input (**Figure 3.5A**). Oscillator and tonic neurons more readily summed inputs with larger timing offsets. Few phasic neurons fired APs in responses to timing offsets above 0.5 ms. By contrast, every tonic neuron recorded could fire in response to time differences greater than 1 ms, with one neuron firing to time differences as large as 5 ms. The slopes of these *in vitro* ITD tuning curves were 2.5- and 7-fold steeper in phasic neurons relative to oscillator and tonic neurons, respectively (**Figure 3.5B,C**: slope of sigmoid fit: phasic neurons, $0.056 \pm 0.004 \text{ ms}^{-1}$; oscillator neurons, $0.135 \pm 0.019 \text{ ms}^{-1}$; tonic neurons, $0.41 \pm 0.17 \text{ ms}^{-1}$). ITD functions were narrowest in phasic neurons and widest in tonic neurons (**Figure 3.5B,D**), and ITD width was highly correlated with input resistance (**Figure 3.5E**, Linear regression, $F(1,30)=83.51$, $p=3.57e-10$, $R^2=0.86$).

Axon initial segment morphology is uniform across the MSO

The axon initial segment (AIS) possesses a high density of voltage-gated Na^+ and K^+ channels and is typically the site of spike generation. Thus, variations in AIS length, diameter and proximity to the soma could potentially contribute to the different spike thresholds and firing patterns observed across MSO cells. To determine if the AIS varies with functional firing phenotypes, we quantified AIS morphology as a function of tonotopic location in the MSO in fixed coronal sections of the MSO (**Figure 3.6**). Dual immunolabeling of the AIS marker ankyrin-G and hyperpolarization-activated cyclic nucleotide gated (HCN) channels (the latter to visualize the soma), revealed that the AIS was highly uniform along the tonotopic axis both in its length ($17.8 \pm 0.1 \text{ } \mu\text{m}$ $n=833$) as well

as its starting location in the axon with respect to edge of the soma ($<0.2\pm 0.012\ \mu\text{m}$; **Figure 3.6A,C,E-G**). Further, dual immunolabeling with antibodies to Nav1.6 and HCN1 subunits showed that Nav1.6 was not present in the most proximal portion of the AIS, consistent with a prior study (**Figure 3.6B,D**)(Ko et al., 2016). This proximal spacer in the Nav1.6 signal, and the total length of the Nav1.6 segment, were also uniform across the tonotopic axis (**Figure 3.6E-G**).

Subthreshold voltage oscillations are mediated by fast Na^+ channels.

Subthreshold oscillations were a feature of all MSO neurons regardless of firing pattern but differed in amplitude and frequency (**Figure 3.7**). Oscillations in phasic neurons were small ($<1\ \text{mV}$) and high in frequency (400-800 Hz; **Figure 3.7A**, black traces), whereas in both oscillator and tonic neurons oscillations were far more prominent (**Figure 3.7A**, blue and red traces). In tonic neurons, oscillations were often difficult to visualize because they occurred only over a narrow range of voltages just below AP threshold. Spectral analyses of oscillations at different membrane potentials showed that oscillation frequency increases with the square of membrane potential monotonically, with all firing types forming a continuum (**Figure 3.7B-C**). In tonic and oscillator neurons, subthreshold oscillations and firing frequency were distinctly correlated: this was most easily visualized in oscillator neurons, where subthreshold oscillations and AP trains of similar frequencies could be measured in individual responses (**Figure 3.7D**). Finally, oscillations were eliminated by application of $1\ \mu\text{M}$ tetrodotoxin (TTX) either to the bath or locally to the

soma and axon (90-95% reduction in power, see Methods; **Figure 3.7E**), indicating that oscillations were driven primarily by voltage-gated Na⁺ channels, regardless of firing type.

Reduced slope sensitivity allows oscillator and tonic neurons to respond to AM-like stimuli

The striking differences in membrane and firing properties of MSO neurons raise the question of what functional significance such diversity may play in encoding binaural information, particularly in high-frequency regions of the MSO. One possibility is that such properties represent adaptations to detect low-frequency envelopes of high-frequency, amplitude modulated (AM) sounds. To test this, we injected current into neurons in the shape of a fully rectified sine wave. This stimulus was designed to approximate the pattern of synaptic summation experienced by MSO neurons *in vivo* in response to AM sounds, based on known responses of bushy cells in the cochlear nucleus (Frisina et al., 1990). The frequency and amplitude of simulated envelopes were varied systematically in order to determine how different neurons responded to inputs that produced slow or fast rising voltage responses.

Phasic neurons showed markedly different responses to these simulated envelopes, compared to oscillator and tonic neurons (**Figure 3.8A-C**). Phasic neurons typically would not fire in response to envelopes below 100 Hz. Often, APs could not be evoked on the first several cycles of a 100 Hz envelope, regardless of current amplitude (up to 6.5 nA). The current threshold for evoking APs decreased as the frequency of the envelope increased up to 400-600 Hz. At higher frequencies, spiking became more difficult to evoke,

likely due to depolarization block (see elevated membrane potential in **Figure 3.8A**, 1000 Hz phasic neuron).

Both tonic and oscillator neurons responded to simulated envelopes across a broad range of frequencies (**Figure 3.8C,D**). In some oscillator neurons, firing thresholds became elevated at lower frequencies, with several neurons showing low-frequency cut-offs (**Figure 3.8D**). Oscillator and tonic neurons differed dramatically from phasic neurons in their ability to fire multiple APs per cycle at envelope frequencies at and below 200 Hz. In many cases, this resulted in oscillator and tonic neurons firing the same number of APs per second-long envelope stimulus, regardless of frequency (e.g., **Figure 3.8C**, overlapping curves for tonic neuron). With the exception of the slowest tonic neurons, most MSO neurons could fire APs at the envelope frequency 1:1 for frequencies up to 600-800 Hz.

The characteristic subthreshold oscillations in oscillator neurons were particularly prominent during low-frequency envelope injections. **Figure 3.8B** shows an example response of an oscillator to a 10 Hz envelope at several current amplitudes. These oscillations reached peak amplitude at voltages close to threshold. At suprathreshold voltages, oscillations preceded spiking, could exceed 6 mV in amplitude, and typically drove subsequent repetitive spiking. Large oscillations were also seen in tonic neurons during envelope current injections, although in most cases the voltage range between the emergence of oscillations and spiking was narrow.

DISCUSSION

Traditionally, the binaural neurons of the MSO have been assumed to comprise a highly stereotyped cell type, with sub-millisecond membrane properties, transient firing pattern and bipolar dendritic morphology. Here, we show in a large sample of neurons and detailed mapping of sub-nucleus location that the functional properties of MSO neurons are strikingly variable, and that a substantial proportion of neurons in the MSO exhibit functional properties incompatible with the classic model of MSO processing. Specifically, subsets of MSO neurons show slower membrane properties as well as high-frequency firing driven by subthreshold voltage oscillations. While MSO neurons can be grouped into descriptive categories based on firing pattern, we found no compelling evidence that these three categories represent fully separable cell types. We show that these disparate properties enable different MSO neurons to detect activity with vastly different rise times, ranging from sub-millisecond *in vitro* ITDs (the traditional role attributed to MSO neurons) to slower rising envelopes over hundreds of milliseconds. Thus, physiological diversity enables the population of MSO neurons to effectively process a wider range of acoustic stimuli than previously recognized.

The MSO contains a single cell type with variable physiological properties.

Previous physiological studies in MSO neurons have defined two cell types in the MSO: the principal neurons, with bipolar dendrites, phasic firing and fast membrane properties (Grothe and Sanes, 1994; Scott et al., 2005; Rautenberg et al., 2009), and non-principal neurons, with stellate morphology, regular firing, and slower membrane

properties (Henkel and Spangler, 1983; Smith, 1995; Chirila et al., 2007). While many of these prior observations were apparent in our recordings, more extensive sampling across the whole tonotopic range of the MSO suggests that these non-principal neurons are not fully distinct from principal neurons (**Figures 3.1-2**). Several lines of evidence support the concept that there is a single cell type in the MSO. The initial trajectories of oscillator and tonic neurons' axonal projections were not different from those of phasic neurons (**Figure 3.3**), showing qualitatively similar patterns in both projection path and collateral targets. Immunohistochemical studies have not shown the presence of neurons expressing glycine or GABA in the MSO, indicating that there are no inhibitory subpopulations (Roberts and Ribak, 1987; Wenthold et al., 1987). All firing types received qualitatively similar patterns of bilateral excitatory and inhibitory synaptic inputs: (**Figure 3.5, for excitatory inputs**).

All firing types could be found at the ventral and dorsal extremes of the nucleus. However, only phasic neurons were seen in the center of the MSO. This trend persisted despite heavy sampling of the middle third of the MSO. The low prevalence of non-phasic neurons in the middle tonotopic range also may explain why non-phasic neurons have been rarely reported in studies of the MSO using horizontal slices, where sampling is likely biased to the middle tonotopic region of the nucleus (Scott et al., 2005; Khurana et al., 2011).

Heterogeneity in intrinsic electrical properties within neural circuits

The variability in properties of specific cell types has sometimes been treated as experimental noise, but theoretical studies have shown that such heterogeneity confers

spiking output that carries higher information content (Padmanabhan and Urban, 2010; Tripathy et al., 2013). Neuronal variability can be the result of a topographic or regional gradient in properties, even outside of sensory and motor systems. Stellate neurons of the medial entorhinal cortex also appear to exhibit positional differences in HCN currents and leak K^+ currents that affect temporal summation, influencing their encoding of grid cell spacing (Garden et al., 2008; Giocomo et al., 2011). Gradients of ion channels along the tonotopic axis are a ubiquitous feature of the avian auditory system. Neurons in the nucleus laminaris display a striking gradient of dendritic morphology along the tonotopic axis (Smith and Rubel, 1979; Sanes et al., 1990), as well as many other features, which have been correlated with improved coding of low vs high-frequency sound information (Fukui and Ohmori, 2004; Kuba et al., 2005; Hong et al., 2018). There are several examples of similar gradients in mammalian auditory nuclei. In the LSO and MNTB, neurons in low-frequency regions fire transiently and express fast intrinsic membrane properties, in part reflecting a higher density of K^+ channels (Barnes-Davies et al., 2004; Brew and Forsythe, 2005). In both avian and mammalian systems, gradients in membrane and firing properties can reflect tonotopic differences in HCN channels (Yamada et al., 2005; Baumann et al., 2013) and/or voltage-gated Na^+ channels (Hong et al., 2018).

Our results differ from the above studies in several important ways. There were no progressive morphological or physiological gradients that were correlated with neuron location in the MSO. In the highest and lowest frequency tonotopic regions, where both phasic and non-phasic firing types were found, neurons with highly disparate properties could be observed in close proximity with one another. We identified no overall systematic

differences in dendritic parameters between neuron classes, despite the fact that a subset of oscillator and tonic neurons in the dorsal, low frequency region of the MSO had unusually long dendrites (**Figures 3.3A, 3.4A**). Sampling in this region was relatively sparse, and thus it is uncertain whether these unusual neurons might play a role distinct from their counterparts in the rest of the MSO neuron column. In the ventral, high-frequency region of the MSO, neurons with completely different functional properties exhibited similar dendritic morphologies, highlighting the critical role of intrinsic conductances in defining functional roles in the binaural circuit.

Mechanisms underlying physiological variation

Numerous studies have established that phasic MSO neurons exhibit extraordinarily fast membrane properties, produced primarily by high expression levels of HCN and Kv1 channels (Koch et al., 2004; Scott et al., 2005; Khurana et al., 2012). It is likely that differences in the expression levels of these channels underlie many of the differences between MSO neurons by affecting input resistance. It is important to note however, that blockade of voltage gated K⁺ channels does not make phasic neurons fire repetitively (Scott et al., 2005), indicating a role for Na⁺ currents. Phasic neurons have small, narrow APs due to the negatively shifted inactivation range of somatic voltage-gated Na⁺ channels, which reduces the percentage of available Na⁺ current at V_{rest} (Scott et al., 2010). Oscillator and tonic neurons have larger, faster rising APs compared to phasic neurons, likely reflecting larger Na⁺ currents underlying spike generation. However, we found that AIS morphology is uniform across the tonotopic axis, with no increase in

variance at the ventral or dorsal ends (**Figure 3.6**). This is in contrast to findings in MNTB principal neurons (Kim et al., 2019). Thus, in the MSO, differences between firing types more likely reflects the subtype distribution, somatic expression levels, and/or modulation of voltage gated Na⁺ channels (Hu et al., 2009), rather than AIS morphology.

A surprising finding in our study is the strong influence of voltage-gated Na⁺ channels in generating large, fast oscillations in MSO neurons. The resonance properties of MSO and other auditory neurons have been shown previously to amplify responses to specific frequency ranges. HCN and K_{LVA} have been implicated as the currents responsible for producing resonance (Remme et al., 2014; Fischer et al., 2018). By contrast, the intrinsic membrane oscillations in this study were actively driven by voltage-gated Na⁺ channels, and the fast gating kinetics of the underlying currents explains why the frequency range of oscillations is higher than that of resonance frequency. We found that oscillations in non-phasic MSO neurons were of far larger amplitude and lower frequency, (100-300 Hz) and could drive firing near or just above the oscillatory frequency (**Figures 3.7A-B, 8D**). As with other electrophysiological parameters, the frequency of oscillations formed a continuum across the full population of MSO cells (**Figure 3.7C**).

Functional implications

The extraordinary biophysical specializations that allow many MSO neurons to detect ITDs in the fine structure of sounds also prevent those neurons from reliably encoding AM and other stimuli with slow rising components (Svirskis et al., 2002; Golding and Oertel, 2012; Lehnert et al., 2014). However, *in vivo* studies in several species,

including cats, guinea pigs, and gerbils, documented the ability of MSO neurons to respond to high-frequency sounds above the phase locking range, and even encode envelope ITDs and sinusoidal AM stimuli (Joris and Yin, 1995; Spitzer and Semple, 1995; Batra et al., 1997; Dietz et al., 2014). Furthermore the MSO is present in many animals that do not hear low-frequency sounds, like monodelphis (Grothe and Pecka, 2014; Bazwinsky-Wutschke et al., 2016), mice (Fischl et al., 2016) and bats (Grothe et al., 1997), and the MSO of certain bat species functions to analyze aspects of AM sounds (Grothe et al., 1997; Grothe and Park, 1998). Finally, humans can detect ITDs in the low-frequency envelopes of high-frequency sounds in psychophysical experiments (McFadden and Pasanen, 1976; Nuetzel and Hafter, 1976; Bernstein and Trahiotis, 1994). The current results resolve these apparent contradictions by demonstrating that there is a subset of neurons in the MSO that are capable of responding to slow voltage changes and, potentially, envelopes. As naturalistic sounds encompass a wide diversity of acoustic waveforms, it follows that there is unlikely a clear distinction between these two modes of coding. Further, the presence of fast-rising synaptic components has been shown to influence encoding of AM-like stimuli, even in phasic neurons (Gai et al., 2010). This work contributes to a growing body of evidence blurring the lines between the supposedly parallel processing in the MSO and LSO (Joris, 1996; Franken et al., 2015; Franken et al., 2018), and further highlights the divergent paths of the mammalian and avian auditory system.

FIGURES

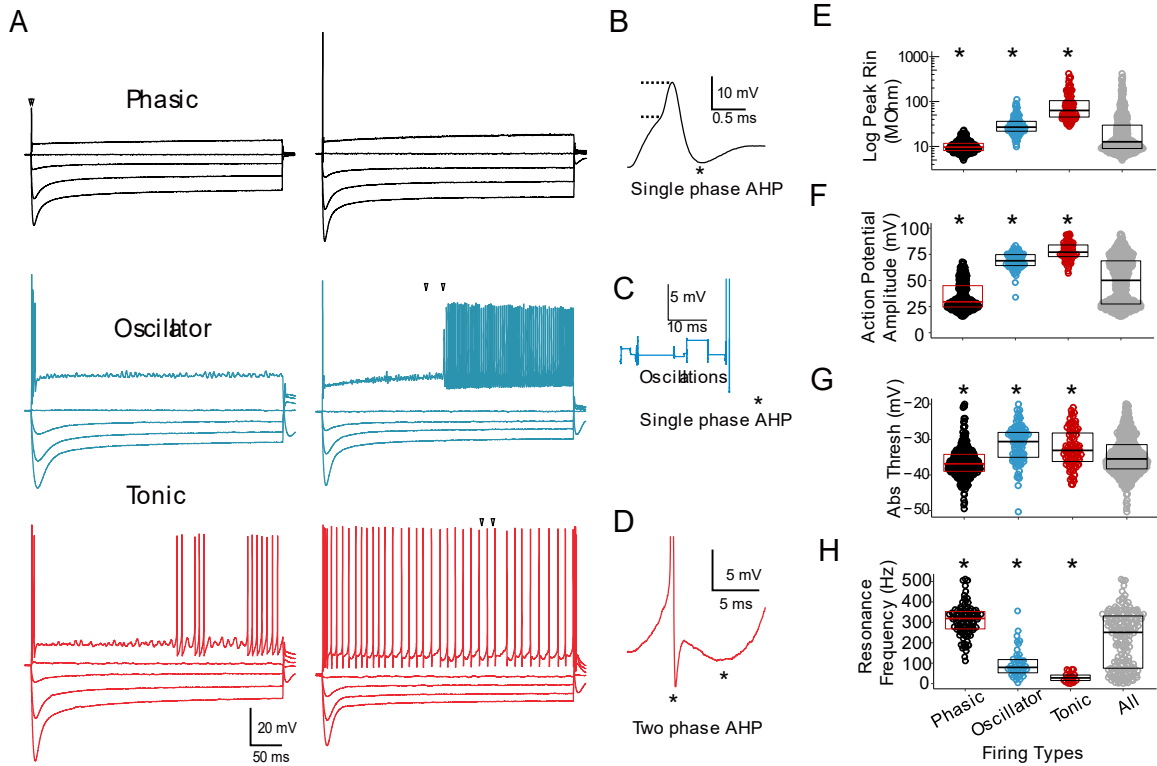


Figure 3.1. MSO principal neurons exhibit a spectrum of membrane properties and firing types. **A.** Six examples of MSO neurons, sorted into three categories. Arrows indicate features displayed in B-D. Top: Phasic neurons with small and large APs (left and right, respectively). Middle: Oscillator neurons with onset-only APs (left), and gap-firing (right). Bottom: Tonic neurons displaying patterns of gap (left) and regular firing (right). **B-D.** Distinguishing features of each category, with one or two-phase afterhyperpolarizations (AHPs) marked by asterisks. **B.** Phasic neurons fire only one AP with a single-phase AHP in response to current steps. Dashed lines indicate AP threshold and peak voltage. **C.** Oscillators fire multiple APs (each with single-phase AHPs), and exhibit large, high-frequency subthreshold oscillations which may evolve into high-frequency spiking. **D.** Tonic neurons show repetitive firing patterns and APs exhibiting two-phase AHPs. **E-H.** Scatter dot plots comparing electrophysiological properties of the three firing types as well as the merged dataset (“All”). Box plots show 1st and 3rd quartiles centered around the mean. Non-parametric statistics: Kruskal-Wallis test for overall differences in the population. Individual group means were then compared against the mean of all groups together with a Wilcoxon Test (asterisk: $p < 0.001$). **E.** Peak input resistance (log scale), measured from the lowest point of the hyperpolarized portion of the IV curve. Kruskal-Wallis, $p = 8.37 \times 10^{-67}$. Wilcoxon: Phasic $p = 1.75 \times 10^{-16}$, Oscillator $p = 4.03 \times 10^{-11}$, Tonic $p = 3.56 \times 10^{-28}$. **F.** AP amplitude (from AP threshold to AP peak). Kruskal-Wallis $p = 5.03 \times 10^{-68}$, Wilcoxon: Phasic $p = 1.11 \times 10^{-17}$, Oscillator $p = 5.37 \times 10^{-14}$, Tonic $p = 1.21 \times 10^{-24}$. **G.**

Absolute threshold, measured at the point where $dV/dt = 40\text{mV/s}$. Kruskal-Wallis $p = 1.38\text{e-}20$. Wilcoxon, Phasic $p = 3.04\text{e-}6$, Oscillator $p = 2.39\text{e-}9$, Tonic $p = 8.60\text{e-}4$. **H.** Resonance frequency, measured as the peak impedance from a 10 sec. chirp stimulus. Kruskal-Wallis $p = 3.49\text{e-}24$. Wilcoxon Phasic $p=4.84\text{e-}7$, Oscillator $p=4.07\text{e-}6$, Tonic $p =2.05\text{e-}9$.

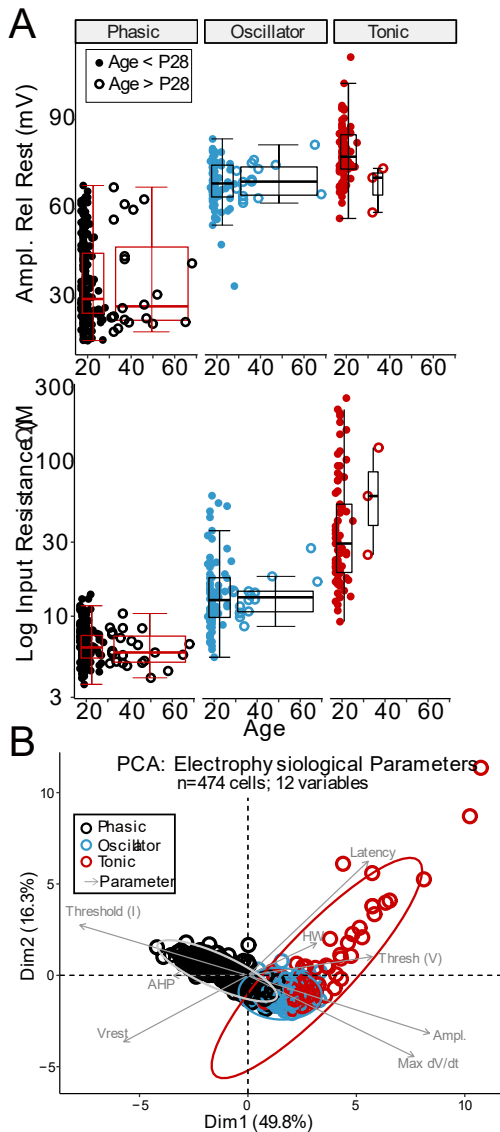


Figure 3.2. MSO principal neurons exhibit a continuum of electrophysiological properties that persists at older ages. A. AP amplitude and input resistance (R_{in}) in cells from animals between P28 and P68 (open circles) span a similar range of values than those from animals between P18 and P28 (closed circles). Data split according to cell firing type. Statistics were not performed due to uneven numbers of neurons in the age categories shown. **B.** PCA of electrophysiological parameters (n=474 cells; 12 features; recordings from all ages), from an imputed dataset (MICE). Highly impactful features are shown with grey arrows, with the length corresponding to vector strength in principal component analysis space.

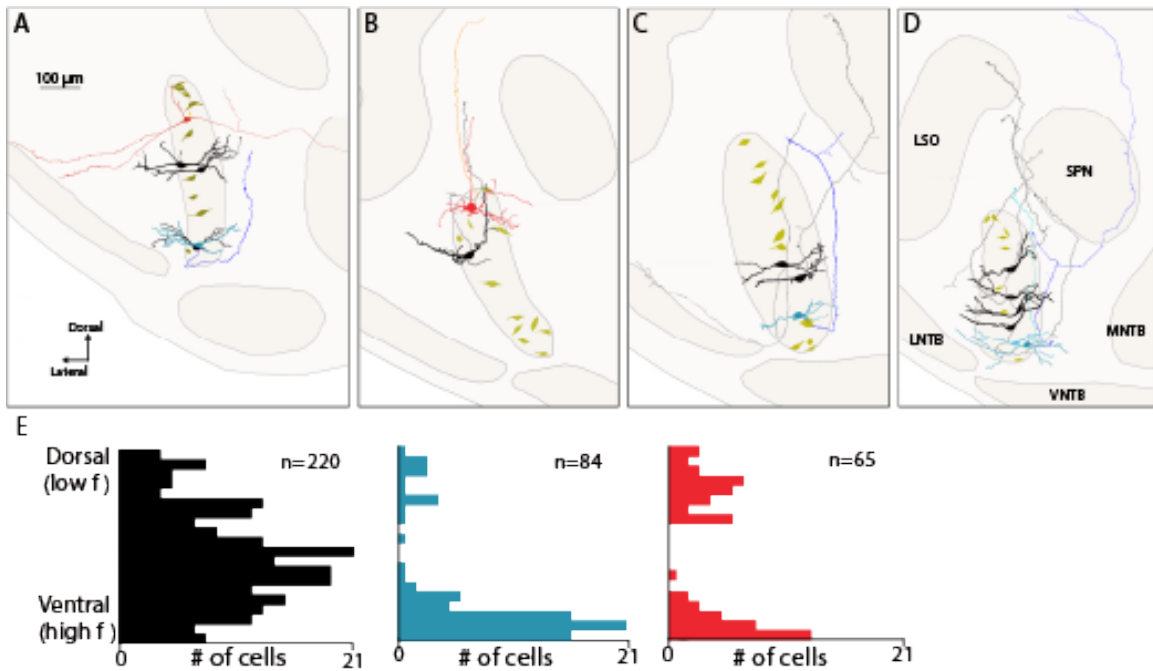


Figure 3.3. MSO neurons of all firing types send long-distance projections with similar trajectories. A-D. Phasic neurons: black, with axons in grey. Tonic neurons: red, with orange axons. Oscillators: blue, with dark blue axons. The two oscillator neurons and their axons in panel D are colored in different shades to better differentiate them. Dark yellow shapes are spindle-shaped cell bodies of unlabeled neurons to help delineate the boundaries of the MSO. Nuclei labeled in panel D apply to all panels. SPN: Superior periolivary nucleus, LSO: Lateral superior olive, MNTB: Medial nucleus of the trapezoid body, LNTB: Lateral nucleus of the trapezoid body, VNTB: Ventral nucleus of the trapezoid body. E. Distributions of recorded cells along the tonotopic axis of the MSO, normalized according to dorsal (low-frequency) and ventral (high-frequency) borders.

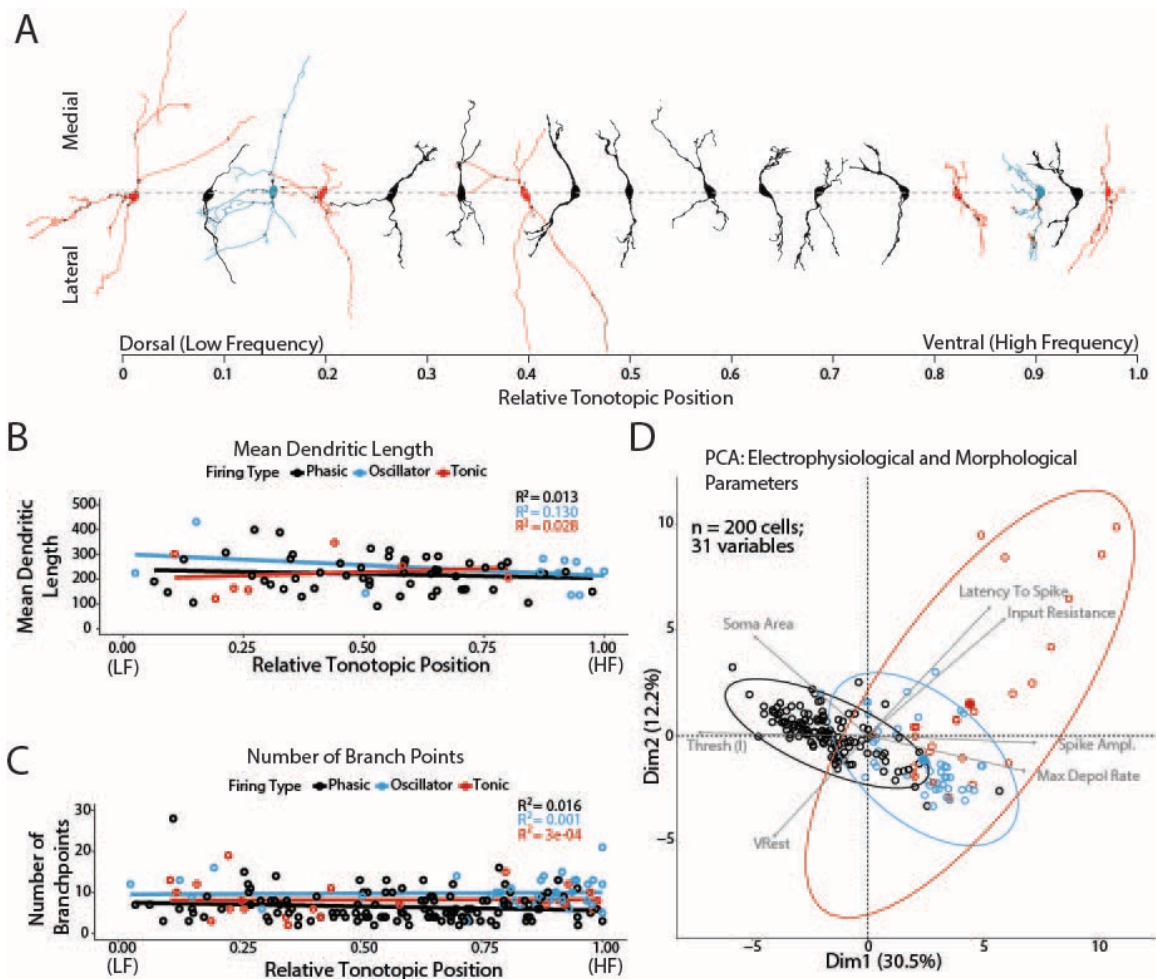


Figure 3.4. Morphological parameters do not separate MSO principal neurons by firing types. **A.** Example NeuroLucida reconstructions of filled, recorded MSO cells, positioned by their normalized dorsal (low-frequency) to ventral (high-frequency) location. Neurons are false-colored by recorded firing type. **B-C.** Reconstructed neurons were analyzed with Sholl analysis using NeuroLucida. There were no strong correlations with morphological parameters and tonotopic position within the nucleus for either mean dendritic length (B) or number of branch points (C). **D.** PCA of 200 cells that were electrophysiologically characterized and subsequently processed for morphological quantitation. A subset of 31 features (12 electrophysiology, 19 morphological) were used to perform the principal component analysis. Vectors show a curated selection from the 15 strongest contributing features, with corresponding directionality and strength. Centroids of the ellipses are displayed as enlarged, filled circles.

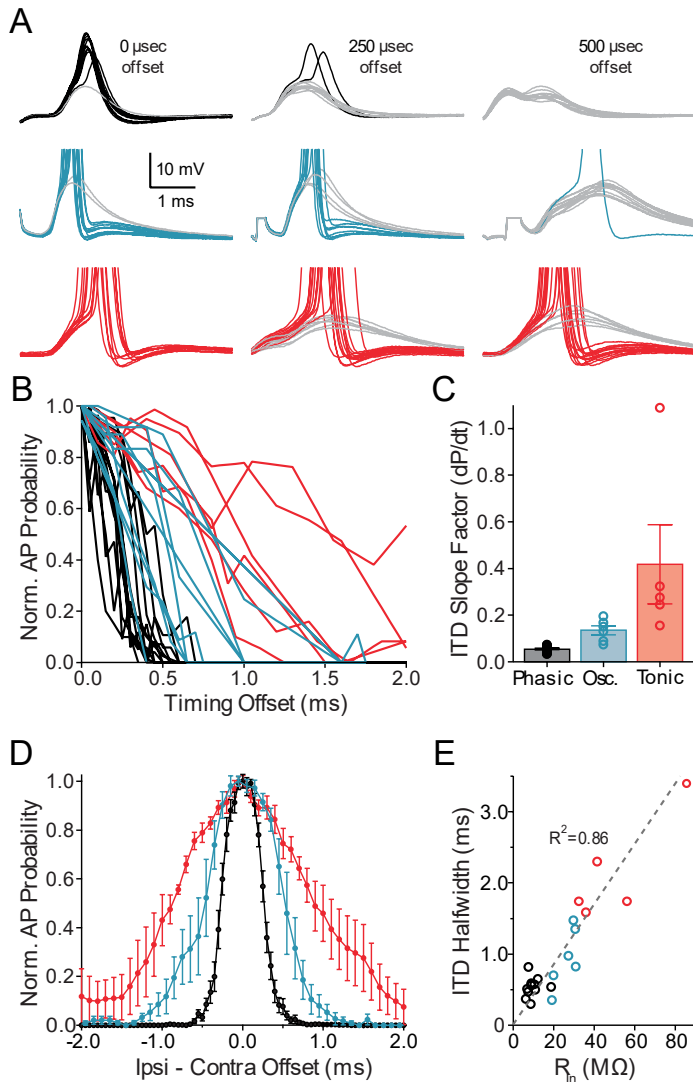


Figure 3.5. Diversity in temporal resolution across MSO neuron firing phenotypes. **A.** Responses to bilateral synaptic excitation at different temporal offsets in phasic, oscillator, and tonic firing phenotypes (black, blue, and red traces, respectively). For each firing type, subthreshold responses are shown in grey. APs in oscillator and tonic neurons are truncated. **B.** Spike probability vs timing offset. Only the right half of the ITD curve is shown for clarity. **C.** Slope of sigmoidal fits of each side of neurons' ITD curves. Each point represents an average of the right- and left-hand slope for each curve. Error bars represent \pm SEM. **D.** Averaged *in vitro* ITD tuning curves for each cell type. **E.** Correlation between the halfwidth of ITD curves and neuronal input resistance. Dashed line: linear fit to the data points [$y=0.045x+0.1$], with the R^2 value given in the figure (0.86).

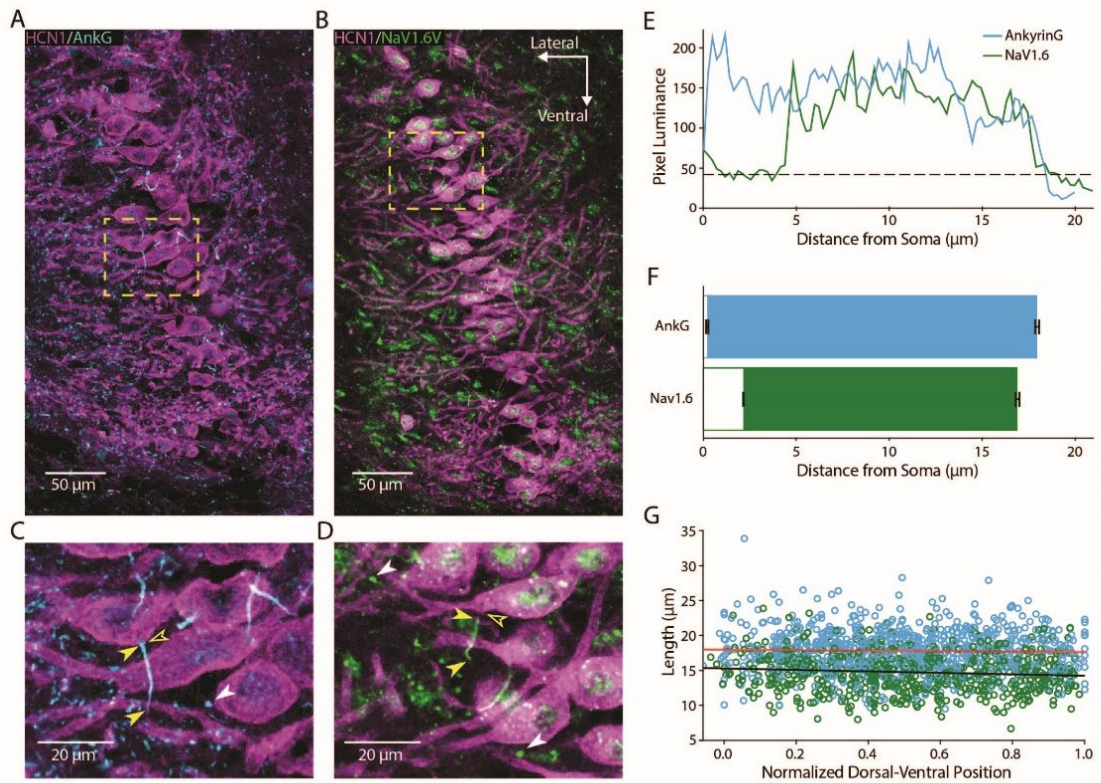


Figure 3.6. Axon initial segments of MSO neurons are consistent across the tonotopic axis. **A-B.** Immunostaining of coronal sections of the auditory brainstem containing the MSO for mouse anti-HCN1 (purple), and either rabbit anti-AnkyrinG (cyan) or rabbit anti-NaV1.6 (green). **C-D.** Expanded regions of interest in A and B bounded by dashed yellow boxes. Open arrowheads: presumed axonal point of emergence from the soma. Filled arrowheads: proximal and distal ends of example initial segments. White arrowheads: punctate labeling indicating presumed nodes of Ranvier. **E.** Intensity of fluorescent signal along the AIS for example neurons stained for AnkyrinG (cyan) and NaV1.6 (green). The end of the AIS is defined as the point where pixel luminance dropped below 20% of the maximal signal in the tracing (dashed line). **F.** Quantification of group data for the proximal and distal limits of the AIS (AnkyrinG signal) and NaV1.6 signal. **G.** Lengths of AnkyrinG and NaV1.6 labels as a function of the neuron soma's tonotopic position in the MSO (defined as in panel E). Solid lines are linear fits for the AnkyrinG (red line $y = -0.353x + 17.895$, $R^2 = 8.9e-4$, $p = 0.39$) and NaV1.6 data (black line $y = -1.0645x + 15.304$, $R^2 = 1.1e-2$, $p = 9.25e-3$). Data come from: AnkyrinG: 833 cells in 21 sections from 5 gerbils. NaV1.6: 648 cells from 18 slices from 3 gerbils. All error bars represent \pm SEM.

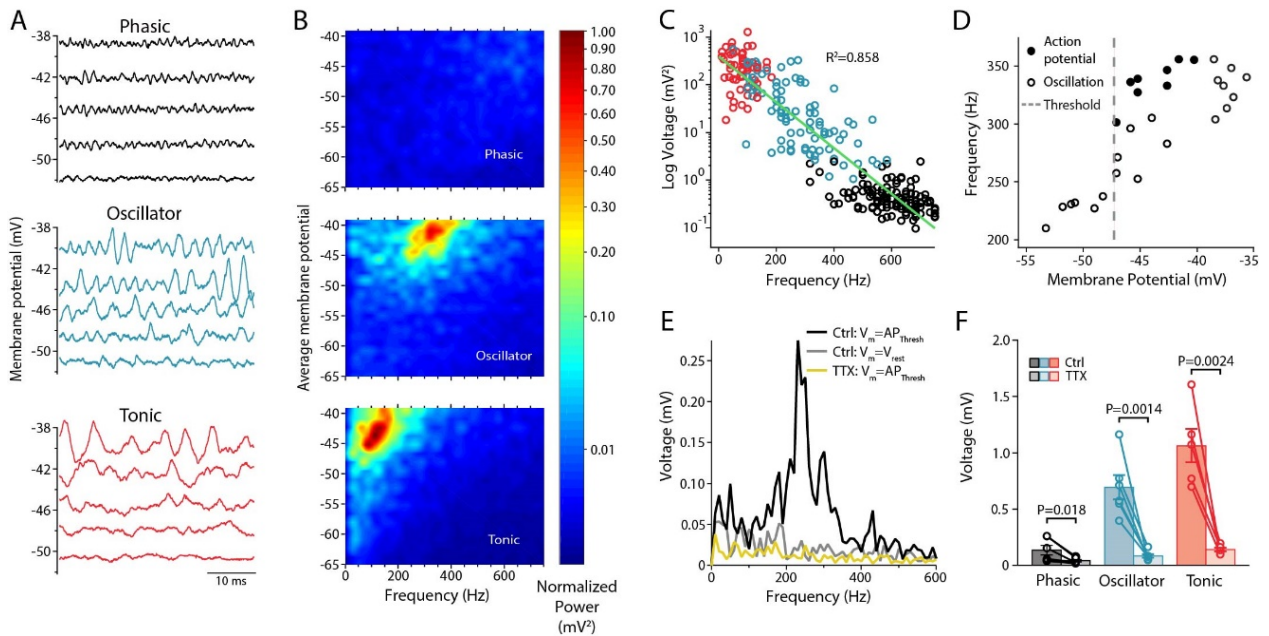


Figure 3.7. Oscillations are generated by the same mechanism in all firing types. A. Subthreshold membrane oscillations at different voltages during subthreshold responses to current steps in MSO firing types. **B.** Normalized voltage of oscillations in the frequency domain, derived from the fast Fourier transform (FFT) of traces (heatmap scale on right). Heatmaps taken from the same cells as shown in A. Scale is Voltage (mV^2) normalized by the peak measurement of the neuron with the largest oscillation (tonic neuron: $V(f) = 13.8 \text{ mV}^2$). **C.** Scatterplot showing the correlation between strongest frequency component of a neurons' oscillations, and the voltage signal at that frequency. Measurements were taken from voltages 2-5mV below spike threshold. Trendline shows the results of a linear fit to the squared voltage vs frequency relationship, $y = -0.49x \text{ mV}^2/\text{Hz} + 390.12 \text{ mV}^2$. **D.** Comparison of the frequency of subthreshold oscillations (open circles) and APs in the same cells (closed circles) as a function of membrane voltage. Dash line: Average AP threshold in MSO neurons. **E.** Example of the FFT output of a 100ms window from an oscillator neuron at -51mV before (black) and after TTX (yellow). AP threshold was -50.3mV in this cell. Also shown is the FFT from the voltage at rest (grey line). **F.** Summary graph of the effects of TTX on oscillations. Transformed voltage was summed from a 100Hz window centered around the peak frequency at a membrane potential close to threshold. P-values represent the results of paired, one tail t-tests. All error bars represent $\pm \text{SEM}$.

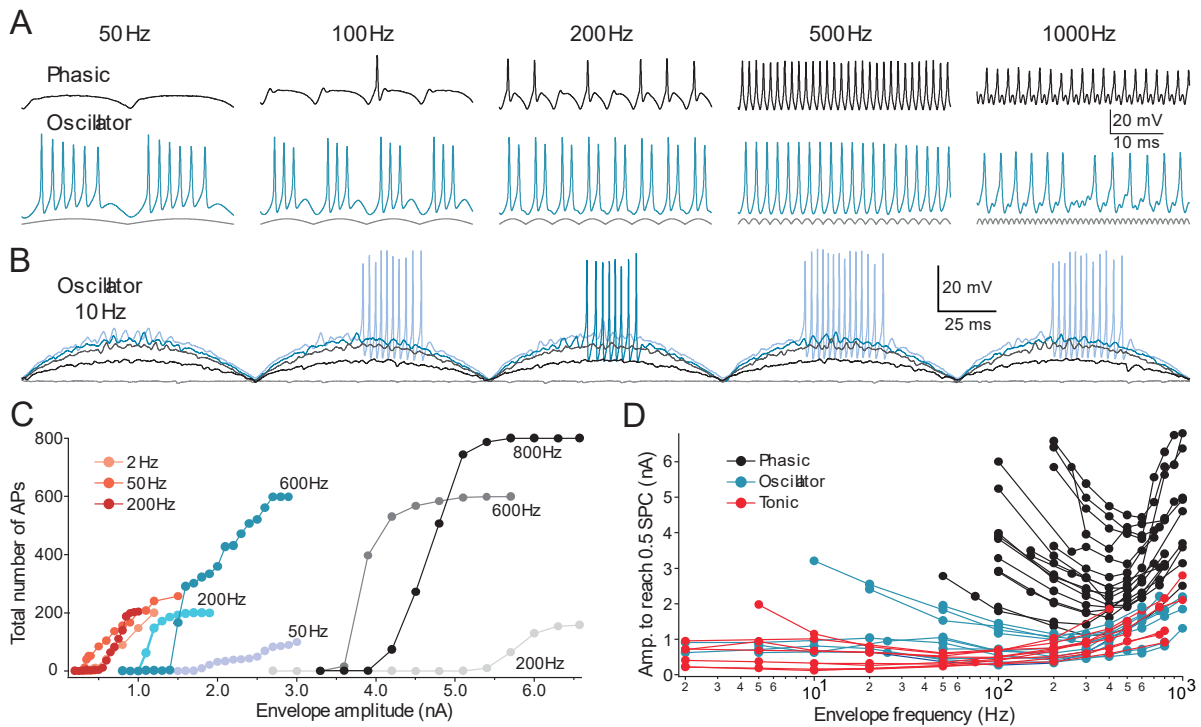


Figure 3.8. Envelope-like current injection reveals differential slope sensitivity of membrane voltage between cell types. **A.** Responses of a phasic (top) and oscillator (bottom) neuron to envelope-like (rectified sine wave) current injections at different frequencies. Injected current pattern is shown in grey at the bottom. Envelope current amplitudes: phasic neuron, 2600-3000pA; oscillator neuron, 900pA. **B.** Responses of an oscillator neuron to a 10 Hz envelope with peak current at 0, 500, 900, 1000, and 1100 pA. Note the increasing amplitude of subthreshold oscillations with increasing membrane voltage. **C.** Dynamic range of firing (total spikes over 1 second envelope current injection) plotted as function of envelope amplitude. Three frequencies from each firing type are shown in different colors: phasic neuron, grayscale; oscillator, blue; tonic, red. **D.** Envelope frequency vs the current amplitude needed to achieve an average of 0.5 spikes per cycle (SPC) at that frequency. Phasic neurons are band-limited in their responses across the range of envelope frequencies whereas oscillator and tonic neurons appear all-pass.

Chapter 4: Glycinergic axonal inhibition subserves acute spatial sensitivity to sudden increases in sound intensity

AUTHOR CONTRIBUTION TO THE WORK:

For the following manuscript, I provided specific contributions, but have provided the manuscript in whole with permission from the authors. Namely, my work consisted of performing the immunohistochemistry and super-resolution microscopy imaging found in **Figure 5** of this manuscript. Additionally, my direct contributions were in writing the results, figure legend, methods and general text surrounding this figure. I also provided editing and feedback for the manuscript as a whole throughout the submission, review, and resubmission phases.

Authors

Tom P. Franken^{1,2,*}, Brian J. Bondy³, David B. Haimes³, Joshua H. Goldwyn⁴, Nace L. Golding³, Philip H. Smith⁵, Philip X. Joris^{1,*}

¹Department of Neurosciences, KU Leuven, Leuven, B-3000, Belgium

²Systems Neurobiology Laboratory, The Salk Institute for Biological Studies, La Jolla, CA 92037, USA

³Department of Neuroscience, University of Texas at Austin, Austin, TX 78712, USA

⁴Department of Mathematics and Statistics, Swarthmore College, Swarthmore, PA 19081, USA

⁵Department of Neuroscience, University of Wisconsin-Madison, Madison, WI 53705, USA

*For correspondence: tfranken@salk.edu; philip.joris@kuleuven.be

ABSTRACT

Locomotion generates adventitious sounds which enable detection and localization of predators and prey. Such sounds contain brisk changes or transients in amplitude. We investigated the hypothesis that ill-understood temporal specializations in binaural circuits subserve lateralization of such sound transients, based on different time of arrival at the ears (interaural time differences, ITDs). We find that Lateral Superior Olive (LSO) neurons show exquisite ITD-sensitivity, reflecting extreme precision and reliability of excitatory and inhibitory postsynaptic potentials, in contrast to Medial Superior Olive neurons, traditionally viewed as the ultimate ITD-detectors. *In vivo*, inhibition blocks LSO excitation over an extremely short window, which, *in vitro*, required synaptically-evoked inhibition. Light and electron microscopy revealed inhibitory synapses on the axon initial segment as the structural basis of this observation. These results reveal a neural vetoing mechanism with extreme temporal and spatial precision and establish the LSO as the primary nucleus for binaural processing of sound transients.

INTRODUCTION

A key component of the neuron doctrine is the unidirectional propagation of action potentials, formulated as the “law of dynamic polarization” by Cajal and van Gehuchten (Berlucchi, 1999; Shepherd, 1991). As the site where action potentials are typically initiated, the axon initial segment (AIS) has a pivotal role in this process (Bender and Trussell, 2012; Kole and Brette, 2018; Letierrier, 2018) and is a bottleneck where inhibition can have an “outsized” effect on a neuron’s output, as proposed for chandelier and basket cells (Blot and Barbour, 2014; Nathanson et al., 2019). Disruption of such synapses is associated with severe brain disorders (Wang et al., 2016), but their exact functional role in the normal brain is speculative because physiological studies of these synapses have been limited to *in vitro* recordings. Even the basic physiological properties of axo-axonic synapses are unclear, not in the least in cortex, where it has recently even been debated whether these synapses are excitatory or inhibitory (Woodruff et al., 2010). Here we report

AIS inhibition by glycinergic neurons for the first time, with a specific functional role tying together several puzzling anatomical and physiological features.

Humans are exquisitely sensitive to the spatial cues of time and intensity differences between sounds at the two ears (ITDs and IIDs; Klumpp and Eady, 1956; Yost and Dye, 1988). The classic “duplex” account posits that these two cues operate in different frequency regions: spatial localization is subserved by ITDs for low-frequency and by IIDs for high-frequency sounds (Strutt, 1907). This account dovetails with the existence of two brainstem circuits seemingly dedicated to the extraction of these cues: the MSO generates sensitivity to ITDs (Goldberg and Brown, 1969; Yin and Chan, 1990) and the LSO to IIDs (reviewed by Tollin, 2003). These two circuits share many components: their most salient difference is that MSO neurons perform coincidence detection on the excitatory spike trains they receive from both ears, while LSO neurons perform a differencing operation comparing net excitatory input from the ipsilateral vs. net inhibitory input from the contralateral ear.

This classical duplex account of the respective role of these two binaural nuclei does not square with striking physiological and morphological features found in the circuits converging on the LSO, including some of the largest synapses in the brain (e.g. the calyx of Held). This and other observations suggest that the LSO is not simply weighing excitation vs. inhibition towards IID-sensitivity, but is specialized for temporal comparisons between the two ears. Many studies indeed observed ITD-sensitivity of LSO neurons to a range of sounds (tones, amplitude-modulated tones, noise (Caird and Klinke, 1983; Irvine et al., 2001; Joris, 1996; Joris and Yin, 1995; Tollin and Yin, 2005)), but ITD-sensitivity to these sounds was weak compared to the effects of IIDs and not commensurate with the striking specializations of the LSO circuit (Joris and Yin, 1998). The only stimuli to which strong ITD-sensitivity was occasionally observed in LSO neurons was to electrical shocks *in vitro* (Sanes, 1990; Wu and Kelly, 1992) and, *in vivo*, to brisk changes in sound characteristics, usually referred to as “transients”. Examples of such transients are clicks, tone onsets, and fast frequency modulated sweeps (Caird and Klinke, 1983; Irvine et al., 2001; Joris and Yin, 1995; Park et al., 1996). High-frequency transients are generated

as adventitious sounds created by the locomotion of predators or prey at close range (Clark, 2016; Goerlitz and Siemers, 2007). Behavioral experiments show that lemurs rely on such sounds to forage (Siemers et al., 2007), and mice choose routes to minimize the generation of such sounds (Roche et al., 1999). This leads to the hypothesis that detection and lateralization of these sounds was a strong evolutionary pressure for this high-frequency circuit and drove its striking temporal specializations (Joris and Trussell, 2018). The recent discovery that LSO principal cells have fast membrane properties and respond transiently to tones (Franken et al., 2018) gives extra weight to the importance of timing in this circuit.

We used *in vivo* and *in vitro* whole-cell patch clamp methods to examine ITD-sensitivity in identified LSO and MSO neurons in response to transient sounds, and found exquisite tuning in LSO but not MSO neurons. LSO principal cells showed a sub-millisecond window where the contralateral ear effectively vetoes the output of the ipsilateral ear, and this is dependent on the strategic positioning of inhibitory inputs on the AIS. Moreover, effects of IIDs are such that they enhance ITD-sensitivity. Thus, for sound impulses, fast temporal differentiation is implemented in LSO, and this is a more suitable neural operation for the creation of binaural sensitivity than the coincidence-type operation in MSO. Our finding that inhibition at the AIS combines with other specializations to achieve temporal differentiation that is punctate in space and time, pulls together previously puzzling anatomical and physiological features into a single coherent view that proposes a new role for LSO principal neurons.

RESULTS

Sharp ITD-sensitivity to clicks in LSO but not MSO

We obtained *in vivo* whole-cell recordings while presenting clicks at different ITDs in 19 LSO neurons and 11 MSO neurons. Responses to tones for these cells have been reported before (Franken et al., 2018, 2015). We were surprised to find sharp sensitivity to ITDs of clicks in LSO but not MSO neurons. **Figure 4.1A** shows sensitivity to ITDs of transients in a principal LSO neuron (IID function in **Figure 4.1**-figure supplement 1A).

Identical impulsive sounds (“clicks”) were delivered to the two ears with varying ITD. The neuron reliably fires a single spike at large negative and positive ITDs, but is completely inhibited over a sub-millisecond range near 0 μ s. The resulting U-shaped tuning function has extraordinarily steep slopes (-6.5 and 4.2 spikes per click/ms); a narrow and deep trough (450 μ s halfwidth) with complete suppression of spiking, and low variability. A measure of tuning, ITD-SNR (the ITD-dependent variance in spike rate divided by the total variance (Hancock et al., 2010)) gives a value of 0.86. Figure 4.1B shows a waterfall plot of the corresponding intracellular voltage signals. It shows an orderly progression of leading EPSP and lagging IPSP at negative ITDs and the reverse sequence at positive ITDs, with a narrow range where the PSPs effectively oppose each other and spiking is abolished. The traces are aligned to the ipsilateral (excitatory ear) click at 0 ms (see left panel): events locked to that stimulus appear vertically stacked. As ITD changes, events locked to the contralateral ear are stacked diagonally. Clearly, the reliable response of 1 spike/click (Figure 4.1A) is in response to the ipsilateral ear. At large negative click ITDs, when the ipsilateral (excitatory) ear is leading, excitation is unopposed and reliably triggers a single spike. Likewise, at large positive ITDs, the leading contralateral (inhibitory ear) click is not able to suppress spiking to the lagging ipsilateral click, even for lags between IPSP and EPSP as small as 0.25 ms. Figures 4.1C and 4.1D show data for a non-principal LSO neuron (IID function in Figure 1-figure supplement 1B): here the intracellular traces are more complex than a stimulus-like stacking of PSPs, but nevertheless tuning to ITDs is present, be it with shallower slopes (-1.0 and 2.0 spikes per click/ms), wider trough (halfwidth 1350 μ s), and higher variability, yielding an ITD-SNR of 0.63. Figures 4.1E and 1F show data for an MSO neuron. As expected, the main feature in the response is an excitatory peak near 0 ms. Even though this is one of the steepest-sloped ITD-functions of our MSO sample (2.1 spikes per click/ms for slope at ITD < 0ms), the ITD-tuning lacks the acuity observed in principal LSO cells, with an ITD-SNR of only 0.38. The intracellular data (Figure 4.1F) reveal that, surprisingly, spiking is not restricted to ITDs where the two events coincide, but also occurs at other ITDs, where the click at either ear can elicit a suprathreshold response.

Population data are shown in Figures 4.1G-I and Figure 1-figure supplement 2. LSO neurons were sorted into principal and non-principal neurons based on anatomical and physiological criteria (Franken et al., 2018). In principal cells (Figure 4.1G), the spiking output of most cells is steeply dependent on ITD at some ITD range. Non-principal LSO neuron tuning (Figure 4.1H) is much more varied but occasionally also features steep slopes. These spike data elaborate on a handful of extracellular recordings of such sensitivity in LSO (Caird and Klinke, 1983; Irvine et al., 2001; Joris and Yin, 1995) and show that this acute temporal sensitivity is a dominant feature of principal LSO neurons, the most frequent cell type in this nucleus, which is undersampled with extracellular methods (Franken et al., 2018). We observed steeper slopes and narrower functions at higher sound levels (Figure 1-figure supplement 4.3A,B).

Compared to LSO, ITD-tuning was surprisingly weak in the majority of MSO neurons (Figure 4.1I). While ITD-functions of LSO neurons had steep slopes, such slopes could not be meaningfully calculated in many MSO neurons (Figure 4.1J). Halfwidths of the ITD-tuning functions, i.e. the ITD range over which the response is suppressed by $\geq 50\%$ (for LSO), or enhanced by $\geq 50\%$ (for MSO), are smaller for principal LSO cells than for MSO cells (Figure 1K; respective median (IQR) 0.84 (0.48), 8 cells, and 1.40 (0.74), 6 cells; Mann-Whitney $U = 40.0$, $p = 0.043$; $\theta = 0.83$ (95% CI [0.52, 0.95])). Halfwidth is smaller for higher CF ($r = -0.62$, $p = 0.001$), potentially due to the non-uniform distribution of glycine receptors with higher concentrations in the high frequency region (Sanes et al., 1987) and wider bandwidth at high CFs. Halfwidth does not fully capture the difference in tuning quality that can be observed when comparing Figures 4.1A,1G with 1E,1I: tuning functions are noisier for MSO neurons than for principal LSO neurons. To capture the reliability of tuning better, we calculated ITD-SNR (Methods). ITD-SNR was substantially higher for principal LSO cells than for MSO cells, across the range of frequency tuning (Figure 1L; respective median (IQR) 0.62 (0.17), 7 cells, and 0.15 (0.10), 7 cells); Mann-Whitney $U = 49.0$, $p = 0.0006$; $\theta = 1$ (95% CI [0.73, 1])); there was no significant difference in CF for the principal LSO and MSO neurons included in this analysis (Mann-Whitney $U = 31.0$, $p = 0.46$). We also find a significantly higher ITD-SNR for principal LSO cells

than for non-principal LSO cells (non-principal LSO: median (IQR) 0.33 (0.31), 9 cells; Mann-Whitney $U = 54.0$, $p = 0.016$; $\theta = 0.86$ (95% CI [0.57, 0.96])). This is not explained by differences in sound level (Figure 1-figure supplement 3C,D).

Thus, despite the classical role of MSO neurons as “ITD detectors”, principal LSO neurons show superior ITD-tuning for transient sounds. We also tested LSO neurons with broadband noise, which has a flat amplitude spectrum like clicks but with a random phase spectrum. ITD-sensitivity to noise was generally weak (Figure 4.1-figure supplement 4A), which was also the case for responses to dynamic interaural phase differences in modulated or unmodulated pure tones (Figure 4.1-figure supplement 4B). However, the presence of brisk transients in sustained sounds, e.g. at tone onset (Figure 4.1-figure supplement 4C) could lead to sharp ITD-sensitivity, as was also the case for a succession of transients, simulating rustling sounds (Ewert et al., 2012; Figure 4.1-figure supplement 5). Thus, a broad stimulus spectrum does not suffice, and a brief duration followed by silence is not required for the generation of sharp ITD-sensitivity: the necessary and sufficient condition is to have fast and large changes in stimulus amplitude. Inspection of the membrane potential traces revealed why transients are more effective than sustained sounds: EPSPs evoked by transients are steeper than those evoked by ongoing sounds, with lower action potential voltage thresholds, and IPSPs are often steeper as well (Figure 4.1-figure supplement 4D,E).

Effective inhibition of LSO neurons is limited to a short initial part of the IPSP

Prior to our recordings, published LSO *in vivo* intracellular recordings were limited to a few traces (Finlayson and Caspary, 1989). To gain insight into the sharp ITD-tuning in LSO and its lack in MSO, we compared intracellular synaptic responses to monaural and binaural clicks from these neurons (Figures 4.2 and 4.3). As illustrated for two LSO neurons (Figures 4.2A and 4.2B), they receive a well-timed EPSP in response to monaural ipsilateral clicks, which reliably trigger spikes, and a well-timed IPSP in response to monaural contralateral clicks. There have been many indirect estimates of the effective latency of excitation and inhibition in LSO neurons using *in vivo* extracellular recording,

suggesting a close match between the onset of EPSPs and IPSPs, despite the longer pathway and extra synapse for contralateral inhibition. For example, tuning curves centered at negative ITDs (Figures 4.1A and 4.2D) suggest that contralateral inhibition effectively has a shorter latency (by a few hundred microseconds) than ipsilateral excitation, while the opposite is the case when centered at positive ITDs (Figures 4.1C and 4.8L). Our intracellular records allow direct measurement and show that indeed the latencies are closely matched, for both principal and non-principal neurons, with the IPSP sometimes arriving first (Figure 4.2C). In 8 principal neurons, we observed a small positive deflection preceding the IPSP by ~ 0.5 ms (arrowhead and insert Figure 4.2A, see also Figure 4.2F and Figure 2-figure supplement 1C), suggesting that consistent, precise response timing is already present at the presynaptic level.

Strikingly, the IPSP duration extends to almost 5 ms in principal cells (Figure 4.2A), close to an order of magnitude larger than the halfwidth of the tuning function to ITDs (Figure 4.1A and 2D). This is consistent with *in vitro* data (Sanes, 1990; Wu and Kelly, 1992), where the effective window of inhibition was also reported to be much smaller than the IPSP duration. The availability of the monaural responses allows us to examine this window. Figure 4.2E shows comparisons of binaural and monaural click responses, for a principal LSO neuron (ITD-function in Figure 4.2D). In each panel, the intracellular response is shown at one ITD (black traces), with the monaurally-recorded responses to ipsi- (blue) and contralateral clicks (green) superimposed, incorporating the stimulus ITD. At large negative delays (Figures 4.2E1 and 2E2), the leading EPSP reliably triggers spiking, unhindered by the ensuing IPSP. More surprisingly, when the IPSP leads and significantly overlaps with the EPSP (Figure 4.2E6), it also fails to inhibit spiking. Only when the early steep slope of the IPSP coincides with the early steep slope of the EPSP are spikes completely blocked (Figure 4.2E4). Comparison of binaural responses for a fuller range of ITDs with the monaural IPSP, is shown in Figure 2F. Responses from large negative to large positive ITDs reveal the exceedingly narrow range of ITDs over which spikes are suppressed, near the onset of the IPSP. Figure 2-figure supplement 1 shows another example.

Weak tuning in MSO neurons results from a breakdown of coincidence detection for transients

Ideal coincidence detectors are akin to multipliers: they only generate an output spike when receiving a spike from each input. MSO neurons approach archetypal coincidence detectors (Joris and van der Heijden, 2019) and respond poorly to monaural stimulation and to temporally misaligned inputs (Goldberg and Brown, 1969; Yin and Chan, 1990). This largely failed in response to clicks, because of a surprising efficacy of monaural stimuli. Figures 3A and 3B show responses to monaural ipsilateral (top panels) or contralateral (bottom panels) clicks for two MSO neurons. Depolarizing events dominate and often generate spikes. Examples of spike rates as a function of click intensity (Figures 4.3C and 3D), illustrate that monaural spike rates to clicks were substantial and could even equal spike rates to binaural clicks (here delivered at ITD = 0 ms, generating a spike rate >90% of the peak of the click ITD function). We calculated the summation ratio (Goldberg and Brown, 1969), i.e. the ratio of the spike rate to binaural stimulation to the sum of monaural responses, where values > 1 indicate facilitation, as expected for a coincidence detector. MSO summation ratios in response to clicks (Figure 4.3F, magenta) were all < 1.3 and had a median of 0.97, indicating that the binaural response rates are similar to the sum of monaural response rates. In contrast, MSO summation ratios to tones were substantially higher than those to clicks (Figure 3F, black; respective median (IQR) 7.56 (11.41), 23 cells and 0.97 (0.38), 5 cells; Mann-Whitney $U = 4.0$, $p = 0.001$; $\theta = 0.03$ (95% CI [0.004, 0.29])). This convincingly shows that the binaural advantage that MSO neurons display for tones is largely non-existent for clicks.

LSO neurons can be regarded as “anti-coincidence” detectors, where the binaural rate can drop to 0 spikes and the response to monaural ipsilateral stimulation saturates near 1 spike/click (double events were sometimes observed, Figure 4.3-figure supplement 1). Contralateral stimulation does not generate spiking except sometimes at high stimulus intensities, presumably due to acoustic crosstalk (Figure 4.3E). To calculate the LSO neuron summation ratio, we invert the ratio (sum of monaural response rates / binaural

response rate): a lack of binaural effect again results in a summation ratio of one, and binaural interaction results in larger ratios. LSO responses all resulted in summation ratios well above two (Figure 3F, green), substantially higher than for MSO responses to clicks (respectively 7 cells and 5 cells, Mann-Whitney $U = 0$, $p = 0.003$; $\theta = 0$ (95% CI [0, 0.32])). Binaural summation to clicks for LSO cells thus clearly surpasses that of MSO cells.

***In vitro* recordings reveal powerful inhibition for synaptically-evoked but not for simulated IPSPs**

To better understand the narrow, sub-millisecond (Figures 4.1A, 1K and 2D) window of inhibition in LSO neurons, we performed *in vitro* experiments in P19-22 gerbils. Shocks to LSO afferents evoke well-timed, transient inhibition and/or excitation and are a particularly apt analogue of acoustic clicks. Thus, comparison of *in vitro* and *in vivo* data is unusually straightforward because the afferent signals evoked by shock and clicks are similar to a degree that is only rarely achieved in this type of comparison. Indeed, early experiments shocking inputs on both sides (Sanes, 1990; Wu and Kelly, 1992), and recent experiments using optogenetic stimulation (Gjoni et al., 2018b), showed clear ITD-sensitivity very similar to *in vivo* responses. Figure 4.4A shows recordings from an LSO neuron where ipsilateral excitation was triggered synaptically by electrical shocks, inhibition was simulated by injecting simulated conductances, and their relative timing was varied to mimic ITDs. Surprisingly, this protocol did not result in a profound inhibitory trough in the tuning function *in vitro* (Figure 4.4C). Results for seven other neurons are shown in Figure 4-figure supplement 1D (solid lines): although U- or V-shaped tuning functions were obtained, full inhibition (spike rate of 0 spikes/s) was not reached in most cases. ITD tuning expressed as ITD-SNR is less pronounced for these *in vitro* functions than for *in vivo* functions (respective median (IQR) 0.40 (0.18), 8 neurons and 0.62 (0.17), 7 neurons; Mann-Whitney $U = 51.0$, $p = 0.006$; $\theta = 0.91$ (95% CI [0.62, 0.98])). Thus, inhibition simulated by somatic injection of conductances cannot reproduce the profound inhibition observed with comparable levels of hyperpolarization *in vivo*. In dynamic clamp experiments, the conductances must be delivered to a single somatic location, in contrast

to the more distributed spatial distribution of real inhibitory synapses that could be distributed along the axon hillock, soma and proximal dendrites. To test whether the efficacy of inhibition is sensitive to the spatial location of inhibition, we reversed the stimulus protocol: we generated natural, spatially distributed synaptic inhibition by delivering shocks to contralateral inputs, while excitation was simulated by conductance clamp at the soma. Under these conditions, despite the similar range of hyperpolarization apparent at the soma, profound inhibition of spiking was reached in the neuron in Figure 4.4B and in all neurons. The tuning functions were very similar to the ITD functions observed *in vivo* (Figure 4.4D; Figure 4-figure supplement 1E (solid lines); compare with Figures 4.1A, 1G and 2D), in terms of slope as well as ITD-SNR (Figure 4.4E, blue). The difference in ITD-SNR between simulated inhibition and simulated excitation was statistically significant (respective median (IQR) 0.40 (0.18), 8 neurons and 0.72 (0.18), 7 neurons; Mann-Whitney $U = 54.0$, $p = 0.001$; $\theta = 0.96$ (95% CI [0.69, 1])). The same findings were obtained when electrical currents instead of conductances were injected to simulate synaptic input (Figure 4-figure supplement 1 (dashed lines)). Together, these results suggest that at least some inhibitory synapses are located electrically closer to the spike initiation region in the axon, prompting a detailed examination of the spatial pattern of inhibitory synapses at the soma, axon hillock and the AIS.

LSO, but not MSO, neurons have inhibitory innervation of the axon initial segment

The connectivity of LSO neurons has been extensively studied (Cant, 1991; Glendenning et al., 1985; Yin et al., 2019). Although there are remaining questions particularly regarding the identity of input from the cochlear nucleus (Doucet and Ryugo, 2003; Gómez-Álvarez and Saldaña, 2016), the inhibitory input provided by the homolateral medial nucleus of the trapezoid body (MNTB) is well-characterized (Banks and Smith, 1992; Gjoni et al., 2018a; Kapfer et al., 2002; Smith et al., 1998). The inhibitory projection targets LSO somata (Gjoni et al., 2018a; Smith et al., 1998), so it is surprising that somatic injection of IPSPs or IPSCs does not fully mimic synaptic stimulation. That the actual inhibitory synaptic input is more powerful than somatic current injection suggests a

specialization distal from the soma, possibly the AIS. To visualize the spatial pattern of glycinergic terminals on LSO neurons, we immunostained the LSO for gephyrin and ankyrin G, markers for postsynaptic glycine receptors and the scaffolding of the AIS/nodes of Ranvier, respectively (Figure 4.5). We additionally stained for DAPI or for synaptophysin-1 (SYN1) to visualize somata or synaptic boutons, respectively. We analyzed samples from the mid-frequency region of the LSO (Figures 4.5A and 5B), where electrophysiological recordings were typically made, selecting neurons with a complete, relatively planar AIS that could be unambiguously connected to an axon hillock and soma (Figures 5C-H). A high density of gephyrin-positive puncta covered the soma and proximal dendrites. In several cases, gephyrin-positive puncta could also be seen extending onto the axon hillock (Figure 4.5, filled yellow arrowheads), and/or along the AIS itself (Figure 4.5, open yellow arrowheads). Clear overlap of gephyrin-positive puncta with a putative synaptic terminal labeled by synaptophysin-1 on an uninterrupted AIS was sometimes seen (Figure 4.5F, open white arrowhead).

To obtain conclusive proof of innervation of the AIS, we performed electron microscopy (EM) on three principal LSO neurons labeled with biocytin. Figure 4.6A shows a camera lucida drawing of a principal LSO neuron, with indication of parts of the axon that were examined with EM. A section at a distance of several tens of μm from the soma, shows the myelinated axon (Figure 4.6B). A section through the AIS shows indeed three synaptic profiles (Figure 4.6C, enlarged in Figure 4.6D1-3). The same was true for the two additional principal LSO neurons (Figure 4.6-figure supplement 1A). In contrast, principal MSO neurons ($n = 2$) did not show such innervation (Figure 4.6-figure supplement 1B).

Computational model shows that inhibitory synapses have a larger effect when added to the axon initial segment instead of to the soma

To test the hypothesis that adding inhibitory synapses to the AIS results in more powerful inhibition compared to only somatic inhibition, we constructed an LSO neuron model. In brief, we adapted the approach of (Goldwyn et al., 2019) to describe soma and axon regions of an LSO neuron. Soma-axon coupling was defined by coupling constants

(voltage attenuation factors) and additional parameters were informed by previous models of LSO neurons (Ashida et al., 2017; Gjoni et al., 2018; Wang and Colburn, 2012), typical response characteristics such as membrane time constant and input resistance (Sanes, 1990), and features of our *in vivo* recordings (such as amplitude and variability of inhibitory post-synaptic potentials). See Methods and Figure 4.7-figure supplement 1 for further details.

We created ITD tuning curves by computing spike probability as we varied the time lag between excitatory and inhibitory inputs (positive ITD if inhibition leads, see voltage traces in Figure 4.7B). We selected parameter values so that the model exhibited modest ITD tuning when all eight inhibitory synapses contacted the soma (minimum spike probability of approximately 0.5 for the dashed line in Figure 7A). This outcome matched the relatively shallow ITD tuning curves measured *in vitro* when IPSPs were delivered through dynamic clamp or current injection (Figure 4.4, Figure 4-figure supplement 1). The ITD tuning curve became substantially deeper when we relocated two of the inhibitory synapses and placed them on the AIS (solid line in Figure 4.7A). This reflects the combined effect of soma and AIS-targeting inhibition: the AIS inhibition alone was not sufficient (compare solid and dotted line in Figure 4.7A). These computational results thus provide support for our hypothesis that a combination of inhibition at the soma and the AIS is more powerful than inhibition restricted to the soma, and can result in steep ITD functions in LSO neurons.

To understand why inhibitory synapses on the AIS have a larger effect than the same number of synapses on the soma, we can compare how these two inhibition sources impact voltage in the AIS region. Consider a simplified scenario of steady-state responses to constant current inputs (the same argument can be modified for dynamic inputs using frequency-dependent impedance functions). In this case, soma-targeting inputs affect soma voltage in proportion to soma input resistance R_1 and this voltage spreads to the AIS in proportion to $\kappa_{1 \rightarrow 2}$ (see discussion of coupling constants in Methods, and also Goldwyn et al. (2019)). The impact of soma-targeting inhibitory input on AIS voltage is, therefore, proportional to $R_1 \kappa_{1 \rightarrow 2}$ (equivalent to the transfer resistance from soma to AIS (Koch et

al. 1982)). In contrast, inhibitory inputs on the AIS change AIS voltage in proportion to AIS input resistance R_2 . Thus, we expect AIS-targeting inhibition to be more powerful than soma-targeting inhibition if $R_2 > R_1 \kappa_{1 \rightarrow 2}$. This condition is always satisfied because $R_2 \kappa_{2 \rightarrow 1} = R_1 \kappa_{1 \rightarrow 2}$ since both terms are expressions for the transfer resistance (discussed in Methods) and $\kappa_{2 \rightarrow 1} < 1$ under the plausible constraint that voltage must attenuate somewhat from AIS to soma. For the simulations in Figure 4.7A,B, for instance, we used $\kappa_{1 \rightarrow 2} = 0.95$, $\kappa_{2 \rightarrow 1} = 0.6$, $R_1 = 40 \text{ M}\Omega$ and $R_2 = 64 \text{ M}\Omega$. We found qualitatively similar results using a range of backward coupling constants (Figure 4.7C) and found that ITD-tuning depth is relatively insensitive to changes in forward coupling (results not shown).

To test whether our findings are robust for waveform kinetics different than those used in the dynamic clamp experiments, we performed the same analyses using conductance waveforms adapted from a recent study of mature LSO neurons (Beiderbeck et al., 2018, Methods). The findings are qualitatively similar, with narrower tuning functions due to faster IPSPs (Figure 4.7-figure supplement 2).

LSO neurons show graded latency-intensity changes which disambiguate spatial tuning

It has been hypothesized that temporal specializations in the LSO-circuit evolved to generate tuning to ITDs of transient sounds congruent with IID-tuning (Joris and Trussell, 2018). Classical tuning to IIDs is sigmoidal (Figure 4.1-figure supplement 1A and Figure 1-figure supplement 1B), with higher spike output for IIDs < 0 and complete inhibition of spiking for IIDs > 0 , so that LSO neurons are excited by sounds in the ipsilateral hemifield (Tollin and Yin, 2002) (Figure 4.8A, cartoons below the abscissa illustrate the accompanying PSP changes). Congruence of ITD- and IID-tuning would be obtained if the “left” slope of ITD-functions is centered over the ITD-range relevant to the animal (Figure 4.8B, function 3): an increase in firing rate would then consistently signal a sound source more towards the ipsilateral side, for both cues. Our sample (Figure 4.1 Figure 1-figure supplement 2), as well as published ITD-functions (Beiderbeck et al., 2018; Irvine et al., 2001; Joris and Yin, 1995; Park et al., 1996), do not support such congruency as a

dominant feature: indeed for at least a sizable fraction of neurons, it is the “right” slope that is closest to 0 ms (Figure 8B, function 1). For cases where the ITD-function is centered near 0 ms (Figure 4.8B, function 2, example in Figure 4.8L (cyan)), there is an additional issue of ambiguity: a rise in spike rate could signal both a leftward or rightward change in horizontal position of the sound source. A similar problem occurs at the population level if some neurons have the “left” slope near 0 and others the “right” slope. However, a natural and elegant solution to these issues is directly embedded in the properties of the LSO circuit.

Figures 4.8D and 4.8E show how PSPs change with sound intensity for a principal and a non-principal cell. In the principal neuron, the changes in both EPSP and IPSP are extremely reproducible and finely graded in amplitude and latency with increasing SPL, also for individual trials (Figure 4.8-figure supplement 1A). In the non-principal neuron, the changes are complex, with multiple events following each click and a leading IPSP at high intensities. The latency changes are sizeable compared to the relevant ITD range for the animal: they show a steady decrease which is approximately linear over the 30-dB range tested, with a slope amounting to $\sim 10\text{-}20 \mu\text{s}/\text{dB}$ (Figure 4.8F: $13 \mu\text{s}/\text{dB}$ ipsi and $20 \mu\text{s}/\text{dB}$ contra; 8G: $10 \mu\text{s}/\text{dB}$ ipsi and contra).

In real-world environments, IIDs and ITDs co-occur and are correlated (Gaik, 1993). For transient stimuli, the two cues merge into a single EPSP – IPSP pair with a given amplitude and time difference. Figures 4.8H-8J use monaural responses to characterize such pairs for variations of single or combined cues. For changes in ITD only (IID fixed at 0 dB), 3 pairings are shown (Figure 4.8I). The spike rates obtained for these conditions are indicated in Figure 4.8L (cyan): varying ITD over a large range results in the rather symmetrical tuning function shown. Note that the only binaural change here is in the relative timing of these fixed PSPs. This is different for changes in IID only (ITD fixed at 0 ms), for which pairs of PSPs are shown in Figure 4.8H (IIDs of -20, 0, and +20 dB). As expected, the changes in level affect the amplitude of the PSPs, but they also have a large, clear effect on latency: the latency differences between onset of EPSP and IPSP are actually larger than the ITDs (± 0.3 ms) imposed in Figure 4.8I. This results in a

nonlinear interaction when both cues are combined, causing a marked functional change in the tuning function (Figure 4.8J). For the cue combination favoring the ipsilateral ear (both cues < 0 ; Figure 4.8J, left panel), the large and early EPSP is not effectively opposed by the small and later arriving IPSP: this results in a higher probability of spiking than for ITD or IID alone. For the combination favoring the contralateral ear (both cues > 0) (Figure 4.8J, right panel), a large and leading IPSP opposes a late and small EPSP: this results in a lower probability of spiking than for ITD alone. The effect of cue combination is therefore to remove the “right” slope of ITD-tuning, and to generate a steep “left” slope closer to 0 ITD (Figure 4.8C).

This is illustrated (Figure 4.8K, same cell) for a broad set of cue combinations. Artificial, single cue variations (Figures 4.8H and 4.8I) correspond to the vertical (grey) and horizontal (cyan) lines. For a real sound source moving in azimuth, the trajectory through this cue space is oblique (magenta): the exact trajectory depends on stimulus spectrum (Maki and Furukawa, 2005) but it generally courses from a region of high spike probability (lower left quadrant) to a region of low spike probability (upper right quadrant). Spike rates corresponding to these three cuts, for a broad range of cues, are shown in Figure 4.8L. Compared to the ITD-only condition (cyan), cue combination (magenta) indeed removes ambiguity by the absence of response for stimuli in the ipsilateral hemifield (IID > 0 , ITD > 0), and results in a steeply-sloped tuning function positioned closer to 0. More limited datasets for three other cells, showing similar effects, are shown in Figure 4.8-figure supplement 2.

In summary, striking specializations at 3 levels combine to make LSO principal cells spatially tuned to transient sounds. Exquisite timing in afferent inputs supplies these neurons with temporally punctate events; the intrinsic properties of the neurons enable these events to interact at a sub-millisecond timescale; and the opposite sign and strategic location of the inputs enable input from one ear to veto the input from the other ear. The net result is sharp tuning to sound transients, which moreover is coherent with IID-tuning to sustained sounds in non-principal cells.

DISCUSSION

Our data lead to a new view of brainstem binaural processing, departing strongly from the previously accepted roles of the MSO as a timing comparator and the LSO as an intensity comparator. We find that both excel as timing comparators, be it for different types of sounds, complementary in frequency range and temporal characteristics. Our data show that principal LSO cells are significantly more temporally specialized than was previously appreciated, towards one specific, highly ecologically relevant form of binaural sensitivity which has received little attention: to sound transients (Joris and Trussell, 2018). Using diverse specializations, excitatory and inhibitory afferent circuits supply exquisitely timed PSPs to both MSO and LSO. By directing well-timed inhibition to the AIS, and combined with fast membrane properties of the LSO principal cells themselves, this circuit enables the output of one ear to veto the output of the other ear in a manner that is punctate in space and time. In contrast, binaural sensitivity of MSO neurons to these stimuli is surprisingly poor.

Traditionally, the LSO is viewed as the brainstem nucleus underlying behavioral sensitivity to IIDs. A long-standing problem with this depiction is that it lacks a rationale for the extreme features of the LSO-circuit, which hinder, rather than help IID sensitivity and which suggest a key role for timing. These features include large axosomatic synapses such as the calyx of Held, differential axon diameters on ipsi- and contralateral side, and fast membrane properties of monaural inputs (Joris and Trussell, 2018). Despite these features, ITD-sensitivity of LSO neurons is weak (Caird and Klinke, 1983; Joris, 1996; Joris and Yin, 1995; Tollin and Yin, 2005, 2002), except to sound transients as documented *in vivo* for a limited number of neurons (Caird and Klinke, 1983; Irvine et al., 2001; Joris and Yin, 1995; Park et al., 1996) and *in vitro* with bilateral electrical shocks (Sanes, 1990; Wu and Kelly, 1992). It was recently argued that spatial sensitivity to high-frequency transients is particularly important for small mammals living near the ground plane, to enable detection of adventitious transient sounds generated by movement of nearby animals (Joris and Trussell, 2018), which provides a rationale for the presence of the calyx of Held and other temporal features in the LSO-circuit. The data reported here are largely

in line with this hypothesis. Combined with the recent finding that principal neurons of the LSO have fast kinetics that have been undersampled in extracellular studies (Franken et al., 2018), the data underscore that temporal aspects of binaural sensitivity are an essential feature of this nucleus.

LSO neurons show acute tuning to ITDs of transient stimuli to an extent that surpasses that of neurons in the MSO, which is classically regarded as the nexus of ITD-sensitivity (Figures 1-3). Intracellular traces to monaural stimulation reveal the presence of extraordinarily well-timed excitation and inhibition in LSO neurons (Figure 4.2). We discovered a “prepotential” (Figure 4.2A, Figure 2-figure supplement 1C) preceding the IPSP with short latency in response to a transient at the contralateral ear, suggesting high synchronization between the many small inhibitory inputs. In response to binaural stimulation, inhibition is remarkable in its depth, temporal acuity, reliability, and limited duration of its effect. Effective interaction between EPSP and IPSP occurs over a time window which is only a small fraction of the latter’s duration, and generates steeply-sloped and narrow ITD-tuning (Figures 4.1 and 4.2). Application of inhibition *in vitro* by somatic conductance clamp (Figure 4.4) or current injection (Figure 4.4-figure supplement 1), was ineffective to completely suppress spiking, as opposed to synaptically driven inhibition. This suggested that at least some synaptically-evoked inhibition acts electrotonically closer to the spike initiation region in the axon. Indeed, morphological examination at the light (Figure 4.5) and EM (Figure 4.6) level revealed glycinergic terminals at the AIS of LSO but not MSO neurons (Figure 4.6-figure supplement 1B). Computational modeling demonstrated that inhibition targeting the soma and the AIS can suppress spiking more strongly than inhibition limited to the soma (Figure 4.7).

Our assertion is not that there is no IID-sensitivity in LSO, which has been abundantly demonstrated both to sustained and transient sounds, or that ITD is the only important binaural cue. Rather, it is that the LSO is temporally specialized towards binaural processing of sound transients. This is most easily explored with “pure” temporal cues, i.e. ITDs of transients. However, these specializations will be engaged by, and affect responses to, any stimulus transient, even if stimulus ITD is not varied explicitly. Our recordings

show directly that IIDs affect both amplitude and timing of EPSPs and IPSPs (Figure 4.8). It has often been proposed that IIDs are translated to ITDs through a peripheral latency mechanism (the “latency hypothesis” (Jeffress, 1948)). Response latency generally decreases with sound level, so an acoustic IID would generate a neural ITD pointing to the same side. Human psychophysical studies do not support a simple IID-to-ITD conversion for low-frequency, ongoing sounds (Domnitz and Colburn, 1977). Indeed, for such sounds, IIDs are small (Maki and Furukawa, 2005), and the relationship between intensity and latency is complex (Michelet et al., 2010). However, EPSPs and IPSPs show large and systematic latency changes in response to transient sounds (Figures 4.8D-8G). Physiological evidence for an interaction between IID and ITD has been observed for transient responses in a variety of species and anatomical structures (Irvine et al., 2001; Joris and Yin, 1995; Park et al., 1996; Pollak, 1988; Yin et al., 1985), but in these extracellular recordings the underlying cellular mechanisms could not be assessed. Our intracellular recordings enabled direct examination and comparison of amplitude and timing of IPSPs and EPSPs and their relation to binaural responses. Our results suggest a different view of the role of latency changes. Both through the properties of its inputs and its intrinsic properties, the LSO is uniquely endowed to combine the two binaural cues. First, PSPs are not only extraordinarily precisely timed but also scale in both amplitude and latency with intensity: the large IIDs present at high frequencies (20 dB or more (Maki and Furukawa, 2005)) translate into delays that are substantial relative to the animal’s headwidth ($\sim 120 \mu\text{s}$ for gerbil) and that add to the stimulus ITD. Second, the ears have opposite signs: one ear can veto the other ear but only over a very narrow time window. These properties, which rely on a range of specialized features both in the input pathway and the LSO cells themselves, all combine in neural space towards a single pair of PSPs that results in an unambiguous output signalling an ipsilateral (high output) or contralateral (no output) sound source for the range of cue values available to the animal (Figure 4.8).

We were able to collect data on exhaustive combinations of ITD and IID for only a small number of cells, since this requires holding the neurons very long. It is therefore not clear where the slopes of the tuning functions are positioned relative to the physiological

range for the population of principal LSO neurons (Figure 4.8K,L; Figure 8 – figure supplement 2B). We find that this can also vary with sound level (Fig. 4.1 – figure suppl. 3 A,B). Future studies need to address how these cells respond to adventitious sounds in natural environments using stimuli in virtual space or free-field.

Comparison of monaural and binaural responses reveals why the EE (excitatory-excitatory) interaction underlying coincidence detection in MSO results in poorer binaural sensitivity to ITDs of clicks than the IE (inhibitory-excitatory) interaction underlying anti-coincidence detection in LSO. The multiplicative interaction in MSO hinges on subthreshold monaural inputs. Indeed, earlier modeling work has shown that a high level of monaural coincidences reduces sensitivity to ITDs for sustained sounds (Colburn et al., 1990; Franken et al., 2014), and various mechanisms counter the presence of monaural coincidences (Agmon-Snir et al., 1998). However, transient stimuli can synchronize sufficient monaural inputs to cause suprathreshold monaural coincidences in MSO neurons, and the sign of these responses is positive (increased spike rate) and identical for monaural stimulation (of either ear) and binaural stimulation, so that little response increment is gained with binaural stimulation. In contrast, in LSO neurons the response sign is opposite for the two ears and maximal binaural interaction is obtained when ITD causes an alternation in sign from robust excitation to profound inhibition. In this subtractive mechanism, strong monaural responses (of opposite sign) yield maximal binaural interaction.

The role of axo-axonic synapses in these temporal computations directly links axonal inhibition to a clear physiological operation (extraction of binaural cues towards sound localization). This makes this circuit a model system to study how such synapses modulate neuronal output at the single-cell level. Indeed, despite the well-known occurrence of axo-axonic synapses provided by chandelier cells in cortex, their physiological role has to a large extent remained a mystery (Pan-Vazquez et al., 2020). Our data indicate that inhibitory axo-axonic synapses cooperate with somatic inhibition to drastically reduce neuronal output with high temporal precision. This may help shed light on the function of such synapses elsewhere in the brain.

We conclude that the LSO pathway is not a simple IID pathway but consists of at least two subsystems with a coherent code for sound laterality. Principal cells encode spatial location of sound transients based on exquisite temporal sensitivity; non-principal cells encode spatial location of ongoing sound features, based on intensity. Given that principal cells are the most numerous cell type (Helfert and Schwartz, 1987; Saint Marie et al., 1989), and given the extreme nature of specializations in the afferent pathway and how they interact via the principal cells, the time-based role of LSO is the more dominant (but previously underestimated) role. This role may support fast and reliable localization of adventitious sounds, such as those made by approaching predators or prey.

MATERIALS AND METHODS

Key Resources Table					
Reagent (species) resource	type or	Designation	Source reference	Identifiers	Additional information
strain, background (<i>Meriones unguiculatus</i> , and female)	strain male	wildtype	<i>In vivo</i> : Janvier Labs <i>In vitro</i> : Animals raised in colony at UT-Austin Animal Resource Center (breeders obtained from Charles River Laboratories)		
antibody		anti-Synaptophysin1 (Guinea pig polyclonal)	Synaptic Systems	Cat# 101-004; RRID:AB_1210382	(1:500)

antibody	anti-AnkyrinG (rabbit polyclonal)	(Galiano et al., 2012)		(1:200) Courtesy of Dr. Matthew Rasband (Baylor College of Medicine)
antibody	anti-Gephyrin (mouse monoclonal)	Synaptic Systems	Cat# 147-011; RRID:AB_887717	(1:200)
software, algorithm	MATLAB	The Mathworks		
software, algorithm	IGOR-Pro	Wavemetrics		
software, algorithm	MafDC	(Yang et al., 2015)		Courtesy of Dr. Matthew Xu-Friedman
software, algorithm	SIM-post processing software	Zeiss		
software, algorithm	Metamorph	Molecular Devices		

Animals

For the *in vivo* recordings, adult (P60-P90) and juvenile (range P22-P35, median P29) Mongolian gerbils (*Meriones unguiculatus*) of both sexes were used. The animals had no prior experimental history and were housed with up to six per cage. This study was performed in accordance with the recommendations in the Guide for the Care and Use of Laboratory Animals of the National Institutes of Health. All *in vivo* procedures were approved by the KU Leuven Ethics Committee for Animal Experiments (protocol numbers P155/2008, P123/2010, P167/2012, P123/2013, P005/2014). After perfusion, the tissue of some of these animals were used for electron microscopic analysis.

For the *in vitro* recordings, Mongolian gerbils aged P19-22 were used. For the immunohistochemistry experiments, Mongolian gerbils aged P24-26 were used. All *in vitro* recording and immunohistochemistry experiments were approved by the University

of Texas at Austin Animal Care and Use Committee in compliance with the recommendations of the United States National Institutes of Health.

The methods for *in vivo* and *in vitro* patch clamp recording and electron microscopy have been previously described (Franken et al., 2018, 2016, 2015) and are briefly summarized here.

Surgery for *in vivo* electrophysiology

The animals were anesthetized by an intraperitoneal injection of a mixture of ketamine (80-120 mg/kg) and xylazine (8-10 mg/kg) in 0.9% NaCl. Anesthesia was maintained by additional intramuscular injections of a mixture of ketamine (30-60 mg/kg) and diazepam (0.8-1.5 mg/kg) in water, guided by the toe pinch reflex. Body temperature was kept at 37°C using a homeothermic blanket (Harvard Apparatus, Holliston, MA, USA) and a heating lamp. The ventrolateral brainstem was exposed by performing a transbulla craniotomy. This access allowed us to record from either LSO or MSO neurons. The contralateral bulla was opened as well to maintain acoustic symmetry. Meningeal layers overlying the exposed brainstem were removed prior to electrode penetration, and (cerebrospinal fluid) CSF leakage wicked up or aspirated. Pinna folds overlying the external acoustic meatus were removed bilaterally to ensure proper delivery of the acoustic stimuli.

***In vivo* electrophysiology**

Patch clamp pipettes were pulled from borosilicate capillaries (1B120F-4, World Precision Instruments, Inc., Sarasota, FL, USA) with a horizontal puller (P-87, Sutter Instrument Co., Novato, CA, USA). When filled with internal solution, electrode resistance was 5-7 M Ω , measured in CSF. The internal solution contained (in mM) 115 K-gluconate (Sigma); 4.42 KCl (Fisher); 10 Na₂ phosphocreatine (Sigma); 10 HEPES (Sigma); 0.5 EGTA (Sigma); 4 Mg-ATP (Sigma); 0.3 Na-GTP (Sigma); and 0.1-0.2% biocytin (Invitrogen). pH was adjusted to 7.30 with KOH (Sigma) and osmolality to 300 mOsm/kg with sucrose (Sigma). A patch clamp amplifier (BC-700A; Dagan, Minneapolis, MN, USA) was used to obtain membrane potential recordings, where the analog signal was low-pass filtered (cut-off frequency 5 kHz) and digitized at 50-100 kHz (ITC-18, HEKA, Ludwigshafen/Rhein, Germany; RX8, Tucker-Davis Technologies, Alachua, FL, USA). Data was collected using MATLAB (The Mathworks, Natick, MA, USA). *In vivo* whole-cell recordings were obtained from LSO and MSO neurons. Neurons were identified as principal LSO neurons, non-principal LSO neurons or MSO neurons using the same morphological and/or physiological criteria as in our earlier work (Franken et al., 2018, 2015). LSO and MSO samples cover the same range of CFs (range MSO: 508 Hz - 8000 Hz; range LSO: 437 Hz - 12021 Hz) (see e.g. Figures 1K and 1L). Series resistance was 61.8 ± 3.77 M Ω (mean \pm s.e.m., 19 cells, leaving out one cell with series resistance >100 M Ω) for LSO neurons and 70.6 ± 2.98 M Ω (mean \pm s.e.m., 28 cells, leaving out two cells with series resistance >100 M Ω) for MSO neurons. Opening resting membrane potential was -56.9 ± 0.56 mV (mean \pm s.e.m., 20 cells) for LSO neurons and -53.6 ± 0.74 mV (mean \pm s.e.m., 27 cells) for MSO

neurons, both corrected for a 10 mV liquid junction potential. Reported membrane potentials are typically presented as V_m rel, i.e. after subtracting resting membrane potential.

Acoustic stimuli

In vivo recordings were done with the animal in a double-walled sound-proof booth (IAC, Niederkrüchten, Germany). TDT System II hardware (Tucker-Davis Technologies, Alachua, FL, USA) was used to generate and present sound stimuli, using MATLAB (The Mathworks, Natick, MA, USA). Acoustic speakers (Etymotic Research Inc., Elk Grove Village, IL, USA) attached to hollow ear bars were positioned over the external acoustic meatus bilaterally. Acoustic calibration was done before each recording using a probe microphone (Bruel and Kjaer, Nærum, Denmark). Characteristic frequency (CF) was measured with a threshold-tracking algorithm during ipsilateral short tone presentation, using either spikes or large EPSPs as triggers. CF was defined as the tone frequency with the lowest threshold. For some cells, CF was not recorded: we then report best frequency (BF) i.e. the frequency that elicits the maximal response for tones of the same sound level. Responses were obtained to monaural and binaural rarefaction clicks (rectangular pulse scaled according to the acoustic calibration, duration 20 μ s). Monaural ipsilateral and monaural contralateral responses were typically obtained to different sound levels (from -10 or 0 dB SPL to \sim 80 dB SPL, in steps of 2-10 dB), for 5 or 10 repetitions per sound level and 100 or 200 ms in between successive clicks. A binaural data set was often obtained using the same parameters. Then, responses were obtained to binaural clicks where ITD was varied. Sound level was set at a value for which monaural ipsilateral responses were suprathreshold. ITD was varied in steps of 100 μ s, and 10-20 repetitions were typically obtained per ITD. ITD responses were often obtained at several sound levels. For some neurons, responses were obtained to binaural clicks for which IID was varied. Positive ITDs and positive IIDs refer to stimuli for which respectively the contralateral stimulus leads the ipsilateral stimulus or the contralateral stimulus is more intense than the ipsilateral stimulus.

For many of these neurons, responses to tonal stimuli have been reported before (LSO: Franken et al., 2018; MSO: Franken et al., 2015).

Analysis

Data analysis was performed in MATLAB. Custom MATLAB code for the computational model is provided as a source code file.

Analysis of *in vivo* data

ITD functions were smoothed by convolution with a 3-point Hanning window (MATLAB function *hanning*) for the population plots in Figures 1G-I and Figure 1-figure supplement 2, and before measuring slope steepness (Figure 1J) and halfwidth (Figure 1K).

To quantify the modulation of spike rate as a function of ITD (Figure 1L) we used the ITD-SNR metric which has been described by Hancock *et al.* (Hancock et al., 2010). ITD-SNR was calculated for all data sets with ≥ 10 repetitions and is defined as

$$ITD\ SNR = \frac{\sigma_{ITD}^2}{\sigma_{tot}^2}$$

σ_{ITD}^2 stands for the variance in spike counts related to the ITD and is defined as

$$\sigma_{ITD}^2 = \frac{1}{N_s} \sum_{s=1}^{N_s} (\bar{R}_s - \bar{R})^2$$

where \bar{R}_s is the mean spike count for each ITD value s across trials and \bar{R} is the grand mean of \bar{R}_s across ITD values. σ_{tot}^2 , the total variance is defined as

$$\sigma_{tot}^2 = \frac{1}{N_s N_t} \sum_{s=1}^{N_s} \sum_{t=1}^{N_t} (R_{s,t} - \bar{R})^2$$

where N_s is the number of different ITD values, N_t is the number of trials per ITD and $R_{s,t}$ is the spike count in response to ITD s during trial t .

To compare binaural responses to monaural response, we defined a summation ratio. For LSO neurons, this ratio is defined as

$$SR_{LSO} = median \left(\frac{\bar{R}_{spl,ipsi} + \bar{R}_{spl,contra}}{\bar{R}_{spl,bin}} \right)$$

where \bar{R}_{spl} stands for the mean spike count across trials to a stimulus with sound level spl . SR_{LSO} is then calculated as the median ratio across sound levels. Because LSO neurons are excited by ipsilateral sounds but inhibited by contralateral sounds, a strong binaural effect means that the response to binaural stimuli is a lot smaller than the sum of monaural ipsilateral and monaural contralateral responses, and this will result in large values of SR_{LSO} . If instead binaural stimulus presentation results in the same average spike count as the sum of monaural ipsilateral and monaural contralateral stimulation, SR_{LSO} will be equal to 1.

For MSO neurons, the summation ratio is defined instead as

$$SR_{MSO} = median \left(\frac{\bar{R}_{spl,bin}}{\bar{R}_{spl,ipsi} + \bar{R}_{spl,contra}} \right)$$

Since MSO neurons are excited by monaural ipsilateral as well as monaural contralateral sounds, a strong binaural effect will result in $\bar{R}_{spl,bin}$ being much larger than the sum of $\bar{R}_{spl,ipsi}$ and $\bar{R}_{spl,contra}$. Inverting the ratio in the definition of SR_{MSO} compared to SR_{LSO} thus means that both metrics are $\gg 1$ when there is a significant binaural advantage compared to monaural stimulation.

To generate the Voronoi diagrams (Figure 8K; Figure 8-figure supplement 2), we used the MATLAB function *voronoin* to generate Voronoi cells for all available combinations of ITD and IID. ITD values were divided by 0.05 ms/dB before feeding them in *voronoin* together with IID values in dB. Each Voronoi cell was colored according to spike rate.

***In vitro* electrophysiology**

The animals were perfused and subsequently sectioned under a Na⁺-free solution containing: 135mM N-Methy-D-Glucamine (NMDG), 20mM D-Glucose, 1.25mM KCl, 1.25mM KH₂PO₄, 2.5mM MgSO₄, 0.5mM CaCl₂, and 20mM Choline Bicarbonate (pH adjusted to 7.45 using NMDG powder, final osmolarity: 310 mOsm). Coronal slices were prepared and incubated at 37°C in a recovery solution: 110mM NaCl, 25mM D-Glucose, 2.5mM KCl, 25mM NaHCO₃, 1.25mM NaH₂PO₄, 1.5mM MgSO₄, 1.5mM CaCl₂, 5mM N-Acetyl-L-Cystine, 5mM Sodium ascorbate, 3mM sodium pyruvate, and 2mM Thiourea (pH adjusted to 7.45 with NaOH, final osmolarity: 310 mOsm). Following 30-45 minutes of recovery, slices were maintained at room temperature for >30 minutes before recording. Whole-cell current-clamp recordings were made using Dagan BVC-700A amplifiers. Voltage data was filtered at 5 kHz, digitized at 100 kHz, and stored on computer using Igor Pro (Wavemetrics). Recording electrodes were pulled from borosilicate glass (1.5mm OD; 4-8MΩ) and filled with intracellular solution containing 115 mM K-gluconate, 4.42 mM KCl, 0.5 mM EGTA, 10 mM HEPES, 10 mM Na₂Phosphocreatine, 4 mM MgATP, and 0.3 mM NaGTP, osmolality adjusted to 300 mOsm/L with sucrose, pH adjusted to 7.30 with KOH. All recordings were carried out at 35°C with oxygenated ACSF perfused at a rate of ~2-4 mL/min, and bridge balance and capacitance compensation were monitored throughout. Series resistance was maintained below 10 MΩ for dynamic clamp experiments, and electrode capacitance was fully compensated. All membrane potentials shown are corrected for a 10 mV liquid junction potential.

ITD dynamic clamp experiments were carried out and analyzed under control of a user interface using Igor Pro routines kindly provided by Dr. Matthew Xu-Friedman (MafDC; Yang et al., 2015). Dynamic clamp was implemented at 50 kHz via an ITC-18 computer interface (Heka Instruments). Excitatory and inhibitory conductances and currents were simulated with double exponential waveforms (EPSCs/EPSPs: time constants = 0.1 ms rise, 0.18 ms decay, reversal potential of 0 mV; IPSCs/IPSPs: time constants = 0.45 ms rise, 2.0 ms decay, reversal potential of -75 mV), based on published literature for the age range used for slice experiments in gerbils and other rodents (Walcher et al., 2011; Kullmann and Kandler, 2001; Balakrishnan et al., 2003; Kakazu et al., 1999; Ehrlich et al., 1999). The amplitude of EPSCs and EPSPs was adjusted 20% above threshold for reliable spike initiation. The peak conductance of IPSPs and amplitude of IPSCs were adjusted so that an individual event elicited a 5-10 mV hyperpolarization from the resting potential

(similar as IPSP amplitudes observed *in vivo* at a similar resting potential). The resting potential was maintained at -60 mV with direct current through the recording electrode to maintain consistent driving forces on excitatory and inhibitory synaptic currents across different experiments. Synaptic stimuli were evoked through glass pipettes (50-100 μM dia.) via a constant current stimulator (Digitimer DS3), and presented with random temporal offset intervals. Small current steps were interleaved to monitor input resistance. Synaptic stimulation was ipsilateral to the LSO for excitatory input stimulation, or near the center of the MNTB for inhibitory stimulation. Excitatory and inhibitory responses were isolated through the inclusion of 1 μM strychnine or 10 μM NBQX to the bath, respectively. Stimulation intensity was also adjusted so that action potential probability at optimal synaptic timing was close to, but less than 100%, to avoid saturation.

Similar to the *in vivo* ITD functions, slope values of *in vitro* functions (Figure 4E, Figure 4-figure supplement 1C) were measured after smoothing the function with a 3-point Hanning window (MATLAB function *hanning*).

Immunohistochemistry and SIM microscopy

The brainstem of Mongolian gerbils (P24-26) were rapidly dissected, blocked in the coronal plane, and drop fixed in cold 4% paraformaldehyde for 30-60 min. Tissue was cryoprotected in a gradient of sucrose solutions (20% sucrose overnight, 30% sucrose overnight; 4°C), and subsequently embedded in Optimal Cutting Temperature (O.C.T.) media. Sections were sliced on a cryostat (16-20 μm ; -19°C) and mounted on slides for immunohistochemistry.

Tissue on slides were rehydrated in 0.1M PBS for 5-10 min. Sections were blocked and permeabilized with PBTGS (10% Goat Serum, 0.3% Triton in 0.1M PBS) for 1.5 hours in a humidity chamber at room temperature on a slow-moving shaker. The tissue was then incubated with a primary antibody solution in PBTGS for 48 hours at 4°C. Primaries included mouse anti-Gephyrin (1:200; Synaptic Systems [cat. #147-011]), rabbit anti-AnkyrinG (1:200; Courtesy of Dr. Matthew Rasband; Baylor College of Medicine (Galiano et al., 2012)), and guinea pig anti-Synaptophysin1 (1:500, Synaptic Systems [cat. #101-004]). After primary incubation, the tissue was gently washed 3x with 0.1M PBS (5;10;15 min intervals) at room temperature. Tissue was then incubated for 2 hours at room temperature in a PBTGS secondary antibody solution including goat anti-mouse Alexa568 (1:200; Abcam [ab175473]), goat anti-rabbit Cy2 (1:200; Jackson Laboratories Inc. [111-225-144]), and goat anti-guinea pig 647 (1:200, Abcam [ab150187]). Slides were again washed 2x with 0.1M PBS, and a third wash (15 min) was done in 0.05M PBS. Tissue was then partially dried, and cover slipped with Fluoromount-G containing DAPI. After drying for 24 hours, slides were cover slipped and sealed with nail polish (24hrs) for imaging.

Low power images of the LSO (112x magnification) were taken on a Zeiss Stereoscope (Axio Zoom.V16). LSO nuclei were subsequently imaged using SIM-microscopy (Zeiss LSM710 with Elyra S.1) and z-stacks of targeted regions were generated (~0.5 μm optical sections; total ~15 μm). Post-SIM processing of multichannel images (488; 568; 647nm) was done offline using Zeiss SIM post-processing software with a Wiener filter setting between -5.0 and -5.2, followed by individual channel deconvolution using Metamorph

software (Molecular Devices). The resulting images were not used for direct quantifications of anatomical structures due to the presence of some remaining SIM processing artifacts introduced by unavoidable light scatter in the tissue sections. Imaging was targeted towards AIS that ran in a single optical plane.

Histology and electron microscopy of cells labeled with biocytin during *in vivo* recording

After the recording session, the animal was euthanized with pentobarbital and perfused through the heart with 0.9% NaCl followed by paraformaldehyde (PFA) 4% in 0.1M phosphate buffer or (for electron microscopy analysis) by PFA 1%/glutaraldehyde 1% and PFA 2%/glutaraldehyde 1%. Tissue processing methods for light and electron microscopy have been described previously (Franken et al., 2018; Smith et al., 2010, 2005) and are summarized here. The brain was dissected out of the skull and stored in PFA 1%/glutaraldehyde 1% for at least 24h. A vibratome was used to cut sections (70 μ m thick) and the DAB-nickel/cobalt intensification method (Adams, 1981) was then used to visualize biocytin. After rinsing in phosphate buffer, free-floating sections were inspected with a light microscope to locate the labeled neuron. Sections containing the labeled cell body and relevant portions of the axon were processed for electron microscopy. These were fixed in 0.5% osmium tetroxide for 30 minutes, rinsed and dehydrated through a series of graded alcohols and propylene oxide. They were then placed in unaccelerated Epon-Araldite resin and transferred into a fresh batch of unaccelerated resin overnight. The sections were then embedded in plastic and flat mounted in accelerated resin between Aklar sheets at 65°C. The region of the embedded sections containing the labeled neuron and its axon, that typically arose from the cell body, were cut out and mounted on the flattened face of a plastic beam capsule. The 70 μ m section was re-sectioned into 3 μ m sections which were placed on a glass coverslip. The 3 μ m sections containing the labeled neuron and the first 50-100 μ m of the axon were selected and remounted on a beam capsule. Thin sections (70-80 nm) were then cut and mounted on coated nickel grids. These sections were stained with uranyl acetate and lead citrate and examined using a Philips CM-120 electron microscope.

Cell types were identified using morphological and physiological criteria as described before (Franken et al., 2018; Helfert and Schwartz, 1987). Briefly, principal LSO cells were identified by the central location of their cell body in the LSO, bipolar dendritic arbors in the transverse plane, high levels of cell body synaptic coverage at the E.M. level (>50%), small action potentials and fast subthreshold kinetics.

Statistics

All error bars represent standard error of the mean. Data distribution was not formally tested for normality. Exact p -values are given and all p values are two-tailed. Statistical significance was defined as $p < 0.05$. A non-parametric effect size measure, η^2 , estimated as the Mann-Whitney U statistic divided by the product of sample sizes, is reported for two-sample statistical analyses (Newcombe, 2006a; η^2 ranges from 0 to 1 and $\eta^2 = 0.5$ in case of no effect). 95% confidence intervals for η^2 were calculated using freely available

software in Excel developed by Dr. Robert Newcombe (Cardiff University, <http://profrobertnewcomberesources.yolasite.com/>), using method 5 by Newcombe (Newcombe, 2006b)). Pearson's correlation coefficient r , and associated 95% confidence interval and p -value were calculated using the MATLAB function *corrcoef*. For *in vivo* data, multiple data sets were often available from the same cell (at different sound intensities, and/or at different frequencies (for tones)). Before doing statistical analyses, metrics were averaged per cell across these different data sets so that each cell contributes one data point to the analysis.

Computational model

Two-compartment model:

A two-compartment model gives a minimal description of a cell with two distinguishable spatial regions. The two regions in the model are soma (compartment 1) and axon initial segment region (AIS, compartment 2). Voltage dynamics in the two compartments are governed by the differential equations:

$$\begin{aligned} AC_m V_1' &= -A G_{lk1} (V_1 - E_{lk,1}) - g_{ax} (V_1 - V_2) - I_{syn,1} \\ \alpha A C_m V_2' &= -\alpha A G_{lk2} (V_2 - E_{lk,2}) - g_{ax} (V_2 - V_1) - I_{ion} - I_{syn,2} \end{aligned}$$

Specific membrane capacitance is $C_m = 0.9 \mu\text{F}/\text{cm}^2$ (Gentet et al., 2000). The ratio of membrane areas between the two compartments is $\square = 0.12$, based on anatomical observations that the soma is ellipsoid in shape with length $20.4\mu\text{m}$ and width $9.5\mu\text{m}$ (Helfert and Schwartz, 1987) and the AIS is cylindrical with length $20\mu\text{m}$ and diameter $1\mu\text{m}$ (Bender and Trussell, 2012). The remaining parameters are the effective soma area (A), leak reversal potential (E_{lk}), leak conductance density (G_{lk} , can differ in the two compartments), and axial conductance (g_{ax}). We describe these parameters in more details below. Their values are set so that passive dynamics of V_1 match typical properties LSO neurons (resting potential -60 mV , input resistance $40 \text{ M}\square$, and time constant 1 ms , (Sanes, 1990; Ashida et al., 2017)).

Conductance parameters determined from steady-state responses:

Conductance parameters are set based on passive, steady-state responses to constant inputs (following the approach of (Goldwyn et al., 2019)). The passive version of the two-compartment model is

$$\begin{aligned} c_m U_1' &= -g_1 U_1 - g_{ax} (U_1 - U_2) - I_1 \\ \alpha c_m U_2' &= -g_2 U_2 - g_{ax} (U_2 - U_1) - I_2 \end{aligned}$$

where U_1 and U_2 measure the deviation of voltages from resting potential in each compartment, c_m is the membrane capacitance (pF), g_1 and g_2 are passive (leak) conductance in each compartment (nS), and I_1 and I_2 are input currents (pA).

Steady-state voltages in response to constant inputs satisfy the linear equations

$$0 = -g_1 U_1 - g_{ax} (U_1 - U_2) - I_1$$

$$0 = -g_2 U_2 - g_{ax}(U_2 - U_1) - I_2$$

from which we calculate the input resistances for the two compartments:

$$R_1 = \frac{g_2 + g_{ax}}{(g_1 + g_{ax})(g_2 + g_{ax}) - g_{ax}^2}$$

$$R_2 = \frac{g_1 + g_{ax}}{(g_1 + g_{ax})(g_2 + g_{ax}) - g_{ax}^2}$$

and the transfer resistance between compartments

$$R_{12} = R_{21} = \frac{g_{ax}}{(g_1 + g_{ax})(g_2 + g_{ax}) - g_{ax}^2}.$$

From steady-state solutions to these equations we can also measure the attenuation of voltage from one compartment to the other. Forward attenuation (soma-to-AIS) for constant input to the soma is

$$\kappa_{1 \rightarrow 2} \equiv \frac{U_2}{U_1} = \frac{g_{ax}}{g_{ax} + g_2}$$

and backward attenuation (AIS-to-soma) for constant input to the AIS is

$$\kappa_{2 \rightarrow 1} \equiv \frac{U_1}{U_2} = \frac{g_{ax}}{g_{ax} + g_1}$$

We refer to these as forward and background coupling constants (Goldwyn et al., 2019). They take values between 0 (no coupling, complete voltage attenuation) and 1 (complete coupling, no voltage attenuation). We invert the above relations to construct a family of models, uniquely determined by the pair of coupling constants (see also (Goldwyn et al., 2019)):

$$g_{ax} = \frac{1}{R_1} \left(\frac{\kappa_{2 \rightarrow 1}}{1 - \kappa_{1 \rightarrow 2} \kappa_{2 \rightarrow 1}} \right)$$

$$g_1 = g_{ax} \left(\frac{1}{\kappa_{2 \rightarrow 1}} - 1 \right)$$

$$g_2 = g_{ax} \left(\frac{1}{\kappa_{1 \rightarrow 2}} - 1 \right)$$

where the soma input resistance $R_I = 40 \text{ M}\Omega$ (Sanes, 1990; Ashida et al., 2017). Values of these conductance parameters across the space of coupling constants are shown in Figure 7-figure supplement 1A-C.

A relation that we make use of in our analysis of AIS-targeting inhibition is

$$R_1 \kappa_{1 \rightarrow 2} = R_2 \kappa_{2 \rightarrow 1}.$$

This can be observed from the equations for input resistance and coupling constants, or by recognizing that $R_1 \kappa_{1 \rightarrow 2}$ and $R_2 \kappa_{2 \rightarrow 1}$ are identical because they are both equivalent to the transfer resistance between compartments. Under a steady-state approximation, soma-targeting inputs affect AIS voltage in proportion to $R_1 \kappa_{1 \rightarrow 2}$ and AIS-targeting inputs affect

AIS voltage in proportion to R_2 . The ratio of these is $\kappa_{2 \rightarrow 1} = R_1 \kappa_{1 \rightarrow 2} / R_2$ and thus the backward coupling constant plays a key role in amplifying the strength of AIS-targeting inhibition. We used $\kappa_{2 \rightarrow 1} = 0.6$ in most simulations (Figure 7A,B) because action potential amplitudes in the soma are approximately 30 mV for this backward coupling strength, consistent with AP sizes observed *in vivo* (Franken et al. 2018) and confirmed that our results remained qualitatively consistent for other backward coupling strengths (Figure 7C).

Effective soma area determined by passive dynamics:

Soma dynamics are commonly described by a membrane time constant describing the rate of exponential decay to rest. In contrast, voltage in the passive two-compartment model evolves on two time scales. If the area ratio between soma and AIS (α) is very small, a separation of time-scales argument can be used to isolate a dominant time scale (Goldwyn et al., 2019). We could not pursue this approach here since $\alpha = 0.12$ is not sufficiently small. Nonetheless, we found it possible to roughly match the U_1 dynamics in the passive two-compartment model to exponential decay with a single time constant.

To do this, we considered decay from a steady-state holding potential in the passive model:

$$\begin{aligned} c_1 U_1' &= -g_1 U_1 - g_{ax}(U_1 - U_2) \\ \alpha c_1 U_2' &= -g_2 U_2 - g_{ax}(U_2 - U_1) \\ U_1(0) &= 1, U_2(0) = \kappa_{1 \rightarrow 2} \end{aligned}$$

Or, more compactly in matrix-vector notation as

$$\mathbf{u}' = -\mathbf{M}\mathbf{u}$$

where

$$\mathbf{M} = \begin{bmatrix} (g_1 + g_{ax})/c_1 & -g_{ax}/c_1 \\ -g_{ax}/\alpha c_1 & (g_2 + g_{ax})/\alpha c_1 \end{bmatrix}$$

and

$$\mathbf{u} = \begin{bmatrix} U_1(t) \\ U_2(t) \end{bmatrix}$$

and the initial value is $\mathbf{u}(0) = \begin{bmatrix} 1 \\ \kappa_{1 \rightarrow 2} \end{bmatrix}$.

Denoting the eigenvectors of \mathbf{M} as \mathbf{w}_i ($i=1,2$) with corresponding eigenvalues λ_i , the vector of voltage decay in both compartments is

$$\mathbf{u}(t) = a_1 \mathbf{w}_1 e^{-\lambda_1 t} + a_2 \mathbf{w}_2 e^{-\lambda_2 t}$$

where a_1 and a_2 are the coordinates of the initial value vector $\mathbf{u}(0)$ in the basis of eigenvectors (Boyce et al., 2018). We then compared the soma voltage $u_1(t)$ to exponential decay on a single time scale using the error function:

$$E(c_1) = \int_0^T \left(e^{-t/\tau_m} - u_1(t) \right)^2 dt.$$

where the membrane time constant is $\tau_m = 1$ ms (Sanes, 1990; Ashida et al., 2017). With $\alpha = 0.12$ and passive conductance parameters determined by the choice of coupling constants, the only remaining free parameter in the formula for $U_1(t)$ is c_1 . We determined a suitable value for c_1 by evaluating the error integral (with a finite upper limit, we use $T = 10$, but any limit sufficiently larger than τ_m gives similar results) and numerically determined the c_1 value that minimized the error function. in **Figure 7-figure supplement 1D** shows values of c_1 across the space of coupling configurations.

To summarize the parameterization method to this point: known, typical anatomical and physiological measurements of LSO neurons define a family of passive models. Each member of this family differs in its forward and backward coupling constants but has nearly identical passive soma voltage dynamics (see **Figure 7-figure supplement 1G** for examples).

Spike-generating currents:

Spike-generating sodium current and high-threshold potassium current are located in the AIS region (compartment 2). Hodgkin-Huxley-type descriptions of these currents were adapted from previous LSO models (Ashida et al., 2017; Wang and Colburn, 2012), specifically the adjusted Wang-Colburn model in Ashida et al., 2017). For each coupling configuration, maximal Sodium conductance was set so that spike threshold occurred for EPSPs in the soma of about 10 mV, similar to what we observed *in vivo*. We then set maximal high-threshold potassium conductance to be 10% of the maximal sodium conductance, consistent with Ashida et al. (2017). Values of maximal sodium conductance (g_{Na}) across the space of coupling constants are shown in Figure 7-figure supplement 1E. Examples of spiking dynamics for two different coupling configurations are shown in Figure 7-figure supplement 1H.

Synaptic inputs:

Synaptic currents were described as sums of unitary inputs of the form $g(t)(V_i - E_{syn})$ where $g(t)$ is the conductance waveform, V_i is the voltage in a compartment (excitation in soma only, inhibition can be in either soma or AIS), and E_{syn} is reversal potential (0 mV for excitation and -75 mV for inhibition). Conductance waveforms are the same as used in our *in vitro* experiments: double exponentials with rise time 0.1 ms and decay time 0.18 ms for excitation, and rise time 0.45 ms and decay time 2 ms for inhibition. Maximal conductances were 2.3 nS for excitation and 3.1 nS for inhibition. Synaptic populations consisted of 20 excitatory inputs and 8 inhibitory inputs, consistent with previous models of LSO neurons in which inhibitory inputs were fewer but stronger than excitatory inputs (Ashida et al., 2017; Gjoni et al., 2018b). To explore the impact of AIS-targeting inhibition, simulations were performed with different arrangements of inhibitory inputs including all eight inhibitory inputs to the soma, six soma inputs and two AIS inputs, and only two AIS inputs.

Each individual synapse in the population is activated independently at a fixed time and with identical probability. Thus the synaptic current of a given type (excitatory or inhibitory) is

$$I_{syn} = b_{N,p}g(t)(V_i - E_{syn})$$

where $b_{N,p}$ is binomial-distributed with success probability $p = 0.84$ (excitatory) and $p=0.92$ (inhibitory) and maximum possible number of inputs ($N=20$ for excitation, $N=2,6$, or 8 for inhibition depending on the arrangement of inhibitory inputs and compartment). These high probabilities reflect the fact that clicks elicit robust and reliable post-synaptic potentials in LSO neurons. The inhibitory probability of 0.92 was selected specifically so that the mean and variance of simulated IPSPs matched these statistics of IPSPs measured in a principal LSO cell *in vivo* in responses to contralateral clicks (Fig. 2A, mean IPSP = -6.35 mV, variance 0.184 mV).

We repeated the computational study using conductance waveforms adapted from a recent *in vivo* study of mature LSO neurons (Beiderbeck et al., 2018). These conductance waveforms were also double exponentials but with substantially faster inhibition kinetics. For this alternate parameter set, excitatory conductance had rise time 0.25 ms, decay time 0.4 ms, peak conductance 1.6 nS, and release probability 0.82 . Inhibitory conductance had rise time 0.35 ms, decay time 0.7 ms, peak conductance 3.9 nS, and release probability 0.92 . Results obtained using these synaptic inputs were broadly similar to the result presented in Figure 7. Faster inhibitory conductances narrowed the width of ITD tuning curves, see Figure 7-figure supplement 2.

Spike probability:

To make direct comparisons to neural recordings in which we measured spike probability in response to clicks, we simulated responses of the model to synaptic inputs (described above) and computed spike probability semi-analytically. Spiking dynamics in the model are deterministic, thus the probability of spiking is determined completely by the probabilistic description of the synaptic inputs. Let the random variables b_{N_E,p_E} and b_{N_I,p_I} be independent, Binomial-distributed random variables that represent the numbers of active excitatory and inhibitory inputs, respectively. Then the following defines the probability of a spike

$$P(\text{spike}|ITD) = \sum_{n_I=0}^{N_I} \sum_{n_E=0}^{N_E} \mathbb{1}(n_E, n_I, ITD) P(b_{N_E,p_E} = n_E) P(b_{N_I,p_I} = n_I)$$

The indicator function $\mathbb{1}(n_E, n_I, ITD)$ takes values of 0 (no spike) or 1 (spike). These binary values were determined by simulating the model in response to all possible input combinations at the specified ITD value and recording whether the AIS-voltage crossed a fixed threshold (-20 mV) or not.

Acknowledgements

We thank Anna Thiessen for her help in performing the electron microscopic analysis, Dr. Eric Verschooten for help with recording and analysis software. We also thank Dr. Kenneth Ledford for programming expertise in dynamic clamp experiments.

Competing interests

The authors declare no financial or non-financial competing interests.

FIGURE AND SUPPLEMENT LEGENDS

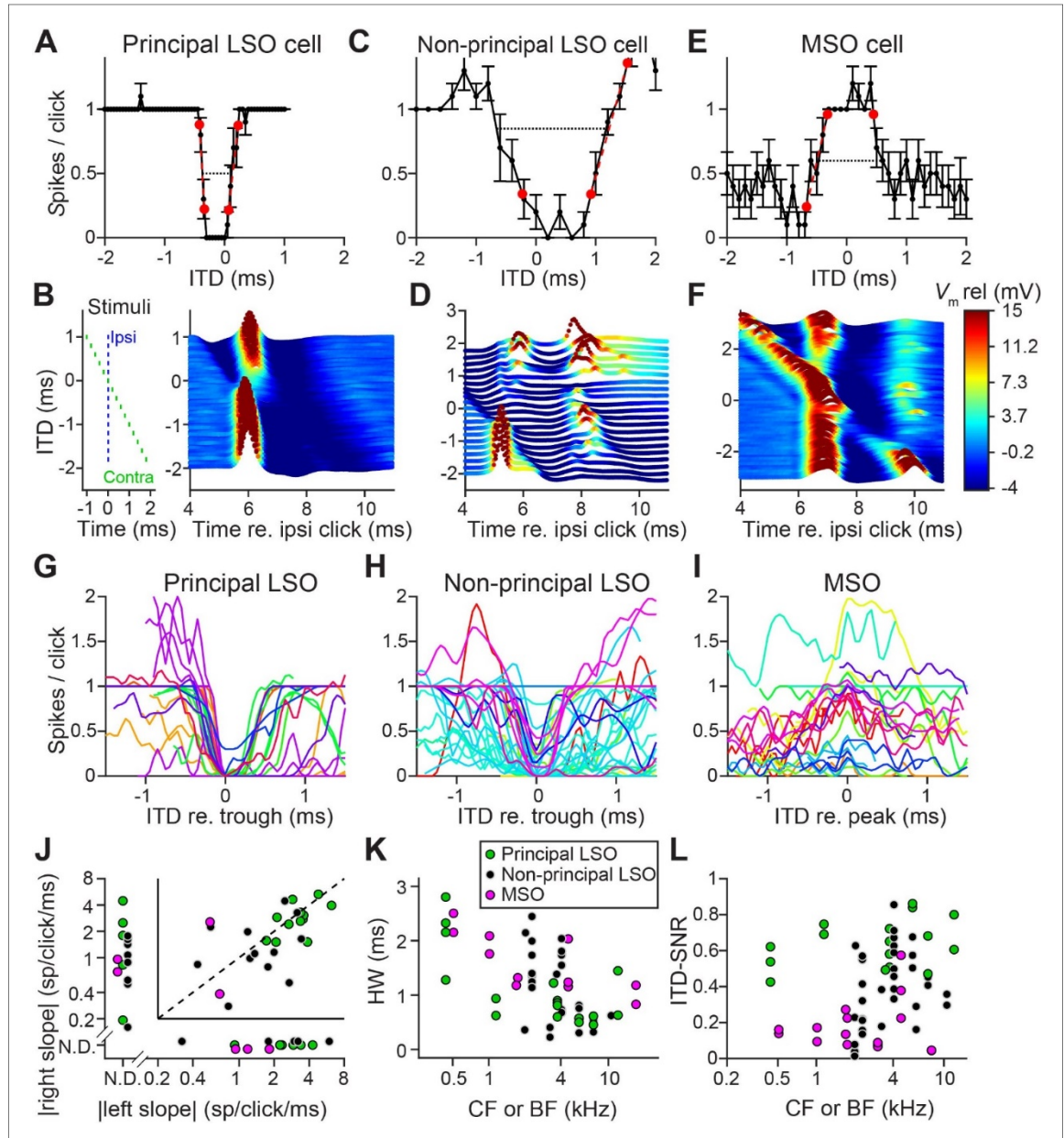


Figure 4.1. Sharp ITD-sensitivity to clicks in LSO but not MSO.

(A) Click-ITD function (10 repetitions) of an LSO principal cell (CF = 5.7 kHz). Data are represented as mean \pm SEM. Red circles indicate ITD values near the trough when the spike rate reached 20% or 80% of the maximum. Black dotted line indicates halfwidth of the central trough. By convention, negative ITD refers to the ipsilateral click leading the contralateral one, and vice versa for positive ITD. (B) Waterfall plots of the intracellular response of the cell in A. The membrane potential, averaged per ITD value across 10 repetitions, is color-coded. For clarity and to aid comparison with D and F, colors correspond to values clipped between the limits shown in the color scale in F. Inset on left indicates timing of the contralateral click (green) relative to the ipsilateral click (blue) for different ITDs. Leading or lagging inhibition does not affect the EPSP sufficiently to inhibit spiking, except over a small time window at ITDs near 0 ms. (C-F) Similar to A and B, for a non-principal LSO cell (C and D; CF = 4.1 kHz), and for an MSO neuron (E and F; CF = 4.6 kHz). In MSO, an excitatory response is present to clicks from either ear: there is some modulation of spike rate but it never decreases to 0. Red circles in E indicate ITD values where the spike rate reached 20% or 80% of the maximum. Black dashed line indicates halfwidth of the central peak. (G-I) Population of ITD functions for identified principal LSO neurons (G: 24 data sets, 8 cells), non-principal LSO neurons (H: 38 data sets, 11 cells) and MSO neurons (I: 25 data sets, 11 cells; 6 out of 11 cells were anatomically verified). To reduce clutter, tuning functions were aligned at the most negative ITD value of trough (G and H) or peak (I). Different colors indicate different cells. (J) Steepness of the slope (measured at 20% and 80% points) to the right of the central trough (for LSO cells) or peak (for MSO cells) plotted against steepness of the slope to the left of the central trough or peak. Abscissa and ordinate are scaled logarithmically. N.D.: data points for which either the left slope or the right slope is not defined because spike rate did not reach the respective threshold (e.g. the right slope of the MSO cell in E). Data sets for which both left and right slopes were not defined are not shown (LSO principal: 1 data set; LSO non-principal: 9 data sets; MSO: 10 data sets). Only cells for which the trough was lower than 0.5 sp/click (LSO) or the peak was higher than 0.5 sp/click (MSO) were included. Principal LSO (green): 23 data sets, 8 cells; Non-principal LSO (black): 27 data sets, 8 cells; MSO (magenta): 7 data sets, 4 cells. (K) Halfwidth of the central peak or trough as a function of CF or BF. Abscissa is scaled logarithmically. Only cells for which the trough was lower than 0.5 sp/click (LSO) or the peak was higher than 0.5 sp/click (MSO) were included. Principal LSO: 17 data sets, 8 cells; Non-principal LSO: 26 data sets, 9 cells; MSO: 11 data sets, 6 cells. (L) ITD-SNR (Hancock et al., 2010) as a function of CF or BF. Abscissa is scaled logarithmically. Principal LSO: 16 data sets, 7 cells; Non-principal LSO: 34 data sets, 9 cells; MSO: 16 data sets, 7 cells. Legend in K applies also to J and L. Numerical data represented as graphs in this figure are available in a source data file (Figure 1-Source data file 1).

The online version of this article includes the following figure supplements for Figure 1:
Figure supplement 1. Physiological data of LSO cells in Figure 1.

Figure supplement 2. Population data of ITD functions of Figure 1G-1I, without centering the left flank of the central trough (LSO) or peak (MSO) at 0 ms.

Figure supplement 3. ITD-sensitivity to clicks at different sound levels.

Figure supplement 4. ITD-sensitivity to clicks is steeper than to sustained sounds for LSO cells.

Figure supplement 5. Steep ITD-sensitivity to transients extends to rustling stimuli.

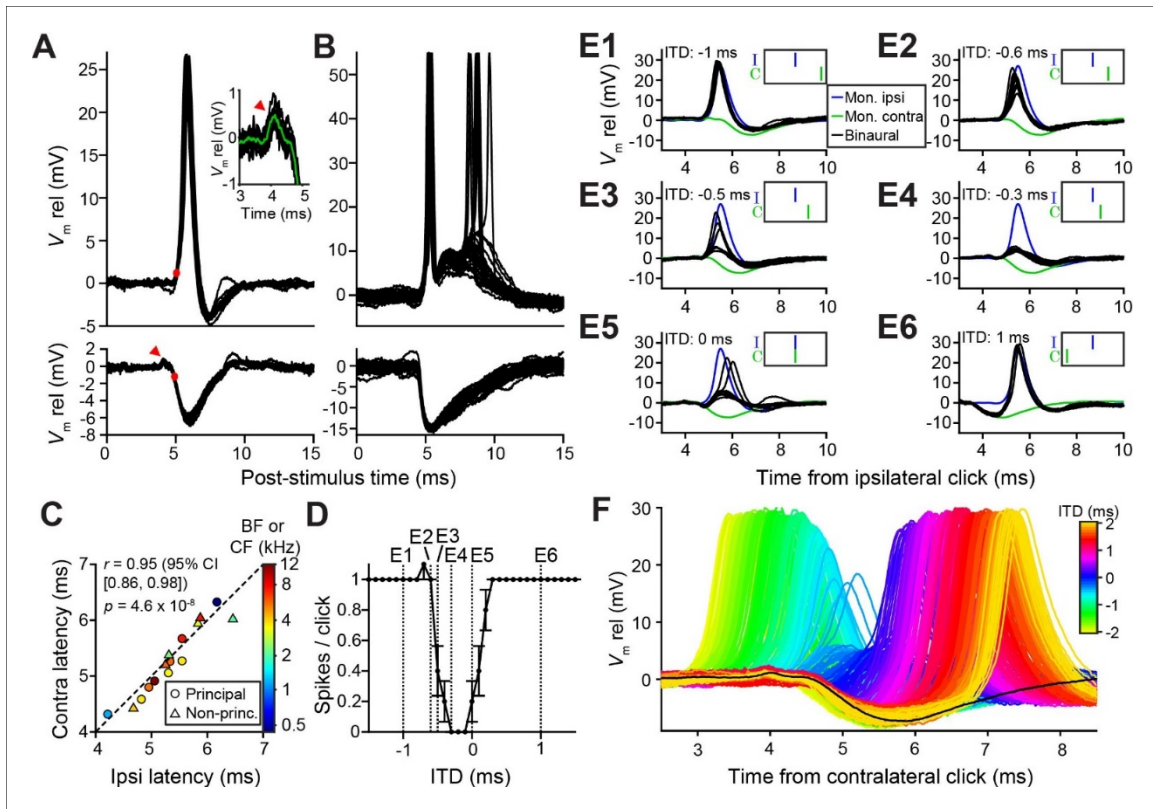


Figure 4.2. Precise timing and interaction of IPSPs and EPSPs in LSO neurons.

(A-B) Example responses to ipsilateral clicks (top panels) and contralateral clicks (bottom panels) for a principal LSO cell (A; CF = 12 kHz; 50 dB SPL; 10 repetitions) and a non-principal LSO cell (B; CF = 4.1 kHz; 20 dB SPL; 30 repetitions). Red arrowhead indicates prepotential, shown with a blowup in inset. (C) Ipsilateral versus contralateral latency of postsynaptic potentials evoked by monaural clicks for 9 principal cells (circles) and 6 non-principal LSO cells (triangles). Color indicates CF or BF for each cell. Latency was defined as the time relative to click onset when the membrane potential crossed a voltage difference relative to rest with an absolute value equal to 20% of the IPSP amplitude. For the ipsilateral response this voltage difference was a depolarization (red dot in top panel in A), for the contralateral response this voltage difference was a hyperpolarization (red dot in bottom panel in A). For this analysis we used the response to identical sound levels for ipsi and contra, at the lowest level generating a maximal monaural ipsilateral response. (D) Click-ITD function for the same neuron as in A. Data are represented as mean \pm SEM. Sound level 60 dB SPL at both ears. Dotted vertical lines correspond to the ITD values of the panels in E. (E1-E6) Average responses to monaural ipsilateral (blue) and monaural contralateral (green) clicks are compared to binaural responses (black) for the ITD values

indicated by dotted vertical lines in D. (F) Data from the same principal LSO cell as in A,D,E. Colored lines: responses to click pairs of different ITDs, referenced in time to the contralateral (inhibitory) click. Black line: averaged response to contralateral clicks at the same sound level as in D and E (corresponding to green line in E). Numerical data represented as graphs in this figure are available in a source data file (Figure 2—Source data file 1).

The online version of this article includes the following figure supplement for Figure 2:
Figure supplement 1. Precise interaction of IPSPs and EPSPs for another principal LSO neuron.

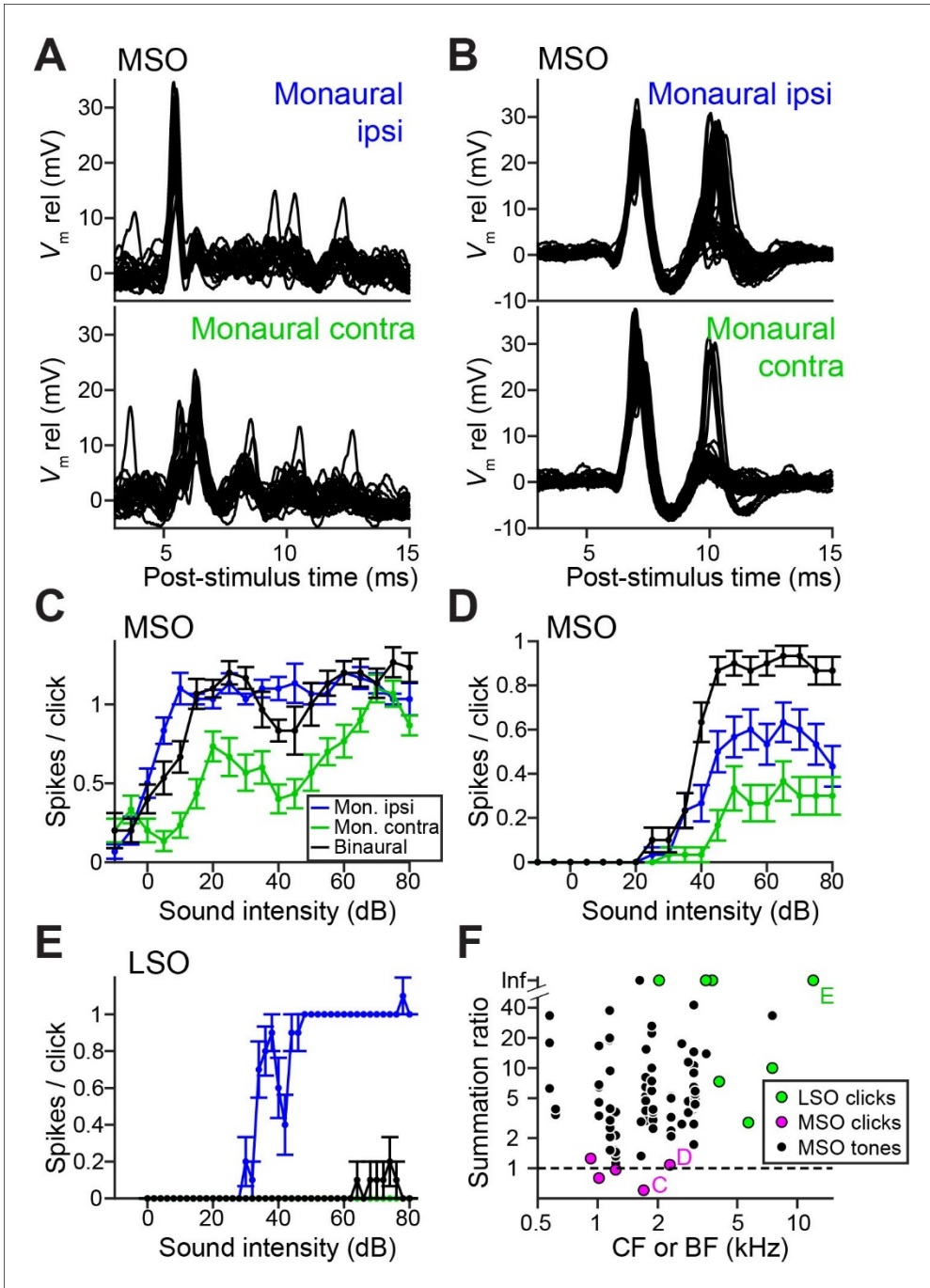


Figure 4.3. Weak ITD-tuning in MSO neurons results from a breakdown of coincidence detection for transients.

(A) Top panel: Example responses to ipsilateral clicks (top panel) and contralateral clicks (bottom panel) for an MSO cell (CF = 1.8 kHz). Sound level 70 dB SPL. 30 repetitions shown. (B) Similar to A, for another MSO cell (CF = 4.6 kHz). Sound level 70 dB SPL. 30 repetitions shown. (C) Rate-level functions (30 repetitions) for monaural clicks and for binaural clicks at 0 ITD for the same MSO cell as in A. Data are represented as mean \pm SEM. (D) Similar to C, for another MSO cell (CF = 2.3 kHz). 30 repetitions per SPL. (E) Similar to C and D, for a principal LSO cell (CF = 12 kHz). 30 repetitions per SPL. (F) Summation ratio for LSO responses to clicks (7 data sets, 7 cells), MSO responses to clicks (5 data sets, 5 cells) and MSO responses to sustained tones (77 data sets, 22 cells). For a summation ratio of one (dashed horizontal line), the binaural response equals the sum of the monaural responses. Letters C,D,E indicate data points of the cells in the corresponding panels. For MSO responses to tones, one data point with a summation ratio of ~ 200 is not shown. Numerical data represented as graphs in this figure are available in a source data file (Figure 3—Source data file 1).

The online version of this article includes the following figure supplement for Figure 3:
Figure supplement 1. Monaural stimulation often leads to double events both in LSO and MSO.

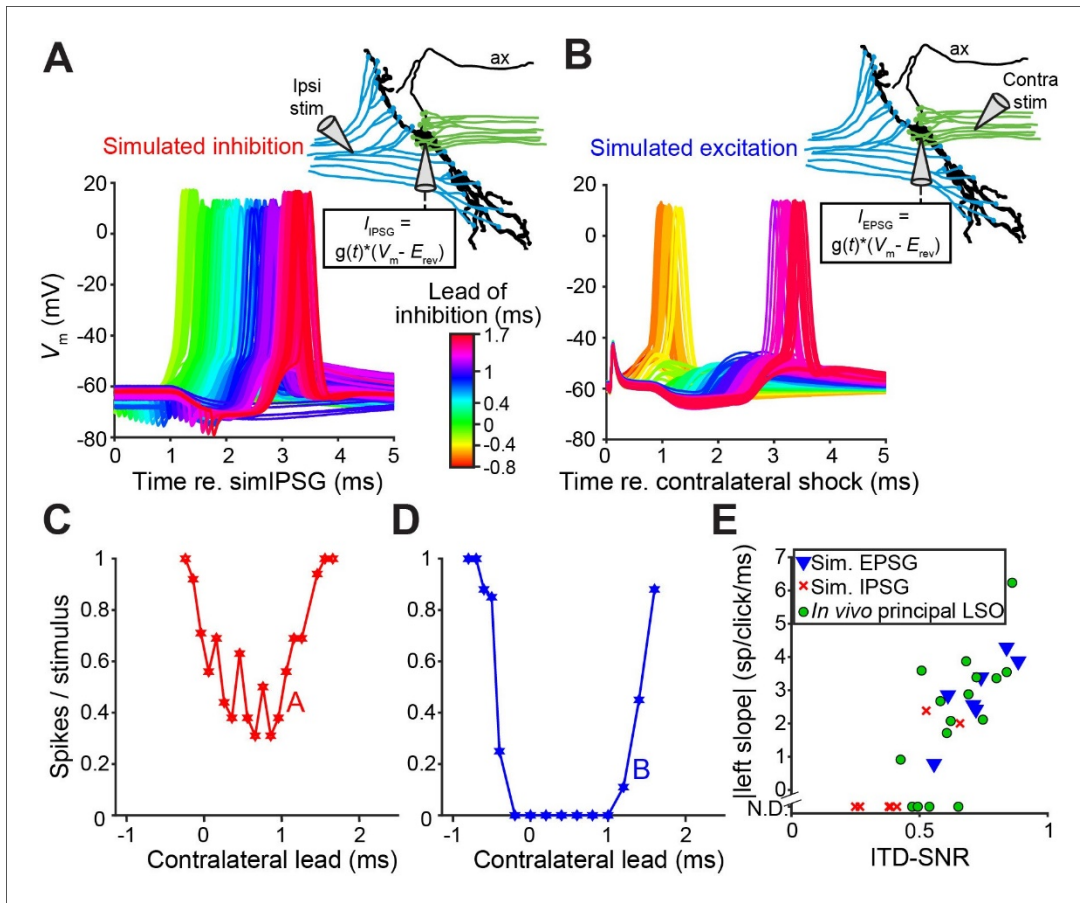


Figure 4.4. *In vitro* recordings reveal powerful inhibition for synaptically-evoked but not for simulated IPSPs.

(A) Voltage responses from a principal LSO neuron recorded in a brain slice, for which the ipsilateral inputs were activated by electric shocks and the contralateral input was simulated by somatically injecting inhibitory conductances (IPSG) via dynamic clamp. Inset indicates experimental setup. Delay between ipsilateral shock and IPSG was varied and is referenced to the timing of the simulated IPSG, and all recorded membrane potential traces are shown, color coded for the delay. ax: axon. (B) Similar to A, but with contralateral inputs activated by electric shocks and ipsilateral excitatory conductances simulated via somatic dynamic clamp (different neuron than A). (C) Rate delay function corresponding to the experiment in A. (D) Rate delay function corresponding to the experiment in B. (E) Steepness of the slope to the left of the trough for the population of delay functions (Figure 4 – figure supplement 1D and 1E, solid lines), plotted against the ITD-SNR (as in Figure 1L). Data from principal LSO cells recorded *in vivo* are shown for comparison (16 data sets from 7 cells). N.D.: not defined (slope was not defined when 20%

of maximal spike rate was not reached after smoothing (see Materials and Methods)). Numerical data represented as graphs in this figure are available in a source data file (Figure 4—Source data file 1).

The online version of this article includes the following figure supplement for Figure 4:
Figure supplement 1. *In vitro* recordings reveal powerful inhibition for synaptically-evoked but not for simulated IPSPs by current injection.

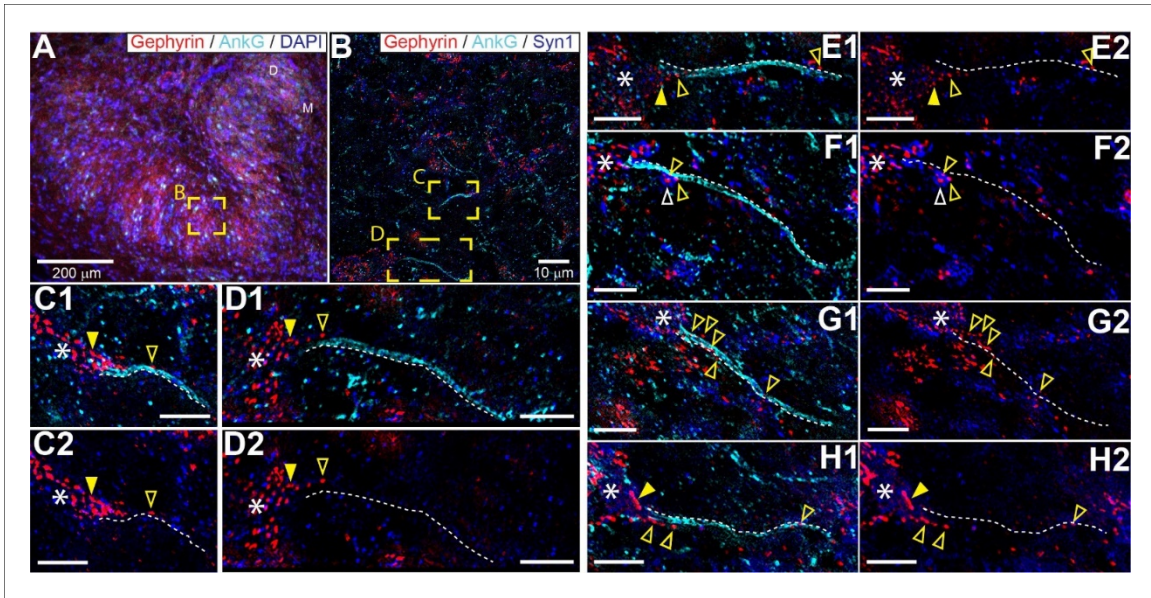


Figure 4.5. Glycinergic innervation of the axon initial segment of LSO neurons.

(A) An example of an LSO in a coronal tissue section from the Mongolian gerbil outlining subregions targeted for SR-SIM microscopy labeled with gephyrin (red), ankyrinG (cyan), and DAPI (blue). All imaging was targeted to the middle bend of the LSO. (B) An example SR-SIM multichannel image labeled for gephyrin (red), ankyrinG (cyan), and synaptophysin1 (blue). Yellow boxes indicate axon initial segments (AIS) shown in C (mirrored from B) and D. (C-H) Images showing example LSO AISs with (1) or without (2) labels for ankyrinG channel (cyan). White dotted lines lay adjacent to labeled AIS for visual guidance, but are not quantitatively drawn. Putative inhibitory terminals can be seen closely associated with the AIS (open yellow arrowheads) and axon hillock (filled yellow arrowheads). Some large putative gephyrin positive terminals show colocalization with synaptophysin1 labeling (open white arrowheads). White asterisks indicate the soma/dendrite from which the AIS emerges. All scale bars are 5 μ m, unless noted otherwise.

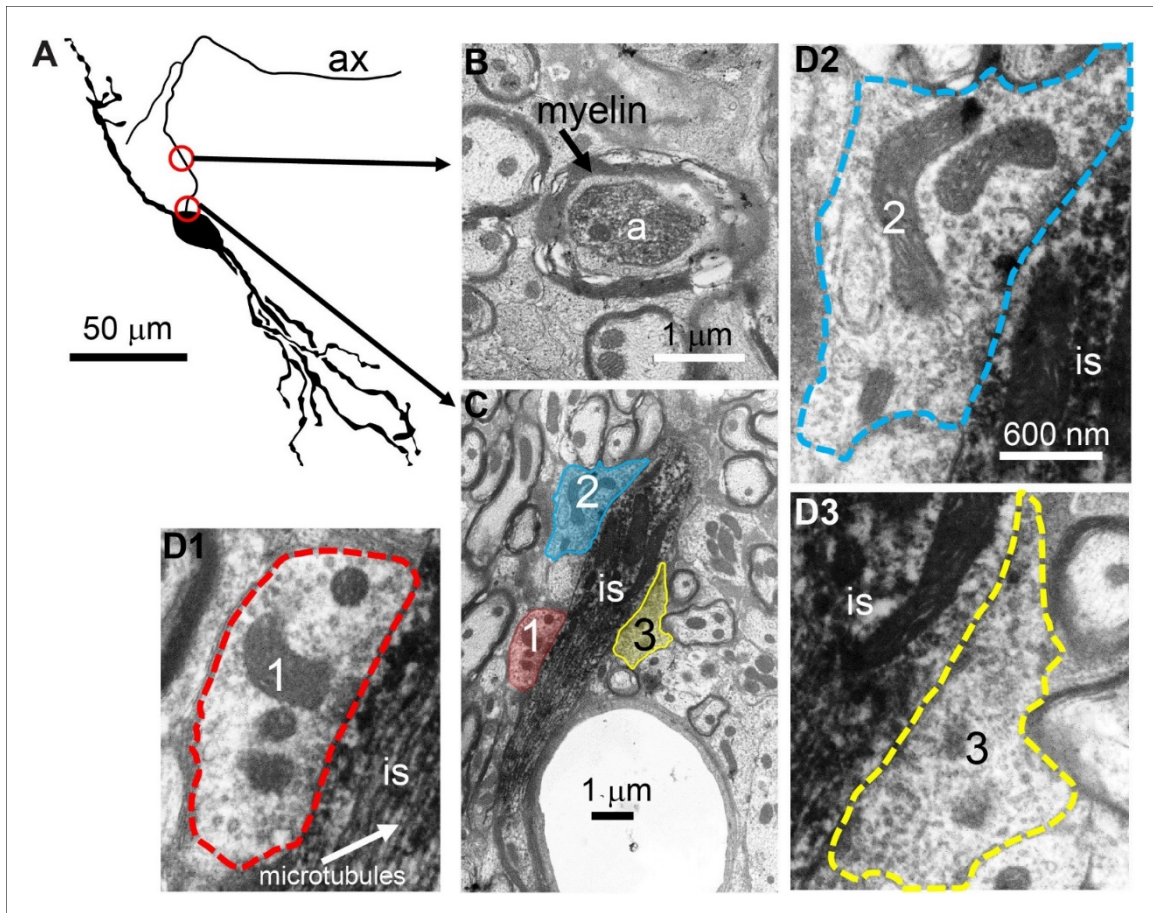


Figure 4.6. Electron microscopy reveals synaptic terminals on an LSO principal cell's axon initial segment.

(A) Camera lucida drawing of an LSO principal cell that was intracellularly recorded from and labeled, *in vivo*. This cell corresponds to cell 2 in (Franken et al., 2018, their Figure 2A). Arrows point to electron micrographs that show portions of the axon (ax) enclosed by the red circles. (B) Electron micrograph showing portion of the axon in the top circle in A. The axon is myelinated here. (C) Electron micrograph showing portion of the axon in the bottom circle in A. This is at the level of the axon initial segment (is). Enclosed colored areas 1-3 represent axon terminals synapsing on the axon initial segment. (D1-D3) Electron micrographs showing larger versions of axon terminals 1-3 in C. Scale bar in D2 applies to all 3 enlarged micrographs.

The online version of this article includes the following figure supplement for Figure 6:
Figure supplement 1. Electron microscopy reveals synaptic terminals on the axon initial segment of principal LSO cells but not of principal MSO cells.

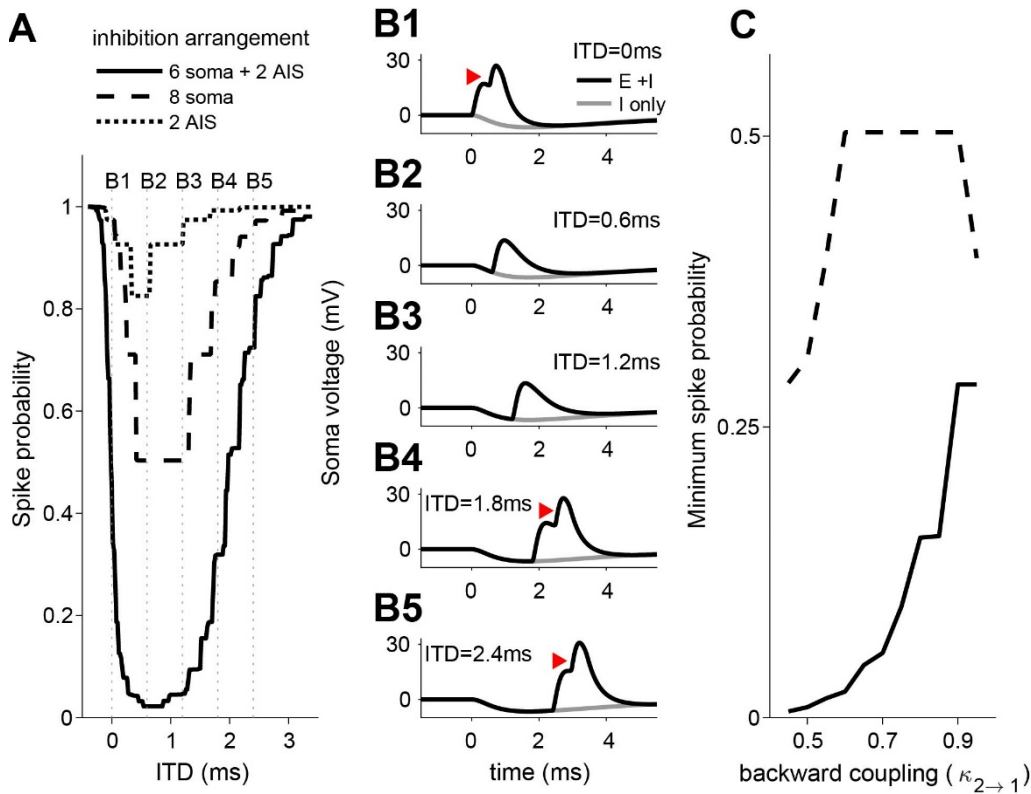


Figure 4.7. ITD-tuning in a two-compartment LSO neuron model.

(A) ITD-tuning is substantially deeper when inhibitory inputs target AIS as compared to the same total number of inputs targeting the soma only. (B) Soma voltage showing detailed timing of responses to excitatory and inhibitory inputs. All synaptic inputs are activated in these simulations. Inhibition arrangement is six soma and two AIS inputs. Coupling configuration in A and B is $\kappa_{1 \rightarrow 2} = 0.95$ and $\kappa_{2 \rightarrow 1} = 0.6$. Red arrowheads mark action potentials (backpropagated from initiation site in AIS compartment). (C) More pronounced suppression of spike rates when inhibitory synapses are added to the AIS rather than to the soma occurs for a range of backward coupling values. Inhibition arrangement for the two functions is indicated in the legend in A. Forward coupling in all simulations is $\kappa_{1 \rightarrow 2} = 0.95$. Numerical data represented as graphs in this figure are available in a source data file (Figure 7—source data file 1).

Figure supplement 1. Two-compartment LSO neuron model.

Figure supplement 2. ITD tuning in two-compartment LSO neuron model with synaptic kinetics adapted from Beiderbeck et al. (2018).

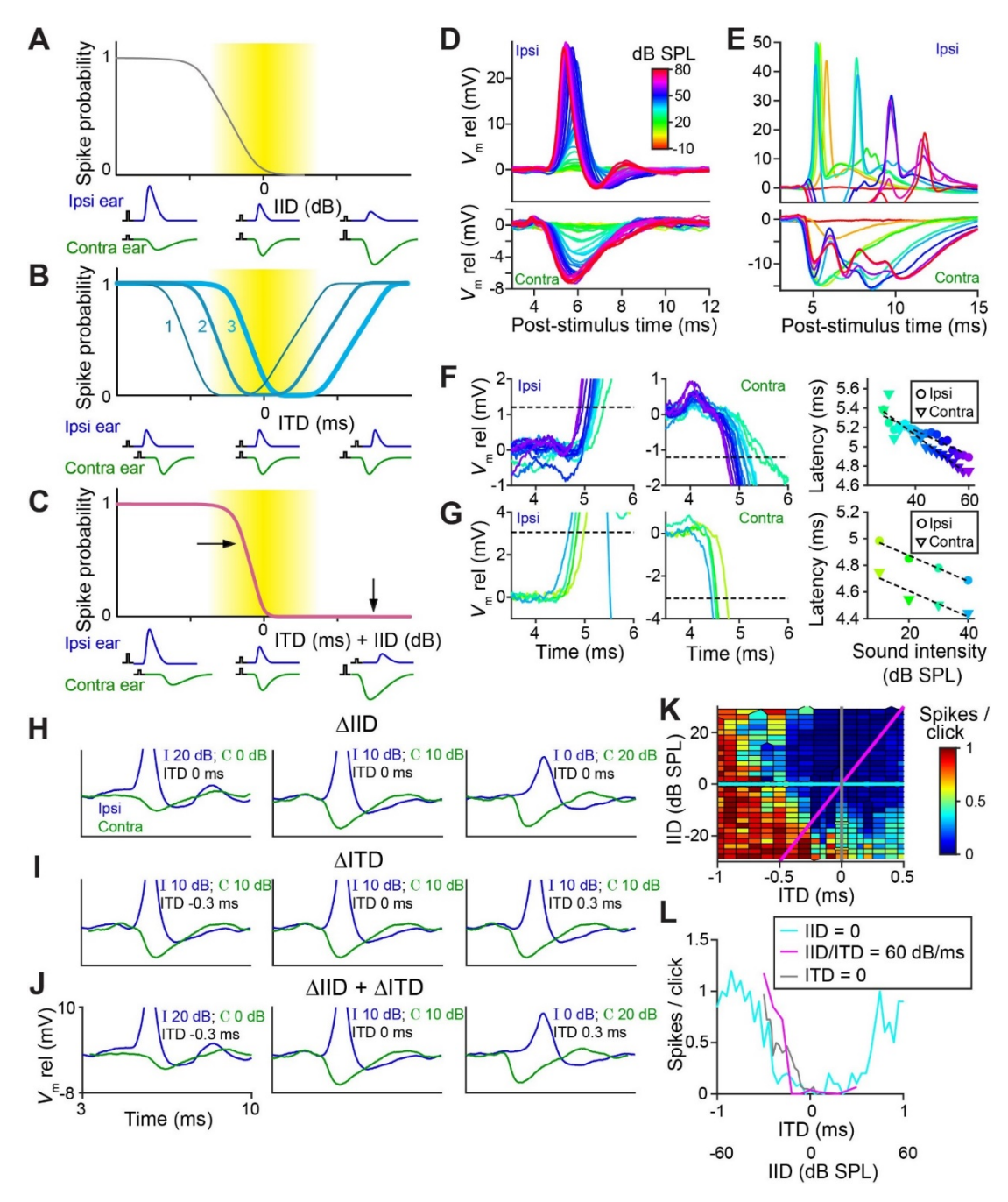


Figure 4.8. LSO neurons show graded latency-intensity changes which disambiguate spatial tuning.

(A) Cartoon showing change in spike probability for changing IID. Yellow area shows approximate region of physiological IID values. Traces below each plot represent the timing and amplitude of ipsi- and contralateral synaptic events to click-pairs with different IID values. (B) Cartoon showing change in spike probability for changing ITD, for three cases with different centering of the trough. (C) Cartoon showing change in spike probability for combined changes in ITD and IID. Horizontal and vertical arrows indicate effects of adding IID to ITD: a rightward shift in the left slope, and inhibition of the right shoulder of the tuning function. (D) Average responses to ipsilateral clicks (top panel) and contralateral clicks (bottom panel) of different sound levels for a principal LSO cell (CF = 12 kHz; same cell as Figure 2A). (E) Similar to D, for a non-principal (marginal) LSO cell (CF = 4.1 kHz; same cell as Figure 2B). Colors as in D. (F) Ipsilateral (left panel) and contralateral responses (middle panel) for the same principal LSO cell as in D. Colors correspond to sound levels, as in D. Dashed lines indicate the threshold used to calculate latencies, a voltage difference relative to rest with an absolute value of 20% of the average IPSP amplitude. For the ipsilateral ear, this voltage difference was depolarizing, for the contralateral ear, it was hyperpolarizing. For this analysis we used data from identical sound levels to ipsi and contra, i.e. the lowest sound level that leads to the maximal spike rate when presented to the ipsilateral ear. Right panel: latency values as a function of sound level, corresponding to the data in the left and middle panel. (G) Similar to F, for the same non-principal LSO cell as in E. (H) Averaged monaural responses to click pairs with different IIDs, for a principal cell (CF = 3.5 kHz). (I) Similar to H, but now ITD varies and IID is kept constant at 0 dB. (J) Similar to H and I, but for combined changes in ITD and IID. (K) Voronoi diagrams of spike rate for different ITD and IID combinations, for the same principal cell as in H-J. Colors are clipped between the limits shown in the color scale. Grey and cyan lines connect data points of respectively IID and ITD functions. Diagonal magenta line connects data points for which there is a consistent change in ITD and IID (60 dB change in IID per 1 ms change in ITD, which is realistic for this CF (Maki and Furukawa, 2005)). Data was pooled across different sound levels. (L) Grey, cyan and magenta functions show spike rates along the lines of the same color in K. Data from the same principal LSO cell as in H-K. Numerical data represented as graphs in this figure are available in a source data file (Figure 8—Source data file 1).

The online version of this article includes the following figure supplements for Figure 8:

Figure supplement 1. Individual traces corresponding to the mean data shown in Figure 8D and 8E.

Figure supplement 2. Similar as Figure 8K and 8L, for three additional LSO neurons.

Chapter 5: Regulated gene expression, not auditory activity, drives the development of sound localization neurons.

David B. Haimes^{1,2}, Holly S Stevenson, Natalie F Osterlund^{1,2}, and Nace L. Golding^{1,2*}

1. Department of Neuroscience, University of Texas at Austin, TX 78712
2. Center for Learning and Memory, University of Texas at Austin, TX 78712
3. GSAF

*To whom correspondence should be addressed

Corresponding author:

Nace L. Golding: University of Texas at Austin, Department of Neuroscience and Center for Learning and Memory, 1 University Station C7000, Austin TX 78712-0248, golding@austin.utexas.edu

Acknowledgements

This work was supported by NIH grants F31 DC017377 to D.B.H. and R01 DC006877 to N.L.G. The authors would like to thank the GSAF and Dr. Dennis Wylie for advice on sequencing experimental designs, as well as Drs. Elle Roberson and John Wallingford for their help in RNA isolation and use of their Nanodrop.

Author Contributions Statement

D.B.H. performed all experiments, data collection, and analysis of the resulting data. H.S.S. performed the library preparation and sequencing for Tag-Seq and Patch-Seq experiments. N.F.O. performed all animal care, experimental blinding, and helped analyze electrophysiological data. All figures were produced by D.B.H. and N.L.G., and D.B.H. wrote the manuscript text. All authors edited the manuscript.

Competing Interests Statement

The authors declare no competing interests.

ABSTRACT

Neurons in sensory circuits rely on accurate information processing of environmental cues to correctly inform behaviors and higher-order function. This processing transforms inputs into outputs and is determined by the intrinsic and filtering properties of neurons, which in turn are determined by their anatomical and physiological specializations. We use a well-described simple circuit that determines the spatial origin of sound, the Medial Superior Olive (MSO), to explore how changing intrinsic properties leads to specialization of informational output. This brainstem region, which hosts a heterogeneous population of neurons, can simultaneously integrate signals within sub-millisecond time windows, while also integrating activity over substantially longer timescales. Specifically, we asked whether intrinsic properties that are shaped over the course of development require auditory activity for specialization. Using a combination of electrophysiological and single-cell mRNA sequencing approaches, we found that diverse MSO neuron properties are only slightly modulated by auditory activity. Interestingly, the input-output processing of MSO neurons is shaped predominantly through changes in the transcriptome during development.

SIGNIFICANCE STATEMENT

Neurons of the medial superior olive (MSO) encode spatial cues by detecting both fast *microsecond* and much longer differences in the arrival time of inputs arising from the left and right ears. Previous work demonstrates that the MSO is a hotspot of anatomical, physiological, and synaptic specializations that aid in precise computation of sound localization cues. Here, we questioned how a diverse input-output relationship, driven by these unique specializations, arises – whether as a function of development or auditory activity. We find that although specializations in these cells develop after the onset of hearing, the neurons of the MSO are developmentally determined to become timing difference detectors. Interestingly, auditory activity plays no role in altering the transcriptome, and only a minor role in modulating the intrinsic properties of neurons. Therefore, we postulate that injury-based deafness models are more likely to experience positive therapeutic outcomes with cochlear implants and other prosthetics, given that the MSO and sound localization circuitry remains relatively intact.

INTRODUCTION

Neurons in different areas of the brain process, filter, and integrate incoming signals to provide output in the form of different patterns of action potentials that reflect features of input stimuli. To carry out their varied roles, neurons exhibit specializations in morphology as well as in protein expression, such as voltage-gated ion channels, which together directly alter the ways a neuron transforms information. For sensory systems in particular, accurate interpretation of environmental cues is paramount to properly dictate behavioral responses. The sound localization circuitry in the mammalian medial superior olive (MSO) provides one of the most striking examples in the nervous system where precise intrinsic properties dictate neuronal output. In maturity, MSO neurons detect spatial locations based on the coincident arrival of excitatory inputs (interaural time difference – ITD) driven by sounds to the left and right ears, a process that is carried out with a temporal resolution of tens of microseconds (Brand et al., 2002; Goldberg & Brown, 1969; Spitzer & Semple, 1995; Yin & Chan, 1990). This mapping of auditory space through sound localization is crucial for a myriad higher order processing, such as aiding in the early development of language acquisition or attending to specific signals in a noisy environment (Arons, 1992; Litovsky & Gordon, 2016; Pollack & Pickett, 1957; van Hoesel & Tyler, 2003).

This remarkable spatial acuity is an emergent property following the onset of hearing, as some species of mammals are born deaf, and continues developing throughout neonatal and juvenile ages (Ashmead et al., 1991; Kelly et al., 1987). Within the MSO, perceptual changes in precise spatial acuity are linked to the coordinated alteration of the spatial distribution of inhibitory synapses (Kapfer et al., 2002; Werthat et al., 2008), an increase in the kinetics of synaptic currents (Magnusson et al., 2005) as well as changes in neurotransmitter composition (Gillespie et al., 2005). Additionally, these synaptic changes

are closely accompanied by profound changes in intrinsic electrical properties, namely a decrease in input resistance and membrane time constant (Chirila et al., 2007; Scott et al., 2005). Finally, an increase in the density and modulation of low voltage-activated potassium and hyperpolarization-activated cyclic nucleotide-gated (HCN) cation channels results in larger currents, which ultimately play critical roles in sharpening temporal precision and spatial acuity (Mathews et al., 2010; Scott et al., 2005).

More recently, we have shown that MSO neurons display a broad continuum of subthreshold membrane properties and firing patterns which can be observed in early juvenile development (~P17) and persist through sexual maturity (Bondy et al., 2021). The stereotyped synaptic inputs described above generates a continuum of firing output responses, which range from a single, small amplitude spike (dubbed “phasic” here) to large amplitude, repetitive trains of spikes (dubbed “repetitive” here). This continuum of firing responses may be important for providing information to downstream brain regions about not just incredibly fast ITDs, but also much slower signals, such as slow amplitude-modulated envelope components of sound. For phasic neurons that have incredible temporal precision, all of the intrinsic property changes described above apply. However, it remains to be seen whether these same changes apply equally to the entire firing continuum, or if different mechanisms exist to generate diversity, particularly for neurons that fire repetitively.

Alongside changing emergent properties, many studies demonstrate the importance of auditory activity, or lack thereof, in shaping both intrinsic neural properties and the overall circuit map for the MSO. Studies on models of hearing loss and deafness reveal a multitude of compensatory changes, including the size of tonotopic lamina (Kandler et al., 2009), synapse connectivity and size (Hardie & Shepherd, 1999; O’Neil et al., 2011; Rubel & Fritzsche, 2002; Ryugo, 2015), and overall dendritic morphology (Russell & Moore, 1999). Conversely, studies using noise enrichment (Macica et al., 2003; Song et al., 2005) provide evidence that post-translational states of voltage-gated ion channels can be modulated. Furthermore, for animals reared in omni-directional noise, effectively eliminating the ITD cues the MSO relies upon, neurons are remarkably resilient, and still

able to integrate ITDs, albeit with diminished precision (Seidl & Grothe, 2005). It remains an outstanding question how auditory activity and development coincide to shape the diversity of firing patterns that emerge in post-hearing MSO neurons.

In this paper, we determine the roles of development and auditory activity on the emergence of firing diversity within the MSO. Using a novel combination of electrophysiological, single-cell sequencing, and surgical techniques, we show that major changes in the transcriptome of MSO neurons occur during neonatal and early juvenile development, switching from a pre-hearing MSO to a heterogeneous post-hearing MSO. Despite the complete loss of auditory activity, the transcriptome and overall range of firing diversity of MSO neurons is generally unchanged in our deafened animals. Surprisingly, auditory activity acts only to fine-tune the overall precision, excitability, and distribution of heterogeneous MSO neurons, likely through post-translational mechanisms, but does not stop MSO cells from being fated to become coincidence detectors.

RESULTS

Auditory activity is not required for the emergence of firing diversity in the MSO.

To assess how the input/output relationship of MSO neurons changes after hearing onset, we performed whole-cell current clamp recordings from Mongolian gerbils on postnatal day 10 (P10) and P18-30. Strikingly, there is minimal diversity in the firing type of prehearing neurons, and consistent with our past study (Bondy et al., 2021) diversity does emerge after hearing onset (**Figure 5.1A-B**). As a function of development, action potential width narrows (**Figure 5.1C,D,E**) and passive properties drastically decrease (membrane resistance decreases - Wilcoxon, $p=5.8e-16$). Interestingly, while passive properties undergo a developmental decrease, firing frequency does not change unidirectionally, but rather generates a continuum of response firing frequencies, including firing at much higher rates than prehearing levels (**Figure 5.1E – Firing Frequency**). This diversity of firing is functionally relevant, as high firing frequency phenotypes are better

suites to responding to slow envelope stimuli, while transient, single firing neurons respond best to fast fine-structure components of sound stimuli (**Figure 5.1F**, (Bondy et al., 2021)). This emergence of diverse firing outputs led to questioning what driving factors - normal development, auditory activity, or a combination – might explain the differences seen here.

To determine the effects of normal development and hearing status on MSO firing heterogeneity, we generated 4 cohorts of Mongolian gerbils (**See Methods for Details, Figure 5.2A**). To determine the effectiveness of the surgical interventions, gerbils (P22-47) were later tested for auditory brainstem response (ABR) thresholds, a general measure of hearing activity (**Figure 5.2B**). To test for frequency-dependent effects of the surgery, we tested using a variety of stimulus intensity/frequency combinations, as well as with broadband clicks (**Methods**). As expected, there were significantly elevated response thresholds in the Cochlear Ablation Juvenile (DEAF) cohort. While both Surgical Sham Juvenile (SHAM), and Post-hearing Juvenile (POST) animals exhibit some frequency dependent increases in threshold at higher frequencies, they were not significantly different from each other.

To assess how firing phenotypes changed across cohorts, we performed whole-cell current-clamp recordings in acute brain slices. We injected a series of square current steps increasing in amplitude until neurons began to fire an AP (threshold), and then fired maximally (**Figure 5.3A**). Responses were defined as “phasic” (**Figure 5.3B**) or “repetitive” (**Figure 5.3C**) based on whether the cell fired a single AP or multiple APs in response to *any* square current steps. The Pre-hearing (PRE) cohort only exhibited the repetitive firing type, while the remaining three groups each showed the presence of both firing response types (**Figure 5.3D-E**: PRE: n=29/31 (2 excluded due to incomplete FI), neonatal ages P10-11; POST: n=73/73; SHAM: n=41/41; DEAF: n=61/61, juvenile ages P23-61). Example traces shown are responses at threshold, and at the maximal firing response (or the highest current injection for phasic neurons). By quantifying the number of APs (shown in log scale) in response to increasing current injection (**Figure 5.3D-E**), we found that regardless of how much current was injected into phasic cells, sometimes as

high as 10nA, these cells would never fire a second spike. Interestingly, repetitive firing cells often fired early onset bursts of action potentials at just suprathreshold injection intensities, particularly in the DEAF cohort (arrow **Figure 5.3D**, and **Figure 5.3F**). Further increases in stimulation led to more consistent, repetitive firing throughout the stimulus duration (see maximal firing responses – **Figure 5.3C**). While the continuum of firing diversity in all three juvenile cohorts emerged, we found changes in the proportion of repetitive to phasic neurons. The SHAM and POST cohorts were similarly biased towards phasic firing types (POST: 84.9% phasic, 15.1% repetitive; SHAM: 92.7% phasic, 7.3% repetitive). In contrast, the DEAF cohort exhibited a higher percentage of repetitive firing types compared to controls (DEAF: 63.9% phasic, 36.1% repetitive) (**Figure 5.3E**). Notably, the increase in the repetitive phenotype for Cochlear Ablation Juveniles was with neurons that fired bursts of action potentials at just suprathreshold stimuli, but often would not fire throughout the entire duration of the stimulus, even at maximal current injections (**Figure 5.3F**).

We further asked how individual action potentials (APs) were changing in response to either the developmental axis or complete hearing loss. Therefore, we assessed AP parameters for the first spike generated at threshold for each group (**Figure 5.4**). For cells that fired repetitively at threshold, we took the first spike generated. Notably, the spike waveform was dramatically different for neonatal and juvenile neurons (**Figure 5.4A-B**). Interestingly, the DEAF cohort neurons showed remarkably few changes in the population of spike waveforms compared to POST and SHAM: the spikes responded to the onset of the current injection with a similar absolute threshold (**Figure 5.4B,D**), and similar halfwidth (data not shown). To further analyze changes to spike shape, we generated phase plane plots by taking the first derivative of voltage plotted against the voltage for each threshold spike (**Figure 5.4C**). From these plots, we were able to compare several metrics such as spike threshold, spike amplitude, and maximum depolarization rate of the spike (**Figure 5.4D-F**). We find that for threshold, PRE cohort responses were significantly depolarized, compared to all juvenile responses (**Figure 5.4D**). Furthermore, the responses from the DEAF cohort were also depolarized relative to the POST and SHAM cohorts,

although the latter two were not significantly different from each other (**Figure 5.4D**). We found a similar trend for spike amplitude (**Figure 5.4E**). Interestingly, however, maximum depolarization rate exhibited a slightly different pattern (**Figure 5.4F**). While both PRE and DEAF cohorts were elevated relative to controls, DEAF cohort neurons exhibited faster rates of rise than even their prehearing counterparts, although the populations were not significantly different. We were intrigued to see that although firing diversity still emerged, active spiking parameters change in the DEAF cohort, sometimes measuring remarkably close to PRE levels. Therefore, we asked whether these changes might be controlled upstream, at the genetic level.

Development, not auditory activity drives gene expression in the MSO.

How development and auditory activity act in concert to drive gene expression changes in the MSO remains an open question. As the electrophysiological data implied underlying differences in ion channel proteins (**Figure 5.4D-F**), particularly given that DEAF measurements were similar to PRE, we asked whether gene expression patterns were also similar across cohorts. To determine what gene expression changes may arise, we performed 3' RNA sequencing on mRNA harvested from isolated MSOs from each experimental cohort. After isolation, library prep and sequencing, 21,732 genes were assessed for differential expression across hearing modalities (**Figure 5.5A**). Strong separation emerged between PRE and all other cohorts (**Figure 5.5B**) when visualized with a principal component analysis. Principal component one (71% variance), separated all three biological PRE replicates from all juvenile replicate, and no distinguishable pattern was seen among the three juvenile cohorts (**Figure 5.5B**). Additionally, when total gene expression changes were assessed between the PRE and POST cohorts (**Figure 5.5C**), a total of 3004 genes were significantly different (Benjamini-Hochberg adjusted p value < 0.1, Upregulated = 1607 genes, Downregulated = 1397 genes, greater than log₂ fold change). While a total of 3295 genes were differentially expressed between the DEAF and PRE cohorts (**Figure 5.5D**: Upregulated = 1731 genes, Downregulated = 1564 genes), when the DEAF cohort was further compared against the SHAM cohort (**Figure 5.5F**), only 30 genes were significantly different. Furthermore, comparison of the SHAM and

POST cohort exhibited only 1 gene downregulated with a significant log₂ fold change (**Figure 5.5E**). This suggests to us that auditory activity does not drive gene expression changes during development and maturation of the MSO.

Ion channel expression is strongly controlled during MSO development.

To further investigate the transcriptomic differences between neonate and juvenile cohorts, the 3004 genes that were significantly differentially expressed were independently run through Gene Ontology (GO) analyses using PANTHER (v 16.0) (**Figure 5.6A**). As the electrophysiological data revealed differences in parameters like spike amplitude and maximum depolarization rate across cohorts, which are parameters commonly associated with voltage-gated sodium ion channel proteins, we tested whether GO term analyses would demonstrate significant changes in ion channel regulatory pathway changes. Specific GO terms are highlighted in green, and strongly suggest that ion channels, as well as proteins associated with ion channel regulatory pathways, are significantly upregulated (**Figure 5.6B**). GO terms including RNA translation/ribosomal proteins and transcription factors are downregulated, implying a potential switch in transcriptional regulation as the animals mature (**Figure 5.6C**). Together, these terms support a hypothesis that translational and post-translational mechanisms underlie a developmental switch in gene expression and protein regulation. While GO terms generalize the broad gene expression changes that occur, we wanted to take a more granular view on shifts in ion channel expression during development, given the electrophysiological changes in our recordings (**Figures 5.1, 5.3, 5.4**). We found that several ion channels change bidirectionally during development (Figure 6D). For example, *Scn2a* and *3a* are highly expressed in the neonate compared to the juvenile. In contrast, several other ion channels (*Scn4b*, *Scn8a*, *Kcna1*) are highly expressed in the juvenile compared to the neonate. In conclusion, our data support that a developmental switch in gene expression and potentially regulatory pathways is present, but moreover, given the transcriptome is unchanged in the DEAF cohort, that temporal precision is fine-tuned through further regulatory mechanisms.

Patch-seq cannot cleanly divide POST MSO neurons by their firing type

A major limitation to the 3' RNA sequencing dataset is bulk sequencing of the entire nuclei, where single cell differences (phasic vs. repetitive firing types) are diluted. Because of this averaging of expression, we were unable to determine whether POST repetitive neurons resemble PRE repetitive neurons, or if the POST neuronal diversity has a clear developmental lineage from PRE neurons. Specifically, we hypothesized that PRE neurons might be developmentally retained to provide the repetitive phenotype in the juvenile MSO. To address this, we performed Patch-Seq, a combination of electrophysiological recording with subsequent mRNA harvesting of the same cell to compare these three firing states (**Figure 5.7A**). We performed a UMAP (Uniform Manifold Approximation and Projection) analysis, overlaying the cohort information to categorize our data points as either prehearing (PRE) or posthearing (POST) (**Figure 5.7B**), which revealed two transcriptionally distinct populations (**Figure 5.5-5.6**). To address whether the three firing states - PRE Repetitive vs POST Phasic vs POST Repetitive - represent a developmental progression of cell types, we further overlaid this firing type information over the same UMAP analysis. Furthermore, we performed pseudotime analysis (**Figure 5.7C – black line represents pseudotime**), which revealed a trajectory that began with our prehearing neurons and ended in post-hearing neurons. As we tested other pseudotime analysis packages (Monocle3 **Figure 5.7C**; Slingshot, **Figure 5.7 Supplemental**), trajectories either progressed sequentially from PRE, to POST phasic, to POST repetitive, or alternatively, bifurcated after PRE, into a mixture of POST firing types (**Figure 5.7 Supplemental**). These analyses show that that repetitive posthearing neurons are not a retained, undifferentiated prehearing neuron; instead, they are transcriptionally distinct from the pre-hearing neuron and display a matured transcriptional program similar to phasic neurons.

We wanted to further investigate the transcriptional differences and similarities between these three firing states, so we visualized the most highly variable genes in the dataset (**Figure 5.7D**). The resulting heatmap showed clear differences between PRE and POST neurons, with genes clearly differentially enriched along this developmental axis. While our pseudo-time analysis showed that POST repetitive neurons are more similar to

POST phasic neurons compared to PRE neurons, we wanted to look more granularly at two specific genes, *Pvalb* and *Scn3a*, and their enrichment in these three firing states. *Pvalb* is a known neural marker, and often utilized as a cell-type classifier for neurons (Lohmann And B C M & Friauf, 1996), while *Scn3a* is canonically studied as an embryonic sodium channel gene (Deng et al., 2011; Gazina et al., 2010; Plummer & Meisler, 1999). In the rat, previous evidence demonstrates that *Pvalb* increases across the developmental axis: prehearing MSOs display low *Pvalb* staining, while mature MSOs exhibit robust staining (Lohmann And B C M & Friauf, 1996). Therefore, we used *Pvalb* as a marker for mature MSO neurons, to specifically determine if it is equally expressed in both repetitive and phasic neurons. Using our dataset, we were able to ask if *Pvalb* expression was high in POST repetitive neurons, similar to what we would expect for POST phasic neurons, or low, similar to what we would expect for PRE neurons. Mapping *Pvalb* and *Scn3a* expression to our UMAP space exhibited a strong split, with *Pvalb* remarkably enriched in nearly all POST neurons (**Figure 5.7D**). In contrast, *Scn3a* showed the opposite pattern and is enriched in PRE neurons (**Figure 5.7D**). These data further support our pseudo-time results, and show that POST repetitive neurons, with strong upregulation of *Pvalb* transcripts, are a mature, likely differentiated, neuron as opposed to a developmentally retained PRE neuron.

We were curious if other voltage-gated ion channels also undergo a developmental switch, explaining the underlying physiological differences between the three firing types. Using a list of general voltage-gated ion channels from the HGNC database (<https://www.genenames.org/data/genegroup/#!/group/178>), parsed by genes annotated in the gerbil genome (~180 genes), we utilized a supervised machine-learning decision tree to model and classify our data based on POST phasic, POST repetitive, and PRE repetitive (**Figure 5.8A**). Using an 80-20 training-test split, we found our modeling often separated PRE neurons early and robustly in the decision tree-branching. The model struggled, however, using multiple branches and many binary decision calls to separate POST phasic and repetitive neurons. As the inability of the machine-learning algorithm to separate POST phasic from POST repetitive might be due to the randomness of the data partitioning, we

utilized a random Forest model to increase our modeling robustness. This methodology averages the classification algorithms utilized across 500 decision trees and generated an overall model prediction accuracy generally around ~90% (with an out-of-box error rate of ~15%). From our random forest modeling, we analyzed the genes most impactful on model prediction accuracy (**Figure 5.8B**). To confirm strong differences in expression patterning, we displayed the normalized expression levels of the top three most impactful genes (**Figure 5.8C** – *Scn4b*, *Kcnq4*, *Scn1b*). Finally, we further utilized our random forest model to determine if there were cell class specific errors in prediction accuracy (**Figure 5.8D**). Indeed, we saw that our model, utilizing only a curated list of ion channel genes, was very good at predicting POST phasic neurons (~2% class error), relatively good at predicting PRE neurons (~11% class error), and very poor at predicting POST repetitive neurons (~45% class error). Interestingly, when the algorithm mis-classified POST repetitive neurons, it often mistook them for POST phasic neurons. These data further emphasize that the transcriptome of POST phasic and POST repetitive neurons are highly similar and one principal cell type, despite clear physiological differences in firing phenotype and action potential parameters. We postulate that post-translational pathways are integral to defining this continuum of intrinsic properties.

DISCUSSION

Here, we have assessed how auditory activity, combined with a transcriptome that changes significantly over a short, critical period of developmental time, function together to alter intrinsic properties of MSO neurons. The MSO, which our previous work demonstrates has a spectrum of heterogeneous response properties to binaural signals (Bondy et al., 2021), consists of a simple circuit with a stereotyped functional role: detecting microsecond ITDs, as well as slow envelope ITDs. While previous work demonstrates that passive membrane properties, along with voltage-gated potassium channels, undergo significant changes after hearing onset in the Mongolian gerbil, it remains unclear whether these trends occurred for all MSO neurons equally, and whether transcriptional fluctuations were drivers of these changes.

Using a bilateral cochlear ablation model of severe hearing loss induced prior to hearing onset, we attempted to decouple the impact of auditory activity and normal transcriptional developmental trajectories in MSO neurons. Surprisingly, we found that the MSO remained a diverse nucleus in DEAF models where severe hearing loss was confirmed by ABR testing. Neurons that fired transiently (phasic), as well as repetitively, were both sampled in DEAF, but in different proportions compared to SHAM and POST cohorts. DEAF phasic neurons were predominantly affected in AP shape parameters, as their action potentials were notably larger and faster. For the DEAF repetitive firing neurons, however, physiological properties were more consistent with our recently published work in animals with normal hearing (Bondy et al., 2021). It is striking that MSO neurons, in the absence of normal auditory activity, still exhibit a large range of firing diversity and remain primed to perform diverse ITD detection. The compensatory changes seen here follow from previous studies, such as those in the barn owl, which demonstrate that developmental age, and not auditory experience is a strong driver in developing sound localization accuracy in behavioral tasks (Knudsen 1984, Knudsen 1986).

In this study, we assessed whether the transcriptome of MSO neurons changed as a function of both age, but also in response to auditory activity. Our data supports the hypothesis that the onset of auditory activity does not alter the transcriptome of the MSO. Here, major shifts in the transcriptome occurred over normal development, before and after the onset of hearing, similar to changes seen by Ehmann et al. (2013). Their data, taken from the broader rat superior olive complex nuclei, of which the MSO is a part, demonstrates clearly that specific genes are tightly regulated during this critical juncture from pre- to post-hearing. Our work goes a step further by discretely targeting the MSO, and utilizes RNA-sequencing, rather than microarrays, to globally demonstrate a major change to the transcriptome due solely to development and not hearing loss.

While deafening did not alter the transcriptome, we did identify electrophysiological differences in the cochlear ablation model, including the proportion of firing phenotypes, as well as active firing parameters in the phasic population. From this evidence, we hypothesize that compensatory changes in response to auditory activity act

through post-translation mechanisms. Previous studies show that the phosphorylation states of potassium channels change based on an animal's auditory environment (Macica et al., 2003; Song et al., 2005). Here, the electrophysiological changes that we see primarily relate to spike size and shape, which could be a potential result of the same mechanism. However, a vast number of regulatory pathways for ion channels are known including, but not limited to, subunit pairing, modification state, stability and degradation mechanisms, insertion mechanisms, or channel trafficking mechanisms (Armstrong & Hille, 1998; Lai & Jan, 2006; Mourot et al., 2012; Puri, 2020; Yu & Catterall, 2003), any number of which might be directly altered in response to changes in auditory activity. Furthermore, work done by proteomics labs demonstrate that global RNA abundance correlates positively with final protein abundances, but only explains ~40-60% of the variability, and suggests that these same stability, degradation, and modification pathways of both mRNA and protein all strongly contribute to controlling the final levels of expressed protein (Vogel et al., 2010; Vogel & Marcotte, 2012) . Our GO term analysis presented here specifically implicates several pathways that may be key to unraveling how the electrical properties of MSO neurons are shaped. Together, the evidence presented here suggests to us that post-translational activity is a hotspot both for refining initial firing diversity, but also as a potentially direct target of auditory activity.

It is interesting to speculate whether this driving axis of development also has a critical period. Studies show that prior to hearing onset, central neurons exhibit spontaneous bursts of action potential firing driven by hair cells in the cochlea (Lippe, 1994; Tritsch et al., 2007), which propagate in waves throughout the central auditory pathways (Babola et al., 2018; Di Guilmi & Rodríguez-Contreras, 2021) and as in other sensory modalities, coordinates axonal refinement and the establishment of topographic maps of frequency (Babola et al., 2018; Clause et al., 2014). In contrast to our experiments here, where we removed auditory activity, a fascinating line of research would be to alter this spontaneous activity through Vglut3 animal models (Akil et al., 2012; Babola et al., 2018). In Vglut3 knockout models, spiral ganglion neurons exhibit marked increases in excitability, and we question how this upstream increase in activity may in turn impact the

shifts in the MSO transcriptome seen here. These experiments would provide evidence whether a critical period for gene expression exists in the MSO. Moreover, we wonder whether models that abolish or otherwise alter these early spontaneous waves of activity, might have a substantial impact on firing heterogeneity – or put simply, does early spontaneous activity notify the MSO transcriptome to shift from a pre- to post- hearing state, and through what regulatory mechanisms?

Our use of Patch-seq allowed us to simultaneously use bioinformatics and electrophysiology to study a single cell type with diverse properties in time. Specifically, we questioned whether POST repetitive neurons were an undifferentiated precursor neuron, which had yet to undergo developmental changes. While we were able to separate PRE and POST neurons based on their transcriptional differences, we were unable to cleanly separate POST phasic and repetitive neurons, despite the use of numerous techniques, including pseudotime analysis, highly variable gene analysis, machine-learning classification, and transcript expression of known developmental markers such as *Pvalb* (Lohmann And B C M & Friauf, 1996). This further emphasizes to us, in combination with our previous electrophysiological and anatomical investigations (Bondy et al., 2021), that the MSO is composed of a single principal neuron type, which is further diversified by a spectrum of response properties. In this study, it was impossible to discretely separate MSO neurons by firing type from a transcriptomic perspective, and therefore we hypothesize that developmental changes to the transcriptome set up a continuum of firing properties, that are then modulated by post-translational mechanisms. We particularly were intrigued that these post-translational mechanisms act in a bidirectional way. Given that active electrophysiological parameters (spike amplitude, etc.) for POST repetitive were *higher* than PRE, and POST phasic were *lower* than PRE, it is possible post-translational machinery acts through two separate pathways, generating bidirectional changes in excitability.

Furthermore, in agreement with our past work (S. Khurana et al., 2011; Sukant Khurana et al., 2012; Scott et al., 2005), passive properties such as input resistance and time constant generally decrease over the course of post-hearing development, including

the previously undescribed changes for repetitive neurons. Additionally, repetitive neurons also undergo similar changes to threshold as phasic neurons, a parameter more closely linked to the axon initial segment, where spike generation occurs (Royeck et al., 2008). The major divergence along this firing type axis in the POST is in active spiking parameters. Moreover, there are equivalent changes in sodium channel gene expression, such as *Scn4b* and *Scn8a*, both of which have been implicated in resurgent currents (Bant and Raman 2010) or burst firing in other brain regions (Swensen and Bean 2005). Given this cumulation of evidence, we hypothesize that post-translation modifications to these proteins might act primarily to generate a diversity of firing phenotypes.

We think these findings are important, as the MSO acts as a neural substrate for sound localization, and despite nearly complete hearing loss, remains mostly intact in terms of its intrinsic, diverse properties. Therefore, the MSO is potentially a prime candidate for external interventions in cases of human hearing loss (Ryugo, 2015). However, it is unclear from our current data what the long-term impact of lacking auditory activity is on the MSO; it remains to be seen whether the MSO maintains diverse firing properties long after insult. Therefore, future work investigating critical periods of gene expression in VGlut3 knockout models, as well as modulating the duration of auditory deprivation will together provide evidence about the resilience of heterogeneity in the MSO. Based on evidence that cochlear implant patients with congenital deafness struggle with ITD detection-based tasks (Hancock et al., 2010) demonstrates that current intervention strategies are biased towards success for insult-based hearing loss, supported by the data here that the MSO is remarkably resilient to bilateral cochlear ablation. However, understanding how exactly intrinsic properties are shaped in congenital models of deafness, and what critical periods shape response property resilience will be crucial to making advances in auditory prosthetics and treatments.

ONLINE METHODS

Materials and Methods

Gerbils. All procedures were conducted in accordance with the Institutional Animal Care and Use Committee at The University of Texas at Austin, following guidelines of the National Institutes of Health. Mongolian gerbils (*Meriones unguiculatus*) were raised in a colony at the UT-Austin Animal Resource Center and maintained on a 50/50 day/night cycle with continual access to food and water.

Four cohorts of gerbils were generated to assess how development and auditory activity impact MSO neural diversity. The first, prehearing neonate (abbreviated PRE, P10), provided an early developmental timepoint for comparison prior to the onset of hearing (P11-12 roughly). To study the effects of hearing loss, three cohorts were generated through surgical intervention (performed at P10), by performing a cochlear ablation (Cochlear Ablation Juvenile – abbreviated DEAF), a sham surgery (Surgical Sham Juvenile – abbreviated SHAM), or non-surgical litter weight control (Posthearing Juvenile – abbreviated POST).

Cochlear Ablation Surgeries. Surgical interventions were made at postnatal day 10 (P10), just prior to hearing onset. A litter of pups was separated from parents and kept in isolated housing in a surgical suite for the duration of the surgical day. Individual surgeries began with anesthesia administered using 5% Isoflurane in O₂ administered via inhalation in a closed chamber. Pups were then relocated underneath a dissection scope, with IR heating to maintain body temperature, with continual administration of Isoflurane in O₂ to maintain proper anesthetic depth measured by toe pinch and proper breathing (reassessed every 15 minutes). Lidocaine and iodine were topically applied posterior to the pinna, where an incision was made. Access to the inner ear space was located, where cochlear ablations were performed using forceps to surgically remove and identify the ossicles, using care to avoid the stapedial artery. Further, structural damage was applied to the cochlea, using a glass pipette connected to suction to visualize removal of the endolymph, ensuring hair cell degradation. When possible, the basilar membrane was also extracted through the same suction pipette, or forceps. A small ball of degradable surgical foam was then placed in the inner space, and the incision was closed using forceps to hold the wound closed and applying a small amount of superglue on the exterior of the wound. Animals

were then given a temporary tattoo in the paw pad to maintain identification. The exterior wound was then treated with a mixture of lidocaine and neomycin to aid the healing process. Surgical sham animals underwent the same incision, localization of the inner ear space, but the ossicles and cochlea were left intact before wound closure. Non-surgical controls received the same exterior lidocaine/neomycin mixture applied posterior to the pinna, but did not receive an incision, or damage to the ossicles/cochlea.

Post-Surgical Recovery. All animals, including cochlear ablation, surgical sham, and non-surgical controls were handled and treated the same throughout the surgical process. Animals were all weighed for pre-, peri-, and post-operative weights to assess any deviations in development that may occur due to metabolic reasons. Starting the first day and every day for the first three days after surgery, all pups received carprofen (5mg/kg body weight) sub-cutaneous, along with further lidocaine/neomycin topically at the surgical site. All pups (from each cohort) were also fed 1-3x daily using a mixture of kitten milk replacement (KMR) powder in water at a 1:3 ratio to help maintain proper growth as recommended by veterinarian staff. Pups were fed using a 1ml syringe, with KMR droplets placed near the pup's mouth, allowing the animal to eat ad libitum, and the feeding halted when the animal no longer consumed the KMR droplets. After the first three days of post-operative care, animals were then monitored every 2-3 days, with carprofen, lidocaine/neomycin administration only when the animal demonstrated signs of distress, pain, or reddening of the surgical wound.

Auditory Brainstem Responses (ABR). Gerbils were anesthetized with an intraperitoneal injection of ketamine/xylazine by weight (100mg/kg ketamine; 20mg/kg xylazine – K/X). Animals were given ophthalmic ointment and kept on an IR heating pad to maintain body temperature for the duration of the procedure. After preparation, the animals were then transferred to a sound-isolation booth and implanted with 3 temporary sub-dermal electrodes: at the vertex of the head, just posterior to the pinna, and with a ground electrode in the thigh. Animal hearing was tested across a variety of frequency (clicks; 500Hz-16kHz) and intensity combinations (30-90dB; 10dB intervals) to determine the lowest threshold response. Thresholds were determined as the lowest intensity for a given

frequency that generated a response greater than 4 standard deviations above the noise. Both left and right ears were tested for each frequency and broadband click, with the threshold across left and right ears averaged together to generate one response threshold (dbSPL) for the corresponding stimulus frequency for a given animal. Animals that had no responses for all intensities were marked as No Response (NR). Gerbils were given a second, smaller dose of K/X at the same concentration by weight after testing one ear, and before moving to the test the second, as needed to maintain proper anesthetic depth. In order to blind the experimenter to the hearing status for future electrophysiological and microdissection experiments, a second researcher took the animal and discretely shaved a random portion of fur, documenting the shave pattern. The main experimenter was kept blind to the animal's hearing status, and it was revealed only after all littermates had been utilized. Furthermore, the second researcher provided post-operative care, by transferring animals to an isolated cage with a second heating pad and providing sterile saline (as needed), with active monitoring every 30m until waking. Due to size limitations, and the difficulty of using ketamine/xylazine as an anesthetic for neonates, we did not test the hearing for the Prehearing Neonate cohort to confirm if phenomena such as bone conduction were passing low-frequency sounds into the developing auditory system.

Brain Slice Preparation. Mongolian gerbils (P18-25) were anesthetized with isoflurane then decapitated upon reflex cessation. Brains were removed and prepared with a coronal blocking cut through the superior colliculus. Slice preparation and recordings were performed in artificial cerebrospinal fluid (ACSF) warmed to 35°C bubbled continuously with 95% O₂/5% CO₂, using the following salt concentrations (mM): (125 NaCl, 25 D-Glucose, 2.5 KCl, 25 NaHCO₃, 1.25 NaH₂PO₄, 1.5 MgSO₄, 1.5 CaCl₂ – pH adjusted to 7.45 with NaOH). Slices were cut at 200µm, then incubated for 30m at 35°C after dissection, then stored at room temperature until used for recordings (35°C). For gerbils older than P25, the animals were additionally perfused with warmed (35°C) ACSF prior to dissection to improve slice quality by more rapidly clearing blood from the brain.

Electrophysiological Recordings. Whole-cell current-clamp recordings were made using Dagan BVC-700A amplifiers with voltage data filtered at 5kHz, digitized at 50-100 kHz,

and acquired using custom-written code in Igor Pro (WaveMetrics). Recording electrodes were pulled from thick-walled borosilicate glass (1.5/0.86mm OD/ID; 4-8M Ω) and filled with intracellular solution containing 115 mM K-gluconate, 4.42 mM KCl, 0.5 mM EGTA, 10 mM HEPES, 10 mM, Na₂Phosphocreatine, 4 mM MgATP, and 0.3 mM NaGTP, osmolality adjusted to 300 mOsm/L with sucrose, pH adjusted to 7.30 with KOH. Biocytin (0.1%) was added to allow for cell labeling and subsequent localization within the MSO. For Patch-seq recordings, the intracellular solution was modified to maintain RNA integrity, see below for specifics.

All membrane potentials shown are left uncorrected for the estimated 10mV junction potential. Bridge balance and capacitance compensation were monitored in all recordings. All recordings were carried out at 35° C with oxygenated ACSF perfused at a rate of ~2-4 mL/min.

Data Analysis of Electrophysiological Recordings. Measurements of firing pattern were made by generating a series of VI steps (400ms duration) sweeping from a hyperpolarizing step eliciting a voltage response of -120mV up to a maximal firing rate for the cell. Cells that fired more than one action potential (AP) in response to any current injection were termed “repetitive,” while those that maintained only one AP/stimulus were termed “phasic.” Further responses were recorded at the firing threshold (determined by having a success/failure ratio of ~50% for 100+ stimulus injections). Individual AP parameters were measured from these responses based on a modified third derivative peak detection method (www.github.com/dhaimes-b/Threshold_Analysis) to locate threshold and determine subsequent measurements. Briefly, the third derivative of the voltage response was generated for each spike waveform, and a window was set just prior to the peak of the action potential. Subsequently, the window was visually inspected for the presence of one or two positive peaks. In the case of two peaks, the first peak was assigned as threshold (the putative activation at the spike initiation zone), while the second was assigned as somatic threshold (activation of subsequent somatic sodium channels). In instances of only one peak, it was assigned as threshold. All thresholds were confirmed by visual inspection on phase-plane plots and the initial spike waveform. Further, the third derivative detection

methodology was used in conjunction with other threshold detection methods (Sekerli et al., 2004) and found to yield divergent results typically only when two peaks were present. Other methodologies usually deferred to the second peak and thus yielded a depolarized threshold and less accurate threshold (sometimes as large as a 10mV different). Therefore, we utilized the third derivative method for all analyses.

Microdissection and mRNA Isolation. Using 3 biological replicates for each hearing condition (Prehearing Neonate, Posthearing Juvenile, Surgical Sham Juvenile, Cochlear Ablation Juvenile), coronal slices were generated as above in **Brain Slice Preparation** and were transferred to watch glasses containing oxygenated ACSF. Under observation through a dissection scope, brain regions of interest were manually dissociated from the tissue using a scalpel. The tissue of interest was then transferred immediately into a tube containing RNA-Later (Sigma, cat#: R0901) for temporary storage. Tissue was then manually disrupted and spun through a QIAshredder column (Qiagen, cat#: 79656) for full homogenization in Buffer RLT with 1:100 BME. RNA was isolated following protocol available from QIAGEN, with added DNase digestion performed on column, incubating at RT (15 min). RNA was harvested with a Qiagen Micro-RNA isolation kit (Qiagen, cat#: 74004) for each sample. Final concentration of RNA yield was confirmed on a Nanodrop. RNA samples were temporarily frozen at -80°C until delivered to the Genomic Sequencing and Analysis Facility (GSAF) for library preparation and 3' TagSeq sequencing.

3' Tag mRNA Library Preparation and Sequencing. Tissue samples were provided to the GSAF in triplicate for each hearing condition (PRE, POST, SHAM, DEAF), for a total of 12 unique samples prepared via the **Microdissection and mRNA Isolation** protocol. Subsequent 3' TagSeq library preparation (Lohman et al. 2016; Meyer et al. 2011), a 3' end tag-based RNA sequencing technique, was performed by the Genomic Sequencing and Analysis Facility (GSAF) at the University of Texas at Austin. Briefly, RNA was extracted by adding Trizol (Thermo Fisher) and then cleaned using an RNeasy MiniElute Cleanup Kit (Qiagen). RNA Integrity numbers (RIN) for each sample were measured using an Agilent Bioanalyzer, with 100ng of total RNA used in the TagSeq protocol modified from Lohman et al. 2016.

RNA was heat fragmented at 95°C for 2.5 minutes in the first strand cDNA synthesis solution of dNTPs (NEB), DTT (Agilent), SMARTscribe 5X first strand-synthesis buffer (Takara), and 3ILL-30TV primer. After cooling the fragmented RNA on ice, SMARTscribe Reverse Transcriptase (Takara) and template switching oligonucleotide were added to each sample, followed by incubation at 42°C (1 hour), then 65°C (15 min). The first-strand cDNA was purified with AMPure XP beads (Beckman Coulter) and amplified using Klentaq1 DNA polymerase (DNA Polymerase Technology) and 5ILL and 3ILL-30TV primers (Lohman et al. 2016) with the following PCR conditions: one cycle of 94°C for 5min; 18 cycles of 94°C for 1min, 63°C for 2min, 72°C for 2min. Following another AMPure bead purification step, i5 and i7 indices were added through 4 subsequent PCR cycles. Purified final libraries were quantified using the Quant-it PicoGreen dsDNA assay, and then pooled equally for size selection on a 2% gel using the Blue Pippin (Sage Science, 350-550bp). The libraries were then sequenced using an Illumina HiSeq 2500 instrument (101nt single reads).

Tag-Seq Sequence Data Processing. Fastq datasets were assessed for quality before and after pre-processing using FastQC [v0.11.9], aggregated with the MultiQC program (Ewels et al., 2016). Fastq files were trimmed of the first 10bp using the fastx_trimmer toolset (v 0.0.13). Subsequently, files were aligned using HISAT2 (v 2.1.0) against the gerbil transcriptome (MunDraft-v1.0 – Ensembl release 100). Abundances were quantified using Salmon (v0.12.0), with downstream transcript abundance analysis performed in R and RStudio (v3.4.4). The tximport package (v1.6.0) (Soneson et al., 2015) was used to generate gene-level counts from the abundance outputs from Salmon. Count data matrices were pre-filtered to remove genes with fewer than 5 reads across all included samples. Counts were then provided to the DESeq2 package for negative binomial modeling (v1.18.1) (Love et al., 2014). Differentially expressed gene results reported are those with maximum adjusted p-value <0.1 and log₂ fold change greater than or less than 1.0 for each pairwise comparison of cohorts. Tests were also performed to test null hypotheses with varying log fold change differences other than 0, with no significant changes detected (1.5x, 2x – data not shown). Gene ontology (GO) analysis was performed using PANTHER

online system (v16.0). Genes were separated into up- or down- regulated based on LFC thresholds of double, and $\text{padj} < 0.1$. Genes were then separately run through the online system against a Mouse reference (*Mus musculus*). The output of protein class enrichment and reductions were plotted based on the PANTHER calculated $-\log_{10}$ p-value.

Patch-Seq Recordings. Patch-seq recordings were made using an adapted protocol from Cadwell et al. (2016, 2017) . Slices were prepared from Mongolian gerbils as above, using the recommended modified internal solution containing RNase-OUT (see reference for details). All surfaces, rig, equipment, and glassware were cleaned with RNase-Zap followed by ddH₂O. Whole-cell current-clamp recordings were made to ascertain the overall spiking pattern, and threshold spike parameters. Subsequently, the cell was extracted using a ramping negative pressure (0-6psi) with visual confirmation that the soma shrank and often that the nucleus was extracted up into the recording pipette. The recording pipette was then removed from the bath, and using application of a clean positive pressure device, expelled into a 96 well plate of prepared lysis buffer stored on ice, while gently cracking the tip of the pipette. Lysis buffer was prepared (for a single sample) with 1.75 μ l Nuclease-free sterile water, 1.15 μ l Triton X-100 (0.33% vol/vol), 0.8 μ l dNTPs (25mM each), 0.1 μ l Oligo-dTVN (100 μ M), 0.1 μ l Recombinant RNase Inhibitor (40U/ μ l), 0.1 μ l ERCC spike-ins (1:4x10 dilution): total volume 4 μ l/sample. Lysis buffer was made as a master mix fresh daily, then aliquoted into wells. 96 well plates were kept on ice until the end of the recording session, and then were sealed with PCR foil (Eppendorf, cat#: 0030127790) and transported to the GSAF for immediate downstream library preparation.

Patch-Seq cDNA generation/library prep/sequencing. RNA denaturation, reverse transcription, and cDNA amplification were performed according to Cadwell et al. (2017). Amplified cDNA was purified using AMPure XP beads (Beckman Coulter) and cDNA size and quality were assessed on a Bioanalyzer (Agilent). We used the Quant-iT PicoGreen dsDNA assay (Invitrogen) to quantify and normalize cDNAs to 100pg/ μ l. Subsequently, library preparation was performed according to the manufacturer's instructions for the Nextera XT DNA Library Preparation Kit (Illumina) using $\frac{1}{4}$ volume for all reagents and samples. Libraries were indexed with the IDT for Illumina Nextera DNA UD Indexes

(Illumina). All libraries were then quantified using the Picogreen assay (Invitrogen) and pooled equally. A final AMPure XP bead cleanup was performed on the pooled libraries, followed by qPCR using the KAPA Sybr Fast qPCR Kit (Roche). Libraries were sequenced on an S1 flow cell on the Novaseq 6000 platform (Illumina) with a single-end read length of 100 bases and an average read depth of 10million reads per sample.

Patch-Seq Data Processing and Bioinformatics. Fastq files were assessed for quality before and after pre-processing using FastQC (v0.11.9). Files were trimmed using cutadapt [v2.8] (Martin, 2011) for the first 10bp and merged across lanes. Fastq files were then aligned using STAR with a STAR index built from the gerbil genome (MunDraft-v1.0.102 from Ensembl release 102) merged with ERCC sequences available from ThermoFisher (catalog #4456740). Annotation files were pulled from the same genome assembly file through Ensembl. After alignment, reads were counted using featureCounts [v2.0.0] (Liao et al., 2014). Output files were then imported into RStudio (v4.0.3). ERCC content was calculated as a percentage of total counts for each sample. Negative control plucks (pipette placed above tissue, without recording or aspirating cell contents) were confirmed as all having >98% ERCC content to control for extraneous mRNA that may have contaminated samples. Positive controls samples had between 5-20% ERCC content, within normal ranges (Lun et al., 2017). Further normalization by ERCC was not performed, as the literature is mixed about improvement in data modeling, and preliminary normalization using ERCC yielded similar results for our analyses. Therefore, modeling was done using Seurat [v4] (Hao et al., 2021), with a total of 25,743 genes before filtering, using log normalization with a scale factor of 10,000 (the default parameters). Pseudotime analyses were performed using monocle 3 [v3] (Trapnell et al., 2014), and Slingshot [v2] (Street et al., 2018). Machine learning classification was done using the rpart [v4.1-15], and randomForest [v4.6-14] packages.

FIGURES AND FIGURE LEGENDS

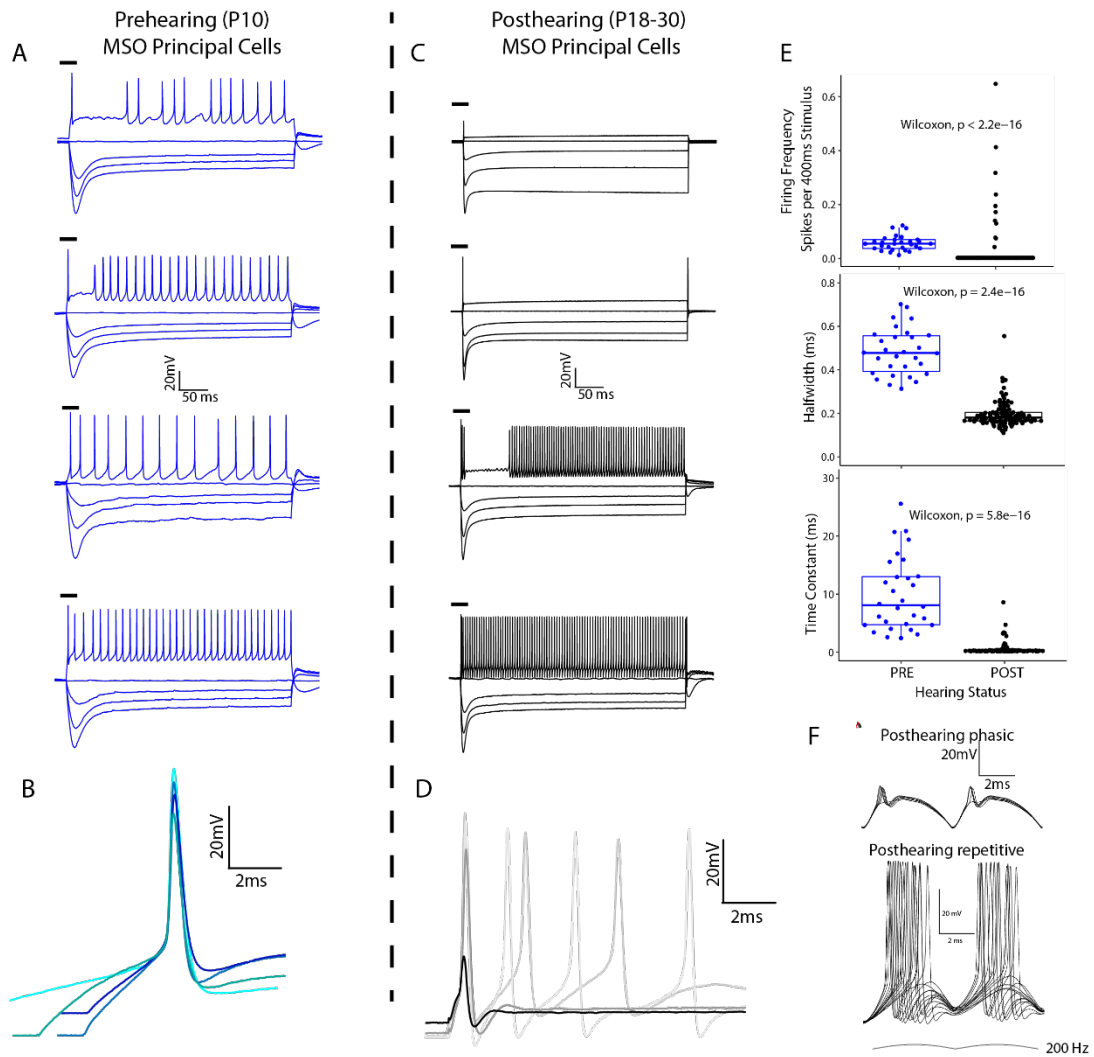


Figure 5.1: Intrinsic firing properties of MSO principal neurons change significantly after hearing onset in Mongolian gerbils.

Voltage responses were generated by a series of square current injections using whole-cell current clamp in brain slices generated from two ages of Mongolian gerbil, before and after hearing onset (Prehearing colored blue, Posthearing colored black). A) Four example voltage responses from different cells recorded from Prehearing (postnatal day 10 – P10) gerbils. Black bars represent the area expanded and shown in **B**. B) Initial responses to threshold current injection shown, aligned by the voltage threshold of the response. C) Four unique cell responses that represent a continuum of response properties in principal cells of the maturing posthearing MSO. D) Threshold-aligned voltage responses from C, exhibiting the diversity of firing pattern and initial action potential size and shape. E) Group data quantifying the firing frequency (top), defined as the number of spikes over the 400ms stimulus square pulse. Halfwidth (middle) and time constant (bottom) show changes in action potential shape and passive properties before and after hearing onset (onset starts at P12). F) Diverse posthearing firing responses in response to slow half-rectified sine-wave current injections, intended to simulate slow envelope-like component of sound stimuli (data originally from Bondy et al. 2021, different example reproduced here).

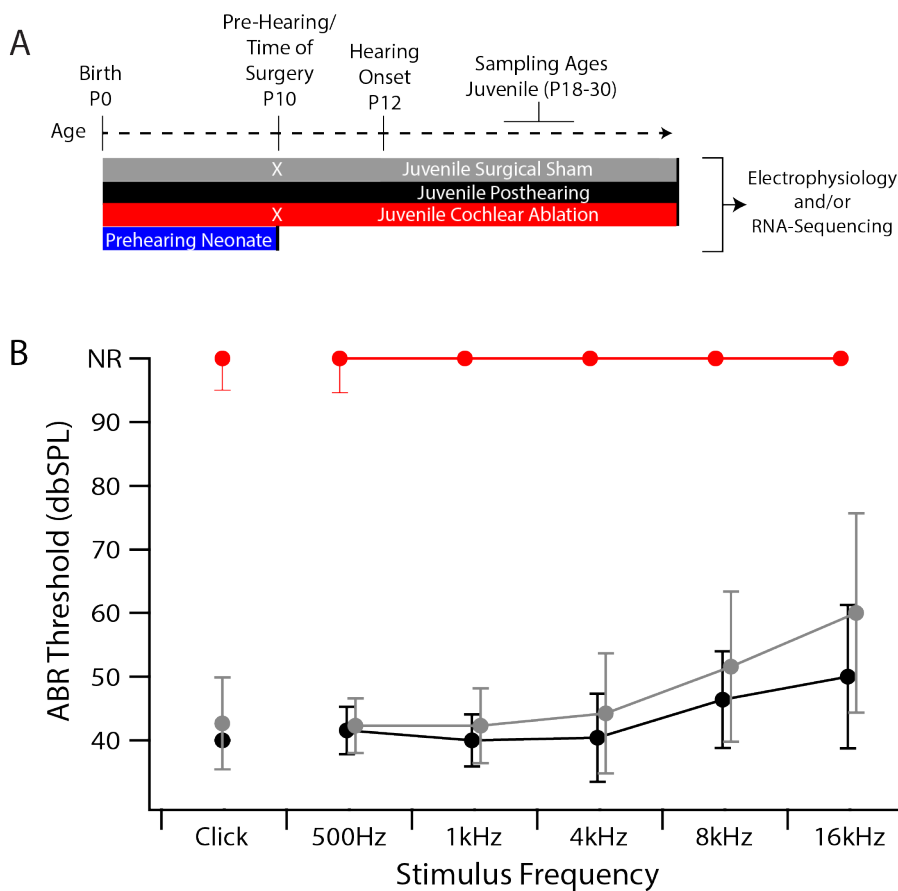


Figure 5.2: Experimental design tests the intersection of hearing activity and development on intrinsic neuron properties.

A) Four cohorts of Mongolian gerbils were generated to test the influence of auditory activity and/or development on changing intrinsic properties. Prehearing neonates (PRE) were sampled at P10, prior to hearing onset (P12), which is delayed in gerbils until the ear canal fully opens. Non-surgical controls were utilized as a post-hearing juvenile sample (POST), while surgical sham juveniles (SHAM) and bilateral cochlear ablation (DEAF) cohorts were generated by performing surgery at P10 (white X). POST, SHAM, and DEAF cohorts were assessed for hearing status via Auditory Brainstem Response (ABR) threshold testing at P18-P25. B) All juvenile cohorts were tested across a variety of threshold-intensity combinations (broadband click, 500Hz-16kHz; 30-90dB, 10dB increments), and manually assessed for the lowest response intensity based on a signal >4 standard

deviations above the noise. No Response (NR) was given as a nominal value when animals did not respond to stimuli at any intensity.

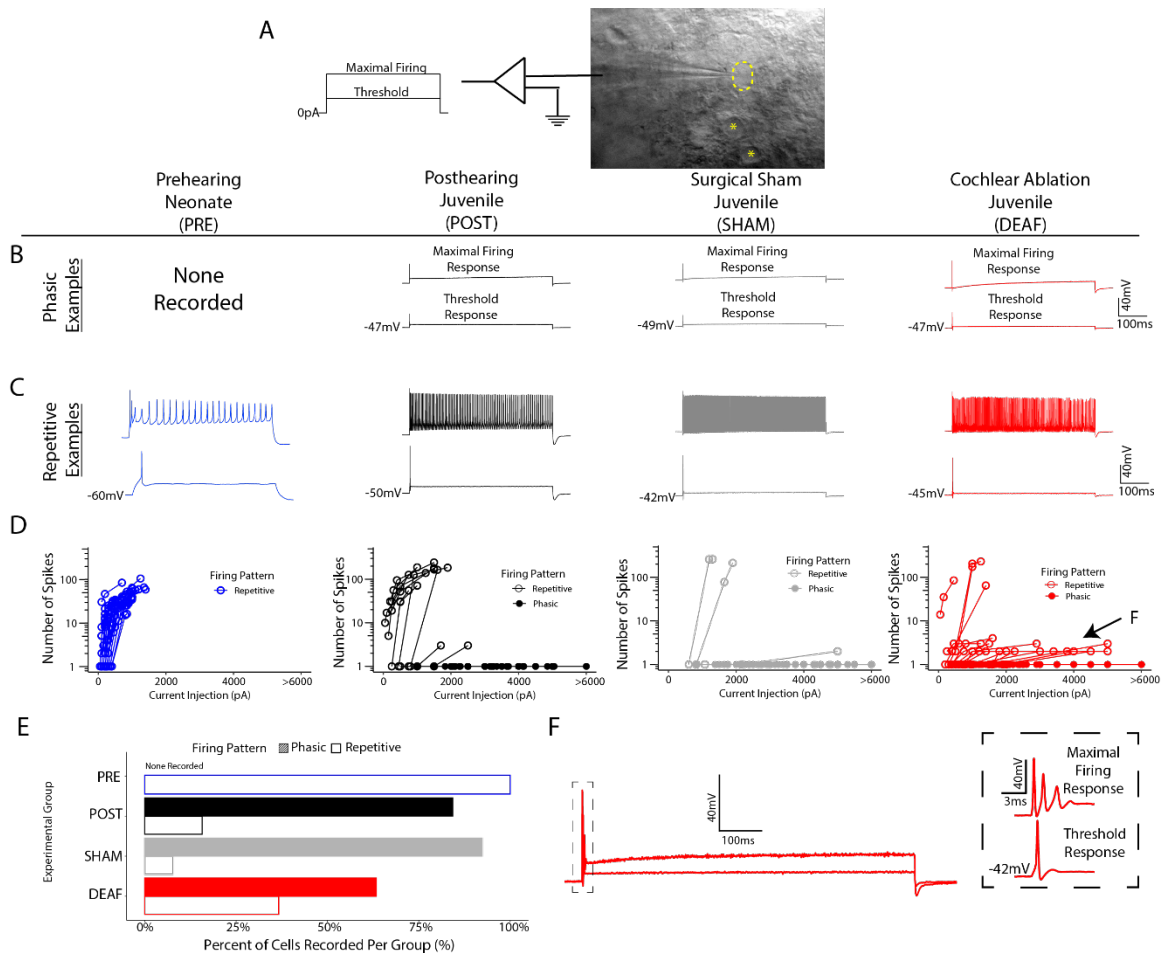


Figure 5.3: Firing heterogeneity changes with development age and hearing status.

Gerbils from two age time points (Prehearing - P10; Posthearing >P17), and hearing statuses (litter weight control/no surgical intervention; surgical sham; cochlear ablation), were used for current clamp recordings from the MSO to assess firing pattern differences. (A) Cartoon illustrating whole cell current-clamp recordings were made with MSO neurons (example cell highlighted with yellow oval; other MSO somas demarcated with yellow asterisks) with responses elicited from a series of increasing current steps that elicited a threshold firing response, up through the current that elicited maximal firing in the neuron. (B) Phasic examples across four age/hearing statuses. Prehearing neurons are marked “None Recorded” as no phasic neurons were seen across all prehearing recordings (n=31). Traces show two example depolarizing current injections, the lower at threshold, and higher at the maximal firing rate, all traces are scaled to the scale bars on the right (100ms, 40mV). (C) Repetitive neuron examples defined by spike counts greater than 1 with any current injection amplitude - shown in D. (D) Group data showing spike count (log scale) versus increasing current injections, graphs are truncated at 6000pA for clarity, current

injections above 6000pA are displayed at >6000pA. The only response type seen at >6000pA was phasic. Neurons split into two groups, phasic or repetitive depending on whether they only fired a single onset spike for all current steps tested (phasic - closed circles), or more than one spike (repetitive - open circles). E) Bar graph shows the proportion of each firing type recorded as a percentage from each group. Prehearing had no phasic firing neurons, and is marked "None Recorded". F) Example threshold and maximal firing traces show that many repetitive neurons in Cochlear Ablation Juvenile exhibited "Onset Bursts," where multiple spikes could be seen in response to the stimulus onset, rather than a single onset spike as in typical phasic firing phenotypes.

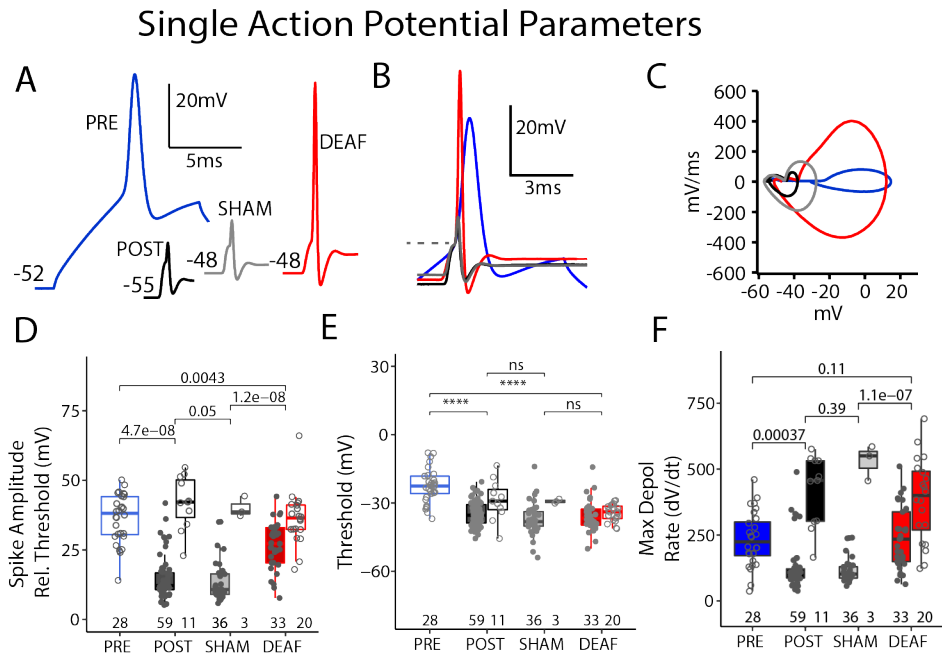


Figure 5.4: Single action potential parameters change with age and hearing loss.

Spike responses were generated with current injections as close to threshold as possible and analyzed for a series of AP parameters, using either the transient onset response, or first spike in a burst/train. (A) Representative averages of threshold spikes shows differences in spike size and shape. (B) Action potentials from (A) threshold aligned (grey dotted line represents threshold). (C) Phase plane plots generated from representative spikes (A). (D-F) Group analyses performed across each hearing/age grouping Prehearing Neonate (n=31), Posthearing Juvenile (n=73), Surgical Sham Juvenile (n=41), Cochlear Ablation Juvenile (n=61). Statistical tests were performed in R using non-parametric Kruskal-Wallis tests, followed by pairwise comparisons with a Wilcoxon test, asterix (*) indicates $p < 0.001$, ns for non-significant ($p > 0.05$).

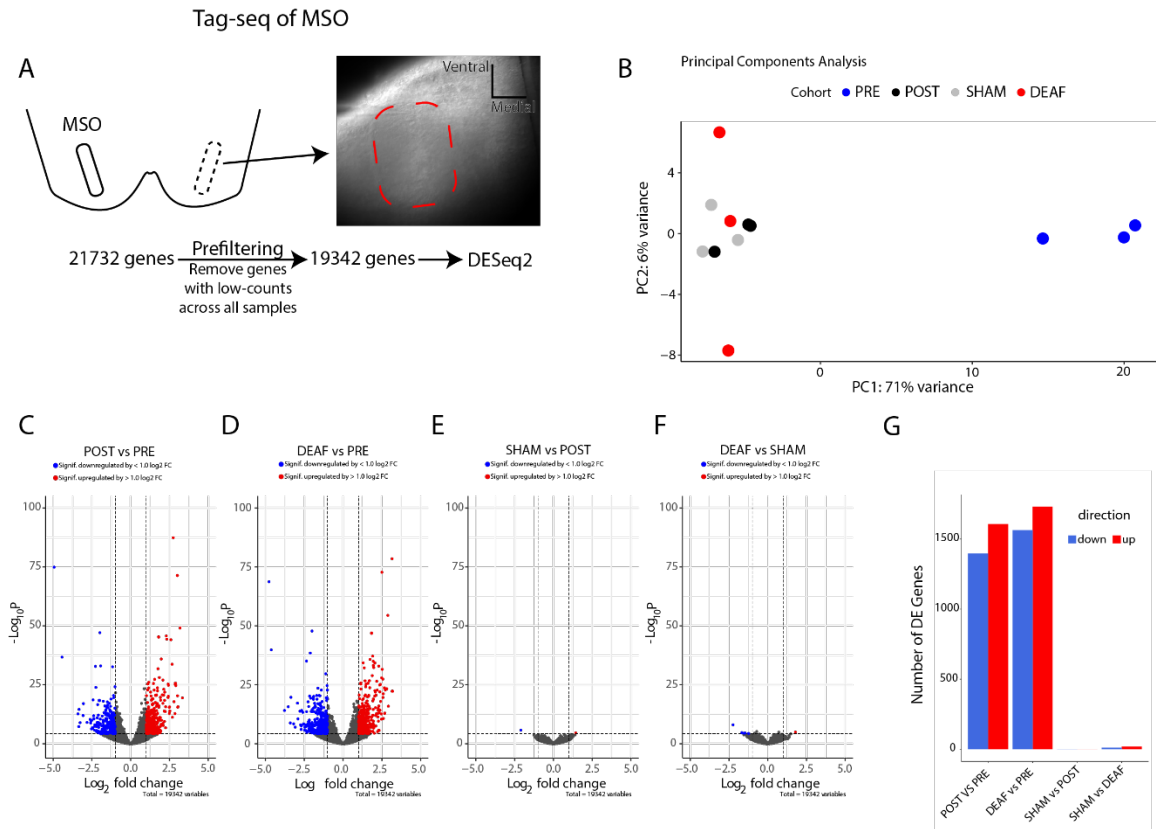


Figure 5.5: 3'-mRNA-sequencing of micro-dissected MSOs shows major change in the transcriptome across development, but not in response to hearing loss.

A) We performed 3' -mRNA sequencing to determine how gene expression changes with response to hearing activity and normal animal development by microdissecting the MSO using a dissection microscope. Using three biological replicates for each group (Prehearing neonate; Posthearing juvenile; Surgical Sham juvenile; Cochlear Ablation juvenile), we analyzed 21,732 genes expressed, which were modeled and displayed in low-dimensional space (B). After filtering to remove genes with low total counts, we used DESeq2 to model our expression data, and then subsequently generated results tables for each pairwise comparison across hearing and age. These results tables are summarized as volcano plots (D-F), with vertical cutoffs added for a doubling of expression (dotted lines), and horizontal cutoffs to demarcate a p value cutoff at 10e-6 (BH adjusted p-value $p < 0.1$). Genes that were found to have log₂ fold changes either up (red) or down (blue), and statistically

significant, are colored. G) The total number of genes for each pairwise comparison were counted and summarized as a bar graph.

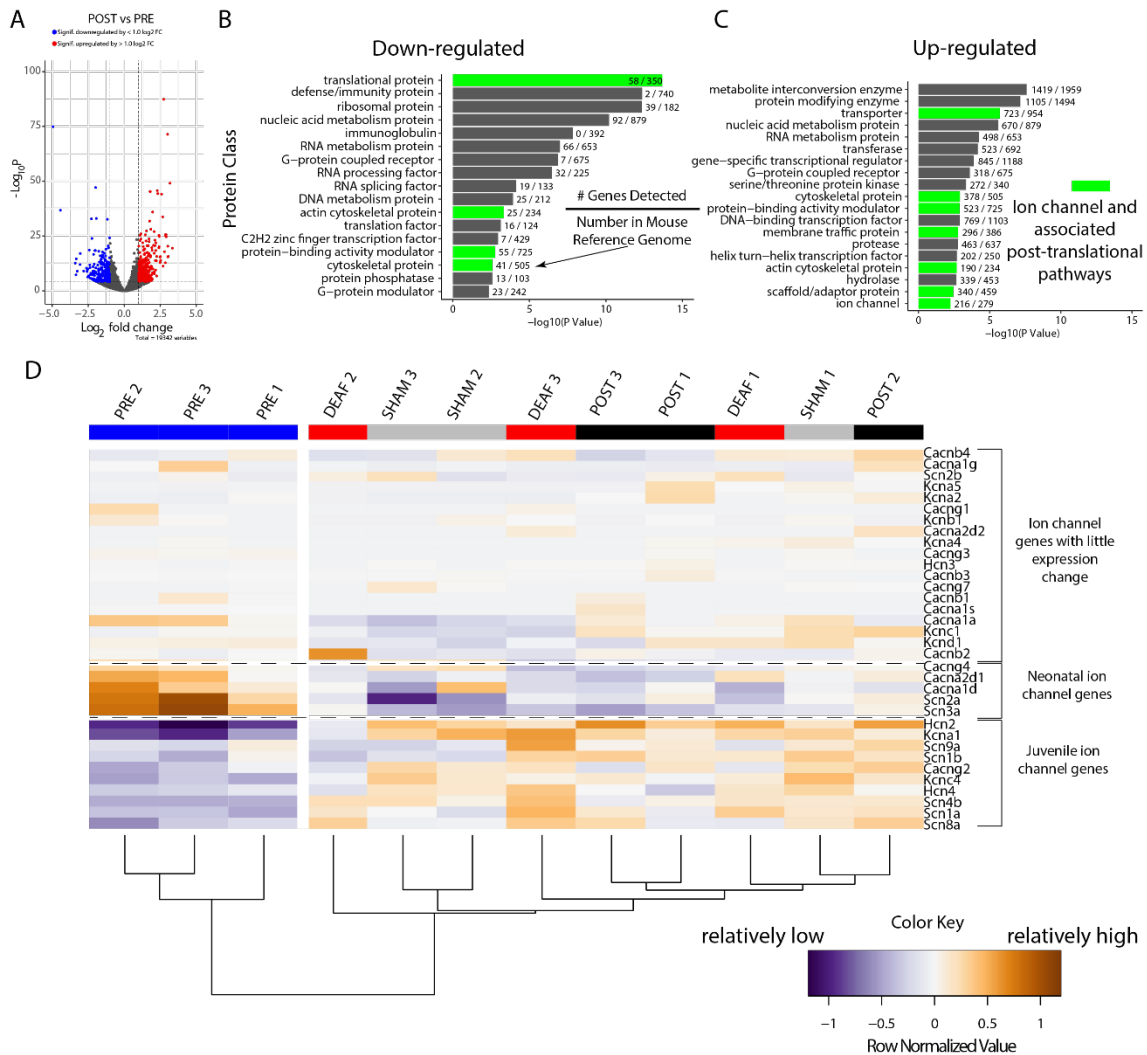


Figure 5.6: Pre- and post-hearing changes to the transcriptome strongly implicate a switch in ion channel expression and post-translational pathways.

Analysis of the mRNA expression dataset generated through 3' Tag-sequencing was subsetted to look specifically at genes with significant (adjusted p-value < 0.1) differences in expression level (Figure 3). (A) Using the 1607 genes that are significantly up-regulated, and 1397 genes that down-regulated, we pooled all 3004 genes for gene ontology analysis (GO). (B) Looking for genes organized by molecular function, we found many GO terms experience global change. Furthermore (C) classification of the proteins that correspond to these genes revealed structural and metabolic pathways that change in response to hearing

onset. (D) To follow up on the presence of changing ion channels and their activity (B-C), we analyzed the variance-stabilized dataset for a curated list of voltage-gated ion channels that might explain differences exhibited in Figures 1-2. Using a heatmap of expression level normalized by dividing each expression by the total expression levels for that gene, we can determine relative patterns in genes. While many ion channels had little change in expression (z-score of approximately 0), we detected genes that either exhibited high expression (z-score > 0.5) in our neonate samples and low (z-score < 0.5) in juvenile (categorized as “Neonatal ion channel genes), or the opposite (categorized as ”Juvenile Ion channel genes”).

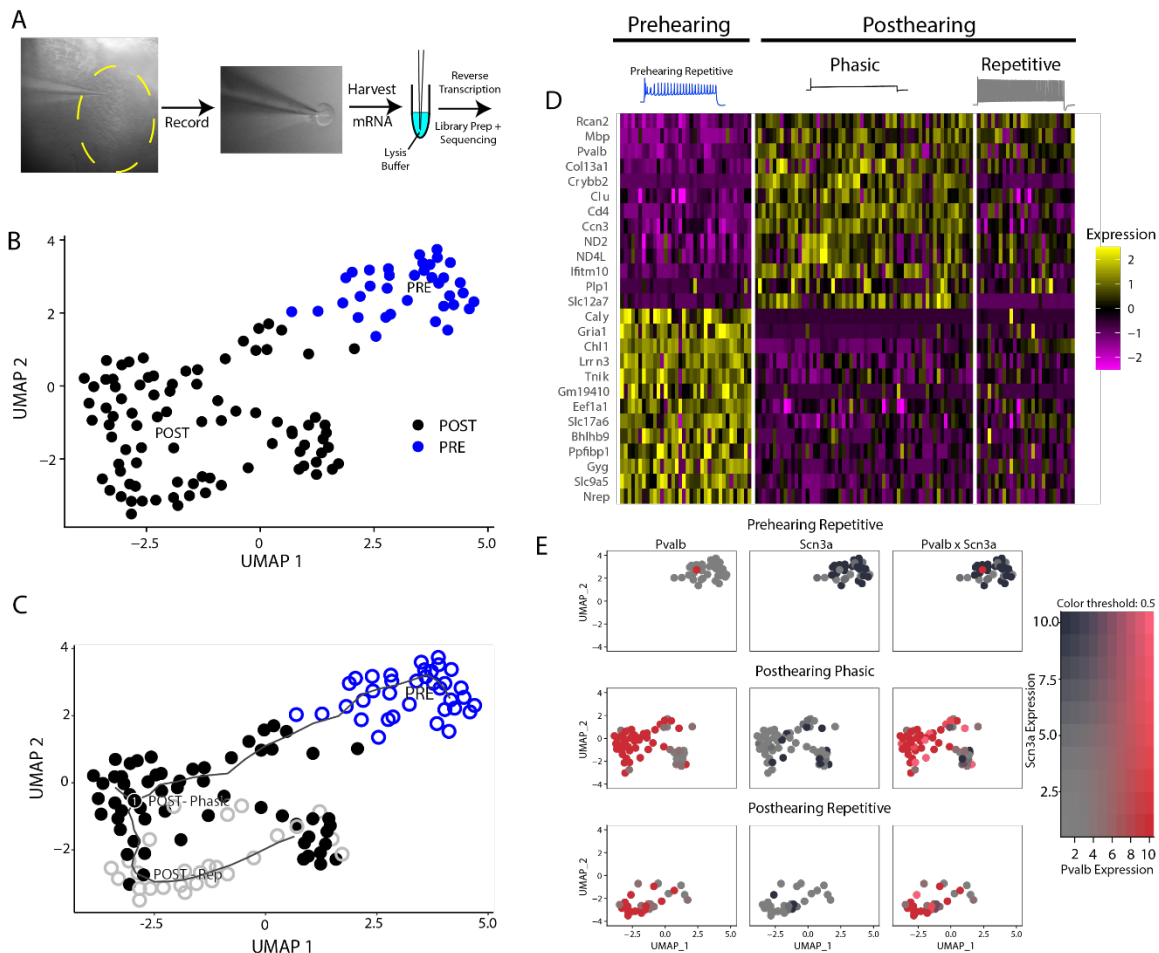


Figure 5.7: Posthearing repetitive neurons are not undifferentiated prehearing repetitive neurons.

A) Using single-cell resolution Patch-seq, which combines electrophysiological recordings with subsequent mRNA harvesting and sequencing, we correlated firing properties with transcript abundance. Generating a dataset of 25,742 genes, we used Uniform Manifold Approximation and Projection (UMAP) to assess patterns. B) Patch-seq analysis recapitulates the PRE and POST separation found in 3'mRNA-sequencing. C) Overlaying neuron firing type showed the distribution of POST-phasic neurons (closed black circles), POST-repetitive neurons (open grey circles), and PRE-repetitive neurons (open blue circles). Pseudotime analysis generated a developmental trajectory overlay (black line), with only a slight bifurcation within a posthearing cluster (black circle marked "1"). D)

Highly variable gene analysis of normalized gene expression for the top 15 most variable genes that were up and down regulated. Firing type and hearing status is mapped above the heatmap with example traces for clarity. E) Two genes were selected to test expression levels, Pvalb and Scn3a. UMAP spaced is used to display, with each row corresponding to a firing type (top - Prehearing Repetitive; middle - Posthearing Phasic; bottom - Posthearing Repetitive). Transcript abundance is displayed based on the heatmap to the right (Scn3a - black; Pvalb - Red), with coexpression being a merge of the two colors. Cutoffs were utilized at the minimum, q10 and maximum, q90 to increase visual clarity.

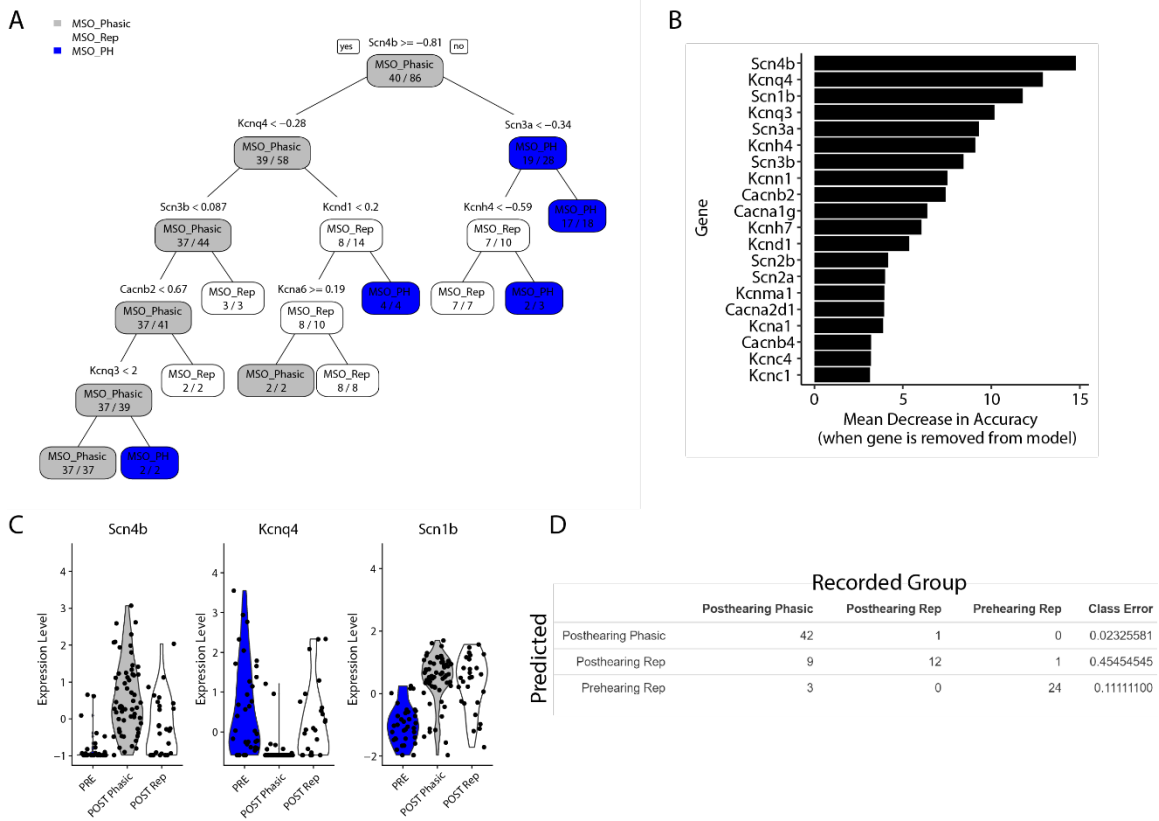


Figure 5.8: Machine-learning algorithms accurately predict firing type from ion channel transcript abundance data.

Using a curated list of primarily pore-forming ion channel gene transcripts, we used a supervised machine-learning classifier to predict firing type. A) One example decision tree generated shows the binary decision making process to predict firing type from ion channel expression. B) To increase the robustness of our modeling, we utilized a random forest algorithm, generated 500 decision trees, and summarized the model across the entire forest (overall out-of-box error ~15%). Gene prediction variables with the most impact on model accuracy were rank-ordered and displayed in bar graph format. C) Violin plots of gene expression confirm the top 3 most predictive random forest genes have unique firing-type specific patterns. D) Table of class prediction error shows that random forest models are able to accurately predict Posthearing Phasic (error ~2%) and Prehearing Repetitive (error ~11%), while exhibiting difficulty predicting Posthearing Repetitive neurons (error ~45%).

Bias in prediction error for Posthearing Repetitive neurons is unidirectional, as 9/10 incorrect predictions were towards Posthearing Phasic neurons.

Chapter 6: Conclusions and Future Directions

CONCLUSIONS

I have presented here the majority of my work studying sound localization circuitry in the mammalian brainstem. In it, the reader will find a general theme aiding in modernizing the duplex theory of sound localization, pushing against the dogmatic views of discrete frequencies anatomically segregated for information processing. With the more modern perspective of this theory, that rather than the MSO discretely processing low-frequency information, and the LSO focused on high-frequency sounds, the compilation of these three works is unified by demonstrating that sound is a complex stimuli, and thus the neurons that process it are equally unique. For the LSO, the weight of arguments created in the Joris lab was furthered with our work here investigating precise LSO neurons, sensitive to not just intensity coding paradigms, but exquisite in their temporal properties.

Throughout the body of my primary work, we further add to the duplex theories of sound localization by emphasizing that MSO neurons exist along a continuum of response properties, as neurons must respond to a variety of frequencies and more importantly, features of auditory stimuli. This continuum of response properties reflects the salient features of sound, with repetitive neurons with markedly slower membrane properties responding robustly to envelope-like stimuli. Therefore, this work emphasizing diversity in neuron processing demonstrates that sound localization is not just split anatomically, but that various features of sound are extracted based on the unique computational specializations exhibited by neurons throughout the SOC. The diversity and novelty of these works adds to this evolving modern perspective as we gain a more nuanced understanding of how the brain extracts spatial information from features of sound.

Additionally, the work discussed in **Chapter 5**, provides an integrative perspective extending previous works performing on hearing loss and developmental changes to neuronal properties. Tying together these two vital axes that influence the various properties of neurons, we demonstrate that the development fate of neuronal cells is strongly fixed, regardless of the activity state. Interestingly, subtle changes to the diversity of firing properties seen in hearing loss models argues that activity triggers post-translational protein pathways to fine-tune response properties to sound stimuli. While it is unclear which specific pathways might be activated – protein modification, stability, degradation, trafficking, etc. – this work provides a foundation for future studies to drill deeply into how unique auditory experiences may directly act through a multitude of pathways. Given past experiments that utilize omni-directional noise paradigms (that remove ITDs the MSO relies on), or auditory enrichments experiments that demonstrate modifications to potassium channel proteins, our work provides further emphasis that these types of experiments may yield insight into how exactly neural properties are fine-tuned.

Moreover, we hope that this work will continue to push fellow neuroscientists to reconsider what truly defines a cell type in the brain. Historical classifications of principal vs non-principal neurons may not be accurate, as demonstrated here, and expectations of a neuron to exhibit consistent properties may not be relevant when the input stimuli is itself diverse. More importantly, the role of a neuron in a given circuit should always be considered in context to truly understand the computation being performed.

RECOMMENDATIONS FOR FUTURE WORK

Given the work discussed here, we provide several recommendations for future directions. In the near future, we hope to see proteomics that follows directly from the work generated here. Specifically, we would recommend using modern proteomics approaches such as DIF-FRAC, or other co-fractionation mass-spectrometry techniques to begin assessing large protein complexes in neuronal membranes. This level of study would tie together several fields of interest. In particular, this approach could be utilized to directly follow up on the RNA-sequencing GO term results that demonstrate that a variety of mRNA and protein modification pathways are altered in the MSO across development. By using co-fractionation mass-spectrometry to directly investigate the membrane-bound protein complexes, we could get further insight into exactly which ion channel proteins are expressed, in what modification or modulatory state, and with precisely which accessory proteins. Combined with the electrophysiology and sequencing data presented here, this line of research would provide novel insight into how combinations of ion channel protein complexes yield distinct currents. This would particularly be an advance over common oocyte/stem cell expression systems where ion channels are expressed, but severely lacking their native complex of associated proteins.

Furthermore, using computational biology to investigate protein complexes associated with known axon initial segment proteins (AnkG, B4-Spectrin, and others) would provide foundational evidence for which ion channels are actually membrane bound at the AIS and directly contribute to spike generation, thus building off ongoing molecular work that interrogates the AIS at a molecular level (albeit typically in cultured systems). If further layering of cell type markers allowed computational segregation of these protein complexes, it could further provide insight into how conserved crucial structures such as the AIS truly are. For instance, many neuroscience labs focus on specific brain regions tied

to a unique behavior or function, but using a broader computational proteomics approach mixed with electrophysiology could unravel whether all neurons utilize the same regulatory pathways to generate axonal polarization with the same complexes, or if there are examples of evolutionary divergence in how neurons polarize. We would hypothesize that the AIS is a conserved, highly regulated structure, and thus initial proteomic experiments may not yield novel insight. However, if this approach is further applied to start unraveling whether all dendrites share common protein complexes, or all dendritic spines do, we will begin to understand developmental programs triggered in unique functional areas. Cross-correlation of function and a broader proteomic approach would provide novel insight into many understudied brain regions and subsequently may yield predictive and testable hypotheses for how these regions transform stimuli.

A second line of investigation would be to modulate the auditory activity received by the circuit and further determine whether a critical period for *gene expression* is fundamental for the development of MSO neurons. For instance, use of omni-directional noise-rearing paradigms such as those utilized by the Grothe lab, or use of Vglut3-KO mice, might further begin to investigate the fate of SOC neurons. By controlling the timing, and overall types of cues the auditory system receives after development (particularly removing ITD cues), we would predict, have no impact on the development of MSO neurons. However, usage of a model that impacts activity *before* hearing onset, such as the Vglut3-KO model, which alters the spontaneous waves of activity evoked in the developing auditory system might thus start to unravel how gene expression is fated. This line of evidence, coupled with proteomics, will truly expand our understanding of neural developmental, and particularly start to investigate control of gene expression, whether epigenetics or through other regulatory mechanisms.

References

CHAPTER 1 REFERENCES

- Arons, B. (1992). A Review of The Cocktail Party Effect. *Journal of the American Voice I/O Society*, 12.
- Ashida, G., & Carr, C. E. (2011). Sound localization: Jeffress and beyond. *Current Opinion in Neurobiology*, 21(5), 745–751. <https://doi.org/10.1016/j.conb.2011.05.008>
- Bentley, M., & Banker, G. (2016). The cellular mechanisms that maintain neuronal polarity. In *Nature Reviews Neuroscience* (Vol. 17, Issue 10). <https://doi.org/10.1038/nrn.2016.100>
- Brown, K. D., & Balkany, T. J. (2007). Benefits of bilateral cochlear implantation: A review. In *Current Opinion in Otolaryngology and Head and Neck Surgery* (Vol. 15, Issue 5). <https://doi.org/10.1097/MOO.0b013e3282ef3d3e>
- Brughera, A., Dunai, L., & Hartmann, W. M. (2013). Human interaural time difference thresholds for sine tones: The high-frequency limit. *The Journal of the Acoustical Society of America*, 133(5). <https://doi.org/10.1121/1.4795778>
- Callan, A. R., Heß, M., Felmy, F., & Leibold, C. (2021). Arrangement of Excitatory Synaptic Inputs on Dendrites of the Medial Superior Olive. *The Journal of Neuroscience : The Official Journal of the Society for Neuroscience*, 41(2), 269–283. <https://doi.org/10.1523/JNEUROSCI.1055-20.2020>
- Carr, C.E., & Soares, D. (2002). Evolutionary Convergence and Shared Computational Principles in the Auditory System. *Brain, Behavior and Evolution*, 59(5–6), 294–311. <https://doi.org/10.1159/000063565>
- Carr, Catherine E., & Christensen-Dalsgaard, J. (2016). Evolutionary trends in directional hearing. In *Current Opinion in Neurobiology* (Vol. 40, pp. 111–117). Elsevier Ltd. <https://doi.org/10.1016/j.conb.2016.07.001>
- Clause, A., Sturm, J., Altieri, S. C., Maricich, S. M., & Kandler, K. (2014). Development of Mammalian Primary Sound Localization Circuits. In *Development of Auditory and Vestibular Systems: Fourth Edition* (pp. 249–285). Elsevier Inc. <https://doi.org/10.1016/B978-0-12-408088-1.00009-9>
- Echteler, S. M., Arjmand, E., & Dallos, P. (1989). Developmental alterations in the frequency map of the mammalian cochlea. *Nature*, 341(6238). <https://doi.org/10.1038/341147a0>
- Ehmann, H., Hartwich, H., Salzig, C., Hartmann, N., Clément-Ziza, M., Ushakov, K., Avraham, K. B., Bininda-Emonds, O. R. P., Hartmann, A. K., Lang, P., Friauf, E., & Nothwang, H. G. (2013). Time-dependent gene expression analysis of the developing superior olivary complex. *The Journal of Biological Chemistry*, 288(36), 25865–25879. <https://doi.org/10.1074/jbc.M113.490508>

- Feng, A. S., & Rogowski, B. A. (1980). Effects of monaural and binaural occlusion on the morphology of neurons in the medial superior olivary nucleus of the rat. *Brain Research*, 189(2). [https://doi.org/10.1016/0006-8993\(80\)90112-2](https://doi.org/10.1016/0006-8993(80)90112-2)
- Franken, T. P., Joris, P. X., & Smith, P. H. (2018). Principal cells of the brainstem's interaural sound level detector are temporal differentiators rather than integrators. *eLife*, 7. <https://doi.org/10.7554/eLife.33854>
- Franzen, D. L., Gleiss, S. A., Kellner, C. J., Kladisios, N., & Felmy, F. (2020). Activity-dependent calcium signaling in neurons of the medial superior olive during late postnatal development. *Journal of Neuroscience*, 40(8), 1689–1700. <https://doi.org/10.1523/JNEUROSCI.1545-19.2020>
- Gasser, a., Ho, T. S.-Y., Cheng, X., Chang, K.-J., Waxman, S. G., Rasband, M. N., & Dib-Hajj, S. D. (2012). An AnkyrinG-Binding Motif Is Necessary and Sufficient for Targeting Nav1.6 Sodium Channels to Axon Initial Segments and Nodes of Ranvier. *Journal of Neuroscience*. <https://doi.org/10.1523/JNEUROSCI.5434-11.2012>
- Golding, N. L., & Oertel, D. (2012). Synaptic integration in dendrites: exceptional need for speed. *The Journal of Physiology*, 590(Pt 22), 5563–5569. <https://doi.org/10.1113/jphysiol.2012.229328>
- Grothe, B., Pecka, M., & McAlpine, D. (2010). *Mechanisms of Sound Localization in Mammals*. 90(3), 983–1012. <https://doi.org/10.1152/physrev.00026.2009>
- Grubb, M. S., & Burrone, J. (2010). Activity-dependent relocation of the axon initial segment fine-tunes neuronal excitability. *Nature*, 465(7301), 1070–1074. <https://doi.org/10.1038/nature09160>
- Guinan, J. J., Guinan, S. S., & Norris, B. E. (1972). Single auditory units in the superior olivary complex: I: Responses to sounds and classifications based on physiological properties. *International Journal of Neuroscience*, 4(3). <https://doi.org/10.3109/00207457209147165>
- Hartmann, W. M., Dunai, L., & Qu, T. (2013). Interaural time difference thresholds as a function of frequency. *Advances in Experimental Medicine and Biology*, 787. https://doi.org/10.1007/978-1-4614-1590-9_27
- Hoogenraad, C. C., & Bradke, F. (2009). Control of neuronal polarity and plasticity – a renaissance for microtubules? *Trends in Cell Biology*, 19(12), 669–676. <https://doi.org/10.1016/j.tcb.2009.08.006>
- Howard, A., Tamas, G., & Soltesz, I. (2005). Lighting the chandelier: new vistas for axo-axonic cells. *Trends in Neurosciences*, 28(6), 310–316. <https://doi.org/10.1016/J.TINS.2005.04.004>

- Hoy, R. R. (1992). The Evolution of Hearing in Insects as an Adaptation to Predation from Bats. In *The Evolutionary Biology of Hearing*. https://doi.org/10.1007/978-1-4612-2784-7_8
- Huang, C. Y.-M., & Rasband, M. N. (2018). Axon initial segments: structure, function, and disease. *Annals of the New York Academy of Sciences*, *1420*(1), 46–61. <https://doi.org/10.1111/nyas.13718>
- Huang, Y.-M., & Rasband, M. N. (2016). Organization of the axon initial segment: Actin like a fence. *The Journal of Cell Biology*, *215*(1), 9–11. <https://doi.org/10.1083/jcb.201609084>
- Isaiah, A., Vongpaisal, T., King, A. J., & Hartley, D. E. H. (2014). Multisensory training improves auditory spatial processing following bilateral cochlear implantation. *Journal of Neuroscience*, *34*(33). <https://doi.org/10.1523/JNEUROSCI.4767-13.2014>
- Jeffress, L. A., & A., L. (1948). A place theory of sound localization. *Journal of Comparative and Physiological Psychology*, *41*(1), 35–39. <https://doi.org/10.1037/h0061495>
- Jones, S. L., & Svitkina, T. M. (2016). Axon Initial Segment Cytoskeleton: Architecture, Development, and Role in Neuron Polarity. *Neural Plasticity*, *2016*, 1–19. <https://doi.org/10.1155/2016/6808293>
- Joris, P. X., & Yin, T. C. T. (1995). Envelope coding in the lateral superior olive. I. Sensitivity to interaural time differences. *Journal of Neurophysiology*, *73*(3). <https://doi.org/10.1152/jn.1995.73.3.1043>
- Joris, Philip X, Smith, P. H., & Yin, T. C. . (1998). Coincidence Detection in the Auditory System: 50 Years after Jeffress. *Neuron*, *21*(6), 1235–1238. [https://doi.org/10.1016/S0896-6273\(00\)80643-1](https://doi.org/10.1016/S0896-6273(00)80643-1)
- Kandler, K., Clause, A., & Noh, J. (2009). Tonotopic reorganization of developing auditory brainstem circuits. *Nature Neuroscience*, *12*(6), 711–717. <https://doi.org/10.1038/nn.2332>
- Kapfer, C., Seidl, A. H., Schweizer, H., & Grothe, B. (2002). Experience-dependent refinement of inhibitory inputs to auditory coincidence-detector neurons. *Nature Neuroscience*, *5*(3), 247–253. <https://doi.org/10.1038/nn810>
- Khurana, S., Remme, M. W. H., Rinzel, J., & Golding, N. L. (2011). Dynamic Interaction of Ih and IK-LVA during Trains of Synaptic Potentials in Principal Neurons of the Medial Superior Olive. *Journal of Neuroscience*, *31*(24), 8936–8947. <https://doi.org/10.1523/JNEUROSCI.1079-11.2011>
- Kuba, H. (2012). Structural tuning and plasticity of the axon initial segment in auditory neurons. *The Journal of Physiology*, *590*(Pt 22), 5571–5579. <https://doi.org/10.1113/jphysiol.2012.237305>

- Kuba, H., Adachi, R., & Ohmori, H. (2014). Activity-dependent and activity-independent development of the axon initial segment. *The Journal of Neuroscience: The Official Journal of the Society for Neuroscience*. <https://doi.org/10.1523/JNEUROSCI.4357-13.2014>
- Kuba, H., Ishii, T. M., & Ohmori, H. (2006). Axonal site of spike initiation enhances auditory coincidence detection. *Nature*, *444*(7122), 1069–1072. <https://doi.org/10.1038/nature05347>
- Lohmann And B C M, C., & Friauf, A. R. D. (1996). Distribution of the Calcium-Binding Proteins Parvalbumin and Calretinin in the Auditory Brainstem of Adult and Developing Rats. In *THE JOURNAL OF COMPARATIVE NEUROLOGY* (Vol. 367).
- Magnusson, A. K., Kapfer, C., Grothe, B., & Koch, U. (2005). Maturation of glycinergic inhibition in the gerbil medial superior olive after hearing onset. *The Journal of Physiology*, *568*(2), 497–512. <https://doi.org/10.1113/jphysiol.2005.094763>
- Marrs, G. S., Morgan, W. J., Howell, D. M., Spirou, G. A., & Mathers, P. H. (2013). Embryonic origins of the mouse superior olivary complex. *Developmental Neurobiology*, *73*(5), 384–398. <https://doi.org/10.1002/dneu.22069>
- Masterton, B., Diamond, I. T., Harrison, J. M., & Beecher, M. D. (1967). Medial superior olive and sound localization. *Science*, *155*(3770). <https://doi.org/10.1126/science.155.3770.1696-a>
- Mathews, P. J., Jercog, P. E., Rinzel, J., Scott, L. L., & Golding, N. L. (2010). Control of submillisecond synaptic timing in binaural coincidence detectors by Kv1 channels. *Nature Neuroscience*, *13*(5), 601–609. <https://doi.org/10.1038/nn.2530>
- Nelson, A. D., & Jenkins, P. M. (2017). Axonal Membranes and Their Domains: Assembly and Function of the Axon Initial Segment and Node of Ranvier. *Frontiers in Cellular Neuroscience*, *11*, 136. <https://doi.org/10.3389/fncel.2017.00136>
- Nothwang, H. G. (2016). Evolution of mammalian sound localization circuits: A developmental perspective. In *Progress in Neurobiology* (Vol. 141, pp. 1–24). Elsevier Ltd. <https://doi.org/10.1016/j.pneurobio.2016.02.003>
- Pecka, M., Brand, A., Behrend, O., & Grothe, B. (2008). Interaural time difference processing in the mammalian medial superior olive: The role of glycinergic inhibition. *Journal of Neuroscience*, *28*(27), 6914–6925. <https://doi.org/10.1523/JNEUROSCI.1660-08.2008>
- Pollack, I., & Pickett, J. M. (1957). Cocktail Party Effect. *The Journal of the Acoustical Society of America*, *29*(11). <https://doi.org/10.1121/1.1919140>
- Rayleigh, Lord. (1877). LXI. Acoustical observations . *The London, Edinburgh, and Dublin Philosophical Magazine and Journal of Science*, *3*(20). <https://doi.org/10.1080/14786447708639268>

- Rayleigh, Lord. (1907). XII. On our perception of sound direction . *The London, Edinburgh, and Dublin Philosophical Magazine and Journal of Science*, 13(74). <https://doi.org/10.1080/14786440709463595>
- Roberts, M. T., Seeman, S. C., & Golding, N. L. (2013). A mechanistic understanding of the role of feedforward inhibition in the mammalian sound localization circuitry. *Neuron*, 78(5), 923–935. <https://doi.org/10.1016/j.neuron.2013.04.022>
- Rosskothén-Kuhl, N., Buck, A. N., Li, K., Schnupp, J. W. H., & Reiss, L. (2021). Microsecond interaural time difference discrimination restored by cochlear implants after neonatal deafness. *ELife*, 10, 1–22. <https://doi.org/10.7554/eLife.59300>
- Shi, S.-H., Jan, L. Y., & Jan, Y.-N. (2003). Hippocampal Neuronal Polarity Specified by Spatially Localized mPar3/mPar6 and PI 3-Kinase Activity. *Cell*, 112(1), 63–75. [https://doi.org/10.1016/S0092-8674\(02\)01249-7](https://doi.org/10.1016/S0092-8674(02)01249-7)
- Smith, P. H., Joris, P. X., Carney, L. H., & Yin, T. C. T. (1991). Projections of physiologically characterized globular bushy cell axons from the cochlear nucleus of the cat. *Journal of Comparative Neurology*, 304(3). <https://doi.org/10.1002/cne.903040305>
- Stoler, O., & Fleidervish, I. A. (2016). Functional implications of axon initial segment cytoskeletal disruption in stroke. *Acta Pharmacologica Sinica*, 37(1), 75–81. <https://doi.org/10.1038/aps.2015.107>
- Sun, S., Babola, T., Pregernig, G., So, K. S., Nguyen, M., Su, S.-S. M., Palermo, A. T., Bergles, D. E., Burns, J. C., & Müller, U. (2018). Hair Cell Mechanotransduction Regulates Spontaneous Activity and Spiral Ganglion Subtype Specification in the Auditory System. *Cell*, 174(5), 1247–1263.e15. <https://doi.org/10.1016/J.CELL.2018.07.008>
- Tollin, D. J. (2003). The lateral superior olive: A functional role in sound source localization. In *Neuroscientist* (Vol. 9, Issue 2, pp. 127–143). Neuroscientist. <https://doi.org/10.1177/1073858403252228>
- Tollin, D. J., & Yin, T. C. T. (2002). The coding of spatial location by single units in the lateral superior olive of the cat. II. The determinants of spatial receptive fields in azimuth. *Journal of Neuroscience*, 22(4). <https://doi.org/10.1523/jneurosci.22-04-01468.2002>
- Tritsch, N. X., & Bergles, D. E. (2010). Developmental regulation of spontaneous activity in the mammalian cochlea. *Journal of Neuroscience*, 30(4), 1539–1550. <https://doi.org/10.1523/JNEUROSCI.3875-09.2010>
- Tritsch, N. X., Yi, E., Gale, J. E., Glowatzki, E., & Bergles, D. E. (2007). The origin of spontaneous activity in the developing auditory system. *Nature*, 450(7166), 50–55. <https://doi.org/10.1038/nature06233>

- Van Beuningen, S. F. B., Will, L., Harterink, M., Chazeau, A., Van Battum, E. Y., Frias, C. P., Franker, M. A. M., Katrukha, E. A., Stucchi, R., Vocking, K., Antunes, A. T., Slenders, L., Doulkeridou, S., Sillevs Smitt, P., Altelaar, A. F. M., Post, J. A., Akhmanova, A., Pasterkamp, R. J., Kapitein, L. C., ... Hoogenraad, C. C. (2015). TRIM46 Controls Neuronal Polarity and Axon Specification by Driving the Formation of Parallel Microtubule Arrays. *Neuron*. <https://doi.org/10.1016/j.neuron.2015.11.012>
- vanderHeijden, M., Lorteije, J. A. M., Plauška, A., Roberts, M. T., Golding, N. L., & Borst, J. G. G. (2013). Directional hearing by linear summation of binaural inputs at the medial superior olive. *Neuron*, 78(5), 936–948. <https://doi.org/10.1016/j.neuron.2013.04.028>
- Vitriol, E. A., Zheng, J. Q., Aizawa, H., Wakatsuki, S., Ishii, A., Moriyama, K., Sasaki, Y., Ohashi, K., Sekine-Aizawa, Y., Sehara-Fujisawa, A., Mizuno, K., Goshima, Y., Yahara, I., Akin, O., Mullins, R. D., Andrianantoandro, E., Pollard, T. D., Arakawa, Y., Bito, H., ... Ginty, D. D. (2012). Growth cone travel in space and time: the cellular ensemble of cytoskeleton, adhesion, and membrane. *Neuron*, 73(6), 1068–1081. <https://doi.org/10.1016/j.neuron.2012.03.005>
- Wefelmeyer, W., Cattaert, D., & Burrone, J. (2015). Activity-dependent mismatch between axo-axonic synapses and the axon initial segment controls neuronal output. *Proceedings of the National Academy of Sciences*, 112(31). <https://doi.org/10.1073/pnas.1502902112>
- Werner, L. A., & Gray, L. (1998). *Behavioral Studies of Hearing Development*. https://doi.org/10.1007/978-1-4612-2186-9_2
- Yang, Y., Ogawa, Y., Hedstrom, K. L., Rasband, M. N., Babcock, H. P., Bennett, V., Zhuang, X., Yamaguchi, K., Fujiwara, T., & Kusumi, A. (2007). β IV spectrin is recruited to axon initial segments and nodes of Ranvier by ankyrinG. *The Journal of Cell Biology*, 176(4), 509–519. <https://doi.org/10.1083/jcb.200610128>
- Zhong, G., He, J., Zhou, R., Lorenzo, D., Babcock, H. P., Bennett, V., & Zhuang, X. (2014). Developmental mechanism of the periodic membrane skeleton in axons. *ELife*. <https://doi.org/10.7554/eLife.04581>

CHAPTER 2 REFERENCES

- Adachi, R., Yamada, R., & Kuba, H. (2015). Plasticity of the axonal trigger zone. *The Neuroscientist: A Review Journal Bringing Neurobiology, Neurology and Psychiatry*, 21(3). <https://doi.org/10.1177/1073858414535986>

- Colbert, C. M., & Johnston, D. (1996). Axonal action-potential initiation and Na⁺ channel densities in the soma and axon initial segment of subicular pyramidal neurons. *The Journal of Neuroscience : The Official Journal of the Society for Neuroscience*, 16(21), 6676–6686. <http://www.ncbi.nlm.nih.gov/pubmed/8824308>
- Evans, M. D., Dumitrescu, A. S., Kruijssen, D. L. H., Taylor, S. E., & Grubb, M. S. (2015). Rapid Modulation of Axon Initial Segment Length Influences Repetitive Spike Firing. *Cell Reports*, 13(6). <https://doi.org/10.1016/j.celrep.2015.09.066>
- French, C. R., Sah, P., Buckett, K. J., & Gage, P. W. (1990). A voltage-dependent persistent sodium current in mammalian hippocampal neurons. *The Journal of General Physiology*, 95(6), 1139–1157. <https://doi.org/10.1085/JGP.95.6.1139>
- Fukaya, R., Yamada, R., & Kuba, H. (2017). Tonal variation of the T-type Ca²⁺ current in avian auditory coincidence detector neurons. *The Journal of Neuroscience : The Official Journal of the Society for Neuroscience*, 2237–17. <https://doi.org/10.1523/JNEUROSCI.2237-17.2017>
- González-Cabrera, C., Meza, R., Ulloa, L., Merino-Sepúlveda, P., Luco, V., Sanhueza, A., Oñate-Ponce, A., Bolam, J. P., & Henny, P. (2017). Characterization of the axon initial segment of mice substantia nigra dopaminergic neurons. *Journal of Comparative Neurology*, 525(16), 3529–3542. <https://doi.org/10.1002/cne.24288>
- Hu, H., & Jonas, P. (2014). A supercritical density of Na⁺ channels ensures fast signaling in GABAergic interneuron axons. *Nature Neuroscience*, 17(5). <https://doi.org/10.1038/nn.3678>
- Park, Y. Y., Johnston, D., & Gray, R. (2013). Slowly inactivating component of Na⁺ current in peri-somatic region of hippocampal CA1 pyramidal neurons. *Journal of Neurophysiology*, 109(5), 1378–1390. <https://doi.org/10.1152/jn.00435.2012>
- Raman, I. M., Sprunger, L. K., Meisler, M. H., & Bean, B. P. (1997). Altered Subthreshold Sodium Currents and Disrupted Firing Patterns in Purkinje Neurons of Scn8a Mutant Mice. *Neuron*, 19(4), 881–891. [https://doi.org/10.1016/S0896-6273\(00\)80969-1](https://doi.org/10.1016/S0896-6273(00)80969-1)
- Scott, L. L., Mathews, P. J., & Golding, N. L. (2010). Perisomatic voltage-gated sodium channels actively maintain linear synaptic integration in principal neurons of the medial superior olive. *The Journal of Neuroscience : The Official Journal of the Society for Neuroscience*, 30(6), 2039–2050. <https://doi.org/10.1523/JNEUROSCI.2385-09.2010>
- Sekerli, M., Del Negro, C. A., Lee, R. H., & Butera, R. J. (2004). Estimating action potential thresholds from neuronal time-series: New metrics and evaluation of methodologies. *IEEE Transactions on Biomedical Engineering*, 51(9). <https://doi.org/10.1109/TBME.2004.827531>
- Shu, Y., Yu, Y., Yang, J., & McCormick, D. A. (2007). Selective control of cortical axonal spikes by a slowly inactivating K⁺ current. *Proceedings of the National Academy*

of Sciences of the United States of America, 104(27), 11453–11458.
<https://doi.org/10.1073/pnas.0702041104>

Yang, Y., Ramamurthy, B., Neef, A., & Xu-Friedman, M. A. (2016). Low Somatic Sodium Conductance Enhances Action Potential Precision in Time-Coding Auditory Neurons. *The Journal of Neuroscience: The Official Journal of the Society for Neuroscience*, 36(47), 11999–12009. <https://doi.org/10.1523/JNEUROSCI.1475-16.2016>

CHAPTER 3 REFERENCES

Barnes-Davies M, Barker MC, Osmani F, Forsythe ID (2004) Kv1 currents mediate a gradient of principal neuron excitability across the tonotopic axis in the rat lateral superior olive. *Eur J Neurosci* 19:325-333.

Batra R, Kuwada S, Fitzpatrick DC (1997) Sensitivity to interaural temporal disparities of low- and high-frequency neurons in the superior olivary complex. I. Heterogeneity of responses. *J Neurophysiol* 78:1222-1236.

Baumann VJ, Lehnert S, Leibold C, Koch U (2013) Tonotopic organization of the hyperpolarization-activated current (I_h) in the mammalian medial superior olive. *Front Neural Circuits* 7:117.

Bazwinsky-Wutschke I, Hartig W, Kretschmar R, Rubsamen R (2016) Differential morphology of the superior olivary complex of *Meriones unguiculatus* and *Monodelphis domestica* revealed by calcium-binding proteins. *Brain Struct Funct* 221:4505-4523.

Bernstein LR, Trahiotis C (1994) Detection of interaural delay in high-frequency sinusoidally amplitude-modulated tones, two-tone complexes, and bands of noise. *J Acoust Soc Am* 95:3561-3567.

Brand A, Behrend O, Marquardt T, McAlpine D, Grothe B (2002) Precise inhibition is essential for microsecond interaural time difference coding. *Nature* 417:543-547.

Brew HM, Forsythe ID (2005) Systematic variation of potassium current amplitudes across the tonotopic axis of the rat medial nucleus of the trapezoid body. *Hear Res* 206:116-132.

Carr CE, Konishi M (1988) Axonal delay lines for time measurement in the owl's brainstem. *Proc Natl Acad Sci U S A* 85:8311-8315.

Carr CE, Shah S, McColgan T, Ashida G, Kuokkanen PT, Brill S, Kempter R, Wagner H (2015) Maps of interaural delay in the owl's nucleus laminaris. *J Neurophysiol* 114:1862-1873.

- Chirila FV, Rowland KC, Thompson JM, Spirou GA (2007) Development of gerbil medial superior olive: integration of temporally delayed excitation and inhibition at physiological temperature. *J Physiol* 584:167-190.
- Dietz M, Marquardt T, Stange A, Pecka M, Grothe B, McAlpine D (2014) Emphasis of spatial cues in the temporal fine structure during the rising segments of amplitude-modulated sounds II: single-neuron recordings. *J Neurophysiol* 111:1973-1985.
- Fischer L, Leibold C, Felmy F (2018) Resonance Properties in Auditory Brainstem Neurons. *Front Cell Neurosci* 12:8.
- Fischl MJ, Burger RM, Schmidt-Pauly M, Alexandrova O, Sinclair JL, Grothe B, Forsythe ID, Kopp-Scheinflug C (2016) Physiology and anatomy of neurons in the medial superior olive of the mouse. *J Neurophysiol* 116:2676-2688.
- Franken TP, Joris PX, Smith PH (2018) Principal cells of the brainstem's interaural sound level detector are temporal differentiators rather than integrators. *Elife* 7.
- Franken TP, Roberts MT, Wei L, Golding NL, Joris PX (2015) In vivo coincidence detection in mammalian sound localization generates phase delays. *Nat Neurosci* 18:444-452.
- Frisina RD, Smith RL, Chamberlain SC (1990) Encoding of amplitude modulation in the gerbil cochlear nucleus: II. Possible neural mechanisms. *Hear Res* 44:123-141.
- Fukui I, Ohmori H (2004) Tonotopic gradients of membrane and synaptic properties for neurons of the chicken nucleus magnocellularis. *J Neurosci* 24:7514-7523.
- Gai Y, Doiron B, Rinzel J (2010) Slope-based stochastic resonance: how noise enables phasic neurons to encode slow signals. *PLoS Comput Biol* 6:e1000825.
- Garden DL, Dodson PD, O'Donnell C, White MD, Nolan MF (2008) Tuning of synaptic integration in the medial entorhinal cortex to the organization of grid cell firing fields. *Neuron* 60:875-889.
- Giocomo LM, Hussaini SA, Zheng F, Kandel ER, Moser MB, Moser EI (2011) Grid cells use HCN1 channels for spatial scaling. *Cell* 147:1159-1170.
- Goldberg JM, Brown PB (1969) Response of binaural neurons of dog superior olivary complex to dichotic tonal stimuli: some physiological mechanisms of sound localization. *J Neurophysiol* 32:613-636.
- Golding NL, Oertel D (2012) Synaptic integration in dendrites: exceptional need for speed. *J Physiol* 590:5563-5569.
- Grothe B, Sanes DH (1994) Synaptic inhibition influences the temporal coding properties of medial superior olivary neurons: an in vitro study. *J Neurosci* 14:1701-1709.
- Grothe B, Park TJ (1998) Sensitivity to interaural time differences in the medial superior olive of a small mammal, the Mexican free-tailed bat. *J Neurosci* 18:6608-6622.

- Grothe B, Pecka M (2014) The natural history of sound localization in mammals--a story of neuronal inhibition. *Front Neural Circuits* 8:116.
- Grothe B, Park TJ, Schuller G (1997) Medial superior olive in the free-tailed bat: response to pure tones and amplitude-modulated tones. *J Neurophysiol* 77:1553-1565.
- Henkel CK, Spangler KM (1983) Organization of the efferent projections of the medial superior olivary nucleus in the cat as revealed by HRP and autoradiographic tracing methods. *J Comp Neurol* 221:416-428.
- Hong H, Wang X, Lu T, Zorio DAR, Wang Y, Sanchez JT (2018) Diverse Intrinsic Properties Shape Functional Phenotype of Low-Frequency Neurons in the Auditory Brainstem. *Front Cell Neurosci* 12:175.
- Hu W, Tian C, Li T, Yang M, Hou H, Shu Y (2009) Distinct contributions of Na(v)1.6 and Na(v)1.2 in action potential initiation and backpropagation. *Nat Neurosci* 12:996-1002.
- Jeffress LA (1948) A place theory of sound localization. *J Comp Physiol Psychol* 41:35-39.
- Joris P, Yin TC (2007) A matter of time: internal delays in binaural processing. *Trends Neurosci* 30:70-78.
- Joris PX (1996) Envelope coding in the lateral superior olive. II. Characteristic delays and comparison with responses in the medial superior olive. *J Neurophysiol* 76:2137-2156.
- Joris PX, Yin TC (1995) Envelope coding in the lateral superior olive. I. Sensitivity to interaural time differences. *J Neurophysiol* 73:1043-1062.
- Karino S, Smith PH, Yin TC, Joris PX (2011) Axonal branching patterns as sources of delay in the mammalian auditory brainstem: a re-examination. *J Neurosci* 31:3016-3031.
- Khurana S, Remme MW, Rinzel J, Golding NL (2011) Dynamic interaction of I_h and $IK-LVA$ during trains of synaptic potentials in principal neurons of the medial superior olive. *J Neurosci* 31:8936-8947.
- Khurana S, Liu Z, Lewis AS, Rosa K, Chetkovich D, Golding NL (2012) An essential role for modulation of hyperpolarization-activated current in the development of binaural temporal precision. *J Neurosci* 32:2814-2823.
- Kim EJ, Feng C, Santamaria F, Kim JH (2019) Impact of Auditory Experience on the Structural Plasticity of the AIS in the Mouse Brainstem Throughout the Lifespan. *Front Cell Neurosci* 13:456.
- Ko KW, Rasband MN, Meseguer V, Kramer RH, Golding NL (2016) Serotonin modulates spike probability in the axon initial segment through HCN channels. *Nat Neurosci* 19:826-834.

- Koch U, Braun M, Kapfer C, Grothe B (2004) Distribution of HCN1 and HCN2 in rat auditory brainstem nuclei. *Eur J Neurosci* 20:79-91.
- Koppl C (1994) Auditory nerve terminals in the cochlear nucleus magnocellularis: differences between low and high frequencies. *J Comp Neurol* 339:438-446.
- Kuba H (2012) Structural tuning and plasticity of the axon initial segment in auditory neurons. *J Physiol* 590:5571-5579.
- Kuba H, Yamada R, Fukui I, Ohmori H (2005) Tonotopic specialization of auditory coincidence detection in nucleus laminaris of the chick. *J Neurosci* 25:1924-1934.
- Lehnert S, Ford MC, Alexandrova O, Hellmundt F, Felmy F, Grothe B, Leibold C (2014) Action potential generation in an anatomically constrained model of medial superior olive axons. *J Neurosci* 34:5370-5384.
- Mathews PJ, Jercog PE, Rinzel J, Scott LL, Golding NL (2010) Control of submillisecond synaptic timing in binaural coincidence detectors by K(v)1 channels. *Nat Neurosci* 13:601-609.
- McFadden D, Pasanen EG (1976) Lateralization of high frequencies based on interaural time differences. *J Acoust Soc Am* 59:634-639.
- Nuetzel JM, Hafter ER (1976) Lateralization of complex waveforms: effects of fine structure, amplitude, and duration. *J Acoust Soc Am* 60:1339-1346.
- Padmanabhan K, Urban NN (2010) Intrinsic biophysical diversity decorrelates neuronal firing while increasing information content. *Nat Neurosci* 13:1276-1282.
- Rautenberg PL, Grothe B, Felmy F (2009) Quantification of the three-dimensional morphology of coincidence detector neurons in the medial superior olive of gerbils during late postnatal development. *J Comp Neurol* 517:385-396.
- Remme MW, Donato R, Mikiel-Hunter J, Ballestero JA, Foster S, Rinzel J, McAlpine D (2014) Subthreshold resonance properties contribute to the efficient coding of auditory spatial cues. *Proc Natl Acad Sci U S A* 111:E2339-2348.
- Roberts MT, Seeman SC, Golding NL (2013) A mechanistic understanding of the role of feedforward inhibition in the mammalian sound localization circuitry. *Neuron* 78:923-935.
- Roberts RC, Ribak CE (1987) GABAergic neurons and axon terminals in the brainstem auditory nuclei of the gerbil. *J Comp Neurol* 258:267-280.
- Sanes DH, Goldstein NA, Ostad M, Hillman DE (1990) Dendritic morphology of central auditory neurons correlates with their tonotopic position. *J Comp Neurol* 294:443-454.
- Scheibel ME, Scheibel AB (1974) Neuropil organization in the superior olive of the cat. *Exp Neurol* 43:339-348.

- Scott LL, Mathews PJ, Golding NL (2005) Posthearing developmental refinement of temporal processing in principal neurons of the medial superior olive. *J Neurosci* 25:7887-7895.
- Scott LL, Hage TA, Golding NL (2007) Weak action potential backpropagation is associated with high-frequency axonal firing capability in principal neurons of the gerbil medial superior olive. *J Physiol* 583:647-661.
- Scott LL, Mathews PJ, Golding NL (2010) Perisomatic voltage-gated sodium channels actively maintain linear synaptic integration in principal neurons of the medial superior olive. *J Neurosci* 30:2039-2050.
- Smith DJ, Rubel EW (1979) Organization and development of brain stem auditory nuclei of the chicken: dendritic gradients in nucleus laminaris. *J Comp Neurol* 186:213-239.
- Smith PH (1995) Structural and functional differences distinguish principal from nonprincipal cells in the guinea pig MSO slice. *J Neurophysiol* 73:1653-1667.
- Spitzer MW, Semple MN (1995) Neurons sensitive to interaural phase disparity in gerbil superior olive: diverse monaural and temporal response properties. *J Neurophysiol* 73:1668-1690.
- Stotler WA (1953) An experimental study of the cells and connections of the superior olivary complex of the cat. *J Comp Neurol* 98:401-431.
- Svirskis G, Kotak V, Sanes DH, Rinzel J (2002) Enhancement of signal-to-noise ratio and phase locking for small inputs by a low-threshold outward current in auditory neurons. *J Neurosci* 22:11019-11025.
- Tripathy SJ, Padmanabhan K, Gerkin RC, Urban NN (2013) Intermediate intrinsic diversity enhances neural population coding. *Proc Natl Acad Sci U S A* 110:8248-8253.
- van Buuren S, Groothuis-Oudshoorn, K. (2001) Multivariate Imputation by Chained Equations in R. *Journal of Statistical Software* 45:1-67.
- Wang X, Hong H, Brown DH, Sanchez JT, Wang Y (2017) Distinct Neural Properties in the Low-Frequency Region of the Chicken Cochlear Nucleus Magnocellularis. *eNeuro* 4.
- Wentholt RJ, Huie D, Altschuler RA, Reeks KA (1987) Glycine immunoreactivity localized in the cochlear nucleus and superior olivary complex. *Neuroscience* 22:897-912.
- Yamada R, Kuba H, Ishii TM, Ohmori H (2005) Hyperpolarization-activated cyclic nucleotide-gated cation channels regulate auditory coincidence detection in nucleus laminaris of the chick. *J Neurosci* 25:8867-8877.

Yin TC, Chan JC (1990) Interaural time sensitivity in medial superior olive of cat. *J Neurophysiol* 64:465-488.

CHAPTER 4 REFERENCES

- Adams, J.C. (1981). Heavy metal intensification of DAB-based HRP reaction product. *J. Histochem. Cytochem.* 29, 775. DOI: <https://doi.org/10.1177/29.6.7252134>
- Agmon-Snir, H., Carr, C.E., and Rinzel, J. (1998). The role of dendrites in auditory coincidence detection. *Nature* 393, 268–272. DOI: <https://doi.org/10.1038/30505>
- Ashida, G., Tollin, D.J., Kretzberg, J. (2017). Physiological models of the lateral superior olive. *PLoS Comput. Biol.* 13, e1005903. <https://doi.org/10.1371/journal.pcbi.1005903>
- Balakrishnan, V., Becker, M., Löhrke, S., Nothwang, H.G., Güresir, E., and Friauf, E. (2003). Expression and function of chloride transporters during development of inhibitory neurotransmission in the auditory brainstem. *J. Neurosci.* 23: 4134-4145. DOI: <https://doi.org/10.1523/JNEUROSCI.23-10-04134.2003>
- Banks, M.I., Smith, P.H., 1992. Intracellular recordings from neurobiotin-labeled cells in brain slices of the rat medial nucleus of the trapezoid body. *J. Neurosci.* 12, 2819–2837. DOI: <https://doi.org/10.1523/JNEUROSCI.12-07-02819.1992>
- Beiderbeck, B., Myoga, M.H., Müller, N.I.C., Callan, A.R., Friauf, E., Grothe, B., and Pecka, M. (2018). Precisely timed inhibition facilitates action potential firing for spatial coding in the auditory brainstem. *Nat. Commun.* 9, 1771. DOI: <https://doi.org/10.1038/s41467-018-04210-y>
- Bender, K.J., and Trussell, L.O. (2012). The physiology of the axon initial segment. *Annu. Rev. Neurosci.* 35, 249–265. DOI: <https://doi.org/10.1146/annurev-neuro-062111-150339>
- Berlucchi, G. (1999). Some aspects of the history of the law of dynamic polarization of the neuron. From William James to Sherrington, from Cajal and van Gehuchten to Golgi. *J. Hist. Neurosci.* 8, 191–201. DOI: <https://doi.org/10.1076/jhin.8.2.191.1844>
- Blot, A., and Barbour, B. (2014). Ultra-rapid axon-axon ephaptic inhibition of cerebellar Purkinje cells by the pinceau. *Nat. Neurosci.* 17, 289–295. DOI: <https://doi.org/10.1038/nn.3624>
- Boyce, W.E., DiPrima, R.C., Meade, D.B. (2018). *Elementary Differential Equations and Boundary Value Problems*, 11th Edition. Wiley.
- Caird, D., and Klinke, R. (1983). Processing of binaural stimuli by cat superior olivary complex neurons. *Exp. Brain Res.* 52, 385–399. DOI: <https://doi.org/10.1007/BF00238032>

- Cant, N.B. (1991). Projections to the lateral and medial superior olivary nuclei from the spherical and globular bushy cells of the anteroventral cochlear nucleus, in: *Neurobiology of Hearing: The Central Auditory System*. Raven Press, New York, pp. 99–119.
- Clark, C. (2016). Locomotion-induced sounds and sonations: mechanisms, communication function, and relationship with behavior, in: *Vertebrate Sound Production and Acoustic Communication*. pp. 83–117.
- Colburn, H.S., Han, Y.A., and Culotta, C.P. (1990). Coincidence model of MSO responses. *Hear. Res.* 49, 335–346. DOI: [https://doi.org/10.1016/0378-5955\(90\)90112-3](https://doi.org/10.1016/0378-5955(90)90112-3)
- Domnitz, R.H., and Colburn, H.S. (1977). Lateral position and interaural discrimination. *J. Acoust. Soc. Am.* 61, 1586–1598. DOI: <https://doi.org/10.1121/1.381472>
- Doucet, J.R., and Ryugo, D.K. (2003). Axonal pathways to the lateral superior olive labeled with biotinylated dextran amine injections in the dorsal cochlear nucleus of rats. *J. Comp. Neurol.* 461, 452–465. DOI: <https://doi.org/10.1002/cne.10722>
- Ehrlich, I., Lohrke, S., and Friauf, E. (1999). Shift from depolarizing to hyperpolarizing glycine action in rat auditory neurones is due to age-dependent Cl⁻ regulation. *J. Physiol.* 520 Pt 1, 121-137. DOI: <https://doi.org/10.1111/j.1469-7793.1999.00121.x>
- Ewert, S.D., Kaiser, K., Kernschmidt, L., and Wiegrebe, L., 2012. Perceptual sensitivity to high frequency interaural time differences created by rustling sounds. *J. Assoc. Res. Otolaryngol.* 13, 131–143. <https://doi.org/10.1007/s10162-011-0303-2>
- Finlayson, P.G., and Caspary, D.M. (1989). Synaptic potentials of chinchilla lateral superior olivary neurons. *Hear. Res.* 38, 221–228. DOI: [https://doi.org/10.1016/0378-5955\(89\)90067-1](https://doi.org/10.1016/0378-5955(89)90067-1)
- Franken, T.P., Bremen, P., and Joris, P.X. (2014). Coincidence detection in the medial superior olive: mechanistic implications of an analysis of input spiking patterns. *Front. Neural Circuits* 8, 42. DOI: <https://doi.org/10.3389/fncir.2014.00042>
- Franken, T.P., Joris, P.X., and Smith, P.H. (2018). Principal cells of the brainstem’s interaural sound level detector are temporal differentiators rather than integrators. *eLife* 7, e33854. DOI: <https://doi.org/10.7554/eLife.33854>
- Franken, T.P., Roberts, M.T., Wei, L., Golding, N.L., and Joris, P.X. (2015). In vivo coincidence detection in mammalian sound localization generates phase delays. *Nat. Neurosci.* 18, 444–452. DOI: <https://doi.org/10.1038/nn.3948>
- Franken, T.P., Smith, P.H., and Joris, P.X. (2016). In vivo whole-cell recordings combined with electron microscopy reveal unexpected morphological and physiological properties in the lateral nucleus of the trapezoid body in the auditory brainstem. *Front. Neural Circuits* 10, 69. DOI: <https://doi.org/10.3389/fncir.2016.00069>

- Gaik, W. (1993). Combined evaluation of interaural time and intensity differences: psychoacoustic results and computer modeling. *J. Acoust. Soc. Am.* 94, 98–110. DOI: <https://doi.org/10.1121/1.406947>
- Galiano, M.R., Jha, S., Ho, T.S., Zhang, C., Ogawa, Y., Chang, K.J., Stankewich, M.C., Mohler, P.J., and Rasband, M.N. (2012). A distal axonal cytoskeleton forms an intra-axonal boundary that controls axon initial segment assembly. *Cell* 149:1125–1139. <https://doi.org/10.1016/j.cell.2012.03.039>
- Gentet, L.J., Stuart, G.J., Clements, J.D. (2000). Direct measurement of specific membrane capacitance in neurons. *Biophys. J.* 79, 314–320. [https://doi.org/10.1016/S0006-3495\(00\)76293-X](https://doi.org/10.1016/S0006-3495(00)76293-X)
- Gjoni, E., Aguet, C., Sahlender, D.A., Knott, G., and Schneggenburger, R. (2018a). Ultrastructural basis of strong unitary inhibition in a binaural neuron. *J. Physiol.* 596, 4969–4982. DOI: <https://doi.org/10.1113/JP276015>
- Gjoni, E., Zenke, F., Bouhours, B., and Schneggenburger, R. (2018b). Specific synaptic input strengths determine the computational properties of excitation-inhibition integration in a sound localization circuit. *J. Physiol.* 596, 4945–4967. DOI: <https://doi.org/10.1113/JP276012>
- Glendenning, K.K., Hutson, K.A., Nudo, R.J., and Masterton, R.B. (1985). Acoustic chiasm II: anatomical basis of binaurality in lateral superior olive of cat. *J Comp Neurol* 232, 261–285. DOI: <https://doi.org/10.1002/cne.902320210>
- Goerlitz, H.R., Siemers, B.M. (2007). Sensory ecology of prey rustling sounds: acoustical features and their classification by wild Grey Mouse Lemurs. *Funct. Ecol.* 21, 143–153. <https://doi.org/10.1111/j.1365-2435.2006.01212.x>
- Goldberg, J.M., and Brown, P.B. (1969). Response of binaural neurons of dog superior olivary complex to dichotic tonal stimuli: some physiological mechanisms of sound localization. *J. Neurophysiol.* 32, 613–636. DOI: <https://doi.org/10.1152/jn.1969.32.4.613>
- Goldwyn, J.H., Remme, M.W.H., Rinzel, J. (2019). Soma-axon coupling configurations that enhance neuronal coincidence detection. *PLoS Comput. Biol.* 15, e1006476. <https://doi.org/10.1371/journal.pcbi.1006476>
- Gómez-Álvarez, M., Saldaña, E. (2016). Different tonotopic regions of the lateral superior olive receive a similar combination of afferent inputs. *J. Comp. Neurol.* 524, 2230–2250. <https://doi.org/10.1002/cne.23942>
- Hancock, K.E., Noel, V., Ryugo, D.K., and Delgutte, B. (2010). Neural coding of interaural time differences with bilateral cochlear implants: effects of congenital deafness. *J.*

- Neurosci. 30, 14068–14079. DOI: <https://doi.org/10.1523/JNEUROSCI.3213-10.2010>
- Helfert, R.H., and Schwartz, I.R. (1987). Morphological features of five neuronal classes in the gerbil lateral superior olive. *Am. J. Anat.* 179, 55–69. DOI: <https://doi.org/10.1002/aja.1001790108>
- Irvine, D.R.F., Park, V.N., and McCormick, L. (2001). Mechanisms underlying the sensitivity of neurons in the lateral superior olive to interaural intensity differences. *J. Neurophysiol.* 86, 2647–2666. DOI: <https://doi.org/10.1152/jn.2001.86.6.2647>
- Jeffress, L.A. (1948). A place theory of sound localization. *J. Comp. Physiol. Psychol.* 41, 35–39. DOI: <https://doi.org/10.1037/h0061495>
- Joris, P.X. (1996). Envelope coding in the lateral superior olive. II. Characteristic delays and comparison with responses in the medial superior olive. *J. Neurophysiol.* 76, 2137–2156. DOI: <https://doi.org/10.1152/jn.1996.76.4.2137>
- Joris, P.X., and Trussell, L.O. (2018). The calyx of Held: a hypothesis on the need for reliable timing in an intensity-difference encoder. *Neuron* 100, 534–549. DOI: <https://doi.org/10.1016/j.neuron.2018.10.026>
- Joris, P.X., and van der Heijden, M. (2019). Early binaural hearing: the comparison of temporal differences at the two ears. *Annu. Rev. Neurosci.* 42, 433–457. DOI: <https://doi.org/10.1146/annurev-neuro-080317-061925>
- Joris, P.X., and Yin, T.C. (1998). Envelope coding in the lateral superior olive. III. Comparison with afferent pathways. *J. Neurophysiol.* 79, 253–269. DOI: <https://doi.org/10.1152/jn.1998.79.1.253>
- Joris, P.X., and Yin, T.C. (1995). Envelope coding in the lateral superior olive. I. Sensitivity to interaural time differences. *J. Neurophysiol.* 73, 1043–1062. DOI: <https://doi.org/10.1152/jn.1995.73.3.1043>
- Kakazu, Y., Akaike, N., Komiyama, S., and Nabekura, J. (1999). Regulation of intracellular chloride by cotransporters in developing lateral superior olive neurons. *J. Neurosci.* 19: 2843–2851. DOI: <https://doi.org/10.1523/JNEUROSCI.19-08-02843.1999>
- Kapfer, C., Seidl, A.H., Schweizer, H., and Grothe, B. (2002). Experience-dependent refinement of inhibitory inputs to auditory coincidence-detector neurons. *Nat Neurosci* 5, 247–53. <https://doi.org/10.1038/nn810>
- Klumpp, R., and Eady, H. (1956). Some measurements of interaural time differences thresholds. *J. Acoust. Soc. Am.* 28, 859–864. DOI: <https://doi.org/10.1121/1.1908493>
- Koch C., Poggio T. and Torre V. (1982). Retinal ganglion cells: a functional interpretation of dendritic morphology. *Phil. Trans. R. Soc. Lond. B* 298: 227–263.

- Kole, M.H., and Brette, R. (2018). The electrical significance of axon location diversity. *Curr. Opin. Neurobiol.* *51*, 52–59. DOI: <https://doi.org/10.1016/j.conb.2018.02.016>
- Kullmann, P.H., and Kandler, K. (2001). Glycinergic/GABAergic synapses in the lateral superior olive are excitatory in neonatal C57Bl/6J mice. *Brain Res Dev Brain Res.* *131*, 143-147. DOI: [https://doi.org/10.1016/s0165-3806\(01\)00271-1](https://doi.org/10.1016/s0165-3806(01)00271-1)
- Leterrier, C. (2018). The axon initial segment: an updated viewpoint. *J. Neurosci.* *38*, 2135–2145. DOI: <https://doi.org/10.1523/JNEUROSCI.1922-17.2018>
- Maki, K., and Furukawa, S. (2005). Acoustical cues for sound localization by the Mongolian gerbil, *Meriones unguiculatus*. *J. Acoust. Soc. Am.* *118*, 872–886. DOI: <https://doi.org/10.1121/1.1944647>
- Michelet, P., Kovacic, D., Mc Laughlin, M., and Joris, P.X. (2010). Time-intensity trading: ongoing temporal coding of broadband noise in the auditory nerve as a function of intensity. *Assoc Res Otolaryngol Abs* *33*, 257. https://aro.org/wp-content/uploads/2020/02/2010_Abstract_Book_REV.pdf
- Nathanson, A.J., Davies, P.A., and Moss, S.J. (2019). Inhibitory synapse formation at the axon initial segment. *Front. Mol. Neurosci.* *12*, 266. DOI: <https://doi.org/10.3389/fnmol.2019.00266>
- Newcombe, R.G. (2006a). Confidence intervals for an effect size measure based on the Mann-Whitney statistic. Part 1: general issues and tail-area-based methods. *Stat. Med.* *25*, 543–557. DOI: <https://doi.org/10.1002/sim.2323>
- Newcombe, R.G. (2006b). Confidence intervals for an effect size measure based on the Mann-Whitney statistic. Part 2: asymptotic methods and evaluation. *Stat. Med.* *25*, 559–573. DOI: <https://doi.org/10.1002/sim.2324>
- Pan-Vazquez, A., Wefelmeyer, W., Gonzalez Sabater, V., Neves, G., and Burrone, J. (2020). Activity-dependent plasticity of axo-axonic synapses at the axon initial segment. *Neuron* *106*, 265-276.e6. <https://doi.org/10.1016/j.neuron.2020.01.037>
- Park, T.J., Grothe, B., Pollak, G.D., Schuller, G., and Koch, U. (1996). Neural delays shape selectivity to interaural intensity differences in the lateral superior olive. *J. Neurosci.* *16*, 6554–6566. DOI: <https://doi.org/10.1523/JNEUROSCI.16-20-06554.1996>
- Pollak, G.D. (1988). Time is traded for intensity in the bat's auditory system. *Hear. Res.* *36*, 107–124. DOI: [https://doi.org/10.1016/0378-5955\(88\)90054-8](https://doi.org/10.1016/0378-5955(88)90054-8)
- Roche, B.E., Schulte-Hostedde, A.I., Brooks, R.J. (1999). Route Choice by Deer Mice (*Peromyscus maniculatus*): Reducing the Risk of Auditory Detection by Predators. *Am. Midl. Nat.* *142*, 194–197. [https://doi.org/10.1674/0003-0031\(1999\)142\[0194:RCBDMP\]2.0.CO;2](https://doi.org/10.1674/0003-0031(1999)142[0194:RCBDMP]2.0.CO;2)

- Saint Marie, R.L., Ostapoff, E.M., Morest, D.K., and Wenthold, R.J., (1989). Glycine-immunoreactive projection of the cat lateral superior olive: possible role in midbrain ear dominance. *J. Comp. Neurol.* 279, 382–396. <https://doi.org/10.1002/cne.902790305>
- Sanes, D.H., Geary, W.A., Wooten, G.F., and Rubel, E.W. (1987). Quantitative distribution of the glycine receptor in the auditory brain stem of the gerbil. *J. Neurosci.* 7, 3793–3802. DOI: <https://doi.org/10.1523/JNEUROSCI.07-11-03793.1987>
- Sanes, D.H. (1990). An in vitro analysis of sound localization mechanisms in the gerbil lateral superior olive. *J. Neurosci.* 10, 3494–3506. DOI: <https://doi.org/10.1523/JNEUROSCI.10-11-03494.1990>
- Shepherd, G.M. (1991). *Foundations of the Neuron Doctrine* (New York: Oxford University Press). ISBN: 9780190259389
- Siemers, B.M., Goerlitz, H.R., Robsomanitrndrasana, E., Piep, M., Ramanamanjato, J.-B., Rakotondravony, D., Ramilijaona, O., Ganzhorn, J.U. (2007). Sensory basis of food detection in wild *Microcebus murinus*. *Int. J. Primatol.* 28, 291. <https://doi.org/10.1007/s10764-007-9135-7>
- Smith, P.H., Joris, P.X., and Yin, T.C. (1998). Anatomy and physiology of principal cells of the medial nucleus of the trapezoid body (MNTB) of the cat. *J. Neurophysiol.* 79, 3127–3142. DOI: <https://doi.org/10.1152/jn.1998.79.6.3127>
- Smith, P.H., Manning, K.A., and Uhrich, D.J. (2010). Evaluation of inputs to rat primary auditory cortex from the supragenulate nucleus and extrastriate visual cortex. *J. Comp. Neurol.* 518, 3679–3700. DOI: <https://doi.org/10.1002/cne.22411>
- Smith, P.H., Massie, A., and Joris, P.X. (2005). Acoustic stria: anatomy of physiologically characterized cells and their axonal projection patterns. *J. Comp. Neurol.* 482, 349–371. DOI: <https://doi.org/10.1002/cne.20407>
- Strutt, J. W. (1907). On our perception of sound direction. *Philos. Mag.* 13, 214–232. DOI: <https://doi.org/10.1080/14786440709463595>
- Tollin, D.J., and Yin, T.C.T. (2005). Interaural phase and level difference sensitivity in low-frequency neurons in the lateral superior olive. *J. Neurosci.* 25, 10648–10657. DOI: <https://doi.org/10.1523/JNEUROSCI.1609-05.2005>
- Tollin, D.J., and Yin, T.C.T. (2002). The coding of spatial location by single units in the lateral superior olive of the cat. II. The determinants of spatial receptive fields in azimuth. *J. Neurosci.* 22, 1468–1479. DOI: <https://doi.org/10.1523/JNEUROSCI.22-04-01468.2002>
- Tollin, D.J. (2003). The lateral superior olive: a functional role in sound source localization. *The Neuroscientist* 9, 127–143. DOI: <https://doi.org/10.1177/1073858403252228>

- Walcher, J., Hassfurth, B., Grothe, B., and Koch, U. (2011). Comparative posthearing development of inhibitory inputs to the lateral superior olive in gerbils and mice. *J. Neurophysiol.* *106*, 1443–1453. DOI: <https://doi.org/10.1152/jn.01087.2010>
- Wang, L., Colburn, H.S. (2012). A modeling study of the responses of the lateral superior olive to ipsilateral sinusoidally amplitude-modulated tones. *J. Assoc. Res. Otolaryngol. JARO* *13*, 249–267. <https://doi.org/10.1007/s10162-011-0300-5>
- Wang, Y., Zhang, P., and Wyskiel, D.R. (2016). Chandelier cells in functional and dysfunctional neural circuits. *Front. Neural Circuits* *10*, 33. DOI: <https://doi.org/10.3389/fncir.2016.00033>
- Woodruff, A.R., Anderson, S.A., Yuste, R., 2010. The enigmatic function of chandelier cells. *Front. Neurosci.* *4*, 201. <https://doi.org/10.3389/fnins.2010.00201>
- Wu, S.H., and Kelly, J.B. (1992). Binaural interaction in the lateral superior olive: time difference sensitivity studied in mouse brain slice. *J. Neurophysiol.* *68*, 1151–1159. DOI: <https://doi.org/10.1152/jn.1992.68.4.1151>
- Yang, Y., Adowski, T., Ramamurthy, B., Neef, A., and Xu-Friedman, M.A. (2015). High-speed dynamic-clamp interface. *J. Neurophysiol.* *113*, 2713–2720. DOI: <https://doi.org/10.1152/jn.00543.2014>
- Yin, T.C., and Chan, J.C. (1990). Interaural time sensitivity in medial superior olive of cat. *J. Neurophysiol.* *64*, 465–488. DOI: <https://doi.org/10.1152/jn.1990.64.2.465>
- Yin, T.C., Hirsch, J.A., and Chan, J.C. (1985). Responses of neurons in the cat's superior colliculus to acoustic stimuli. II. A model of interaural intensity sensitivity. *J. Neurophysiol.* *53*, 746–758. DOI: <https://doi.org/10.1152/jn.1985.53.3.746>
- Yin, T.C.T., Smith, P.H., Joris, P.X., 2019. Neural mechanisms of binaural processing in the auditory brainstem. *Compr. Physiol.* *9*, 1503–1575. <https://doi.org/10.1002/cphy.c180036>
- Yost, W.A., and Dye, R.H., Jr. (1988). Discrimination of interaural differences of level as a function of frequency. *J. Acoust. Soc. Am.* *83*, 1846–1851. DOI: <https://doi.org/10.1121/1.396520>

CHAPTER 5 REFERENCES

- Akil, O., Seal, R. P., Burke, K., Wang, C., Alemi, A., During, M., Edwards, R. H., & Lustig, L. R. (2012). Restoration of Hearing in the VGLUT3 Knockout Mouse Using Virally Mediated Gene Therapy. *Neuron*, *75*(2). <https://doi.org/10.1016/j.neuron.2012.05.019>

- Armstrong, C. M., & Hille, B. (1998). Voltage-gated ion channels and electrical excitability. *Neuron*, 20(3), 371–380. <http://www.ncbi.nlm.nih.gov/pubmed/9539115>
- Arons, B. (1992). A Review of The Cocktail Party Effect. *Journal of the American Voice I/O Society*, 12.
- Ashmead, D. H., Davis, D. F. L., Whalen, T., & Odom, R. D. (1991). Sound Localization and Sensitivity to Interaural Time Differences in Human Infants. *Child Development*, 62(6). <https://doi.org/10.1111/j.1467-8624.1991.tb01601.x>
- Babola, T. A., Li, S., Gribizis, A., Lee, B. J., Issa, J. B., Wang, H. C., Crair, M. C., & Bergles, D. E. (2018). Homeostatic Control of Spontaneous Activity in the Developing Auditory System. *Neuron*, 99(3). <https://doi.org/10.1016/j.neuron.2018.07.004>
- Bondy, B. J., Haimes, D. B., & Golding, N. L. (2021). Physiological diversity influences detection of stimulus envelope and fine structure in neurons of the medial superior olive. *The Journal of Neuroscience*. <https://doi.org/10.1523/jneurosci.2354-20.2021>
- Brand, A., Behrend, O., Marquardt, T., McAlpine, D., & Grothe, B. (2002). Precise inhibition is essential for microsecond interaural time difference coding. *Nature*, 417(6888), 543–547. <https://doi.org/10.1038/417543a>
- Cadwell, C. R., Palasantza, A., Jiang, X., Berens, P., Deng, Q., Yilmaz, M., Reimer, J., Shen, S., Bethge, M., Tolias, K. F., Sandberg, R., & Tolias, A. S. (2016). Electrophysiological, transcriptomic and morphologic profiling of single neurons using Patch-seq. *Nature Biotechnology*, 34(2), 199–203. <https://doi.org/10.1038/nbt.3445>
- Cadwell, C. R., Scala, F., Li, S., Livrizzi, G., Shen, S., Sandberg, R., Jiang, X., & Tolias, A. S. (2017). Multimodal profiling of single-cell morphology, electrophysiology, and gene expression using Patch-seq. *Nature Protocols*, 12(12), 2531–2553. <https://doi.org/10.1038/nprot.2017.120>
- Chirila, F. V., Rowland, K. C., Thompson, J. M., & Spirou, G. A. (2007). Development of gerbil medial superior olive: integration of temporally delayed excitation and inhibition at physiological temperature. *The Journal of Physiology*, 584(1), 167–190. <https://doi.org/10.1113/jphysiol.2007.137976>
- Clause, A., Sturm, J., Altieri, S. C., Maricich, S. M., & Kandler, K. (2014). Development of Mammalian Primary Sound Localization Circuits. In *Development of Auditory and Vestibular Systems: Fourth Edition* (pp. 249–285). Elsevier Inc. <https://doi.org/10.1016/B978-0-12-408088-1.00009-9>
- Deng, G. F., Qin, J. M., Sun, X. S., Kuang, Z. Y., Su, T., Zhao, Q. H., Shi, Y. W., Liu, X. R., Yu, M. J., Yi, Y. H., Liao, W. P., & Long, Y. S. (2011). Promoter analysis of mouse Scn3a gene and regulation of the promoter activity by GC box and CpG

- methylation. *Journal of Molecular Neuroscience*, 44(2).
<https://doi.org/10.1007/s12031-011-9492-8>
- Di Guilmi, M. N., & Rodríguez-Contreras, A. (2021). Characterization of Developmental Changes in Spontaneous Electrical Activity of Medial Superior Olivary Neurons Before Hearing Onset With a Combination of Injectable and Volatile Anesthesia. *Frontiers in Neuroscience*, 15. <https://doi.org/10.3389/fnins.2021.654479>
- Ehmann, H., Hartwich, H., Salzig, C., Hartmann, N., Clément-Ziza, M., Ushakov, K., Avraham, K. B., Bininda-Emonds, O. R. P., Hartmann, A. K., Lang, P., Friauf, E., & Nothwang, H. G. (2013). Time-dependent gene expression analysis of the developing superior olivary complex. *The Journal of Biological Chemistry*, 288(36), 25865–25879. <https://doi.org/10.1074/jbc.M113.490508>
- Gazina, E. V., Richards, K. L., Mokhtar, M. B. C., Thomas, E. A., Reid, C. A., & Petrou, S. (2010). Differential expression of exon 5 splice variants of sodium channel α subunit mRNAs in the developing mouse brain. *Neuroscience*, 166(1), 195–200. <https://doi.org/10.1016/J.NEUROSCIENCE.2009.12.011>
- Gillespie, D. C., Kim, G., & Kandler, K. (2005). Inhibitory synapses in the developing auditory system are glutamatergic. *Nature Neuroscience*, 8(3). <https://doi.org/10.1038/nn1397>
- Goldberg, J. M., & Brown, P. B. (1969). Response of binaural neurons of dog superior olivary complex to dichotic tonal stimuli: some physiological mechanisms of sound localization. *Journal of Neurophysiology*, 32(4). <https://doi.org/10.1152/jn.1969.32.4.613>
- Hancock, K. E., Noel, V., Ryugo, D. K., & Delgutte, B. (2010). Neural coding of interaural time differences with bilateral cochlear implants: Effects of congenital deafness. *Journal of Neuroscience*, 30(42). <https://doi.org/10.1523/JNEUROSCI.3213-10.2010>
- Hao, Y., Hao, S., Andersen-Nissen, E., Mauck, W. M., Zheng, S., Butler, A., Lee, M. J., Wilk, A. J., Darby, C., Zager, M., Hoffman, P., Stoeckius, M., Papalex, E., Mimitou, E. P., Jain, J., Srivastava, A., Stuart, T., Fleming, L. M., Yeung, B., ... Satija, R. (2021). Integrated analysis of multimodal single-cell data. *Cell*, 184(13). <https://doi.org/10.1016/j.cell.2021.04.048>
- Hardie, N. A., & Shepherd, R. K. (1999). Sensorineural hearing loss during development: morphological and physiological response of the cochlea and auditory brainstem. *Hearing Research*, 128(1–2), 147–165. [https://doi.org/10.1016/S0378-5955\(98\)00209-3](https://doi.org/10.1016/S0378-5955(98)00209-3)
- Kandler, K., Clause, A., & Noh, J. (2009). Tonotopic reorganization of developing auditory brainstem circuits. *Nature Neuroscience*, 12(6), 711–717. <https://doi.org/10.1038/nn.2332>

- Kapfer, C., Seidl, A. H., Schweizer, H., & Grothe, B. (2002). Experience-dependent refinement of inhibitory inputs to auditory coincidence-detector neurons. *Nature Neuroscience*, 5(3), 247–253. <https://doi.org/10.1038/nn810>
- Kelly, J. B., Judge, P. W., & Fraser, I. H. (1987). Development of the auditory orientation response in the albino rat (*Rattus norvegicus*). *Journal of Comparative Psychology (Washington, D.C. : 1983)*, 101(1). <https://doi.org/10.1037/0735-7036.101.1.60>
- Khurana, S., Remme, M. W. H., Rinzel, J., & Golding, N. L. (2011). Dynamic Interaction of Ih and IK-LVA during Trains of Synaptic Potentials in Principal Neurons of the Medial Superior Olive. *Journal of Neuroscience*, 31(24), 8936–8947. <https://doi.org/10.1523/JNEUROSCI.1079-11.2011>
- Khurana, Sukant, Liu, Z., Lewis, A. S., Rosa, K., Chetkovich, D., & Golding, N. L. (2012). An essential role for modulation of hyperpolarization-activated current in the development of binaural temporal precision. *The Journal of Neuroscience : The Official Journal of the Society for Neuroscience*, 32(8), 2814–2823. <https://doi.org/10.1523/JNEUROSCI.3882-11.2012>
- Lai, H. C., & Jan, L. Y. (2006). The distribution and targeting of neuronal voltage-gated ion channels. *Nature Reviews Neuroscience*, 7(7), 548–562. <https://doi.org/10.1038/nrn1938>
- Liao, Y., Smyth, G. K., & Shi, W. (2014). FeatureCounts: An efficient general purpose program for assigning sequence reads to genomic features. *Bioinformatics*, 30(7). <https://doi.org/10.1093/bioinformatics/btt656>
- Lippe, W. R. (1994). Rhythmic spontaneous activity in the developing avian auditory system. *Journal of Neuroscience*, 14(3 II). <https://doi.org/10.1523/jneurosci.14-03-01486.1994>
- Litovsky, R. Y., & Gordon, K. (2016). Bilateral cochlear implants in children: Effects of auditory experience and deprivation on auditory perception. In *Hearing Research* (Vol. 338, pp. 76–87). Elsevier B.V. <https://doi.org/10.1016/j.heares.2016.01.003>
- Lohmann And B C M, C., & Friauf, A. R. D. (1996). Distribution of the Calcium-Binding Proteins Parvalbumin and Calretinin in the Auditory Brainstem of Adult and Developing Rats. In *THE JOURNAL OF COMPARATIVE NEUROLOGY* (Vol. 367).
- Lun, A. T. L., Calero-Nieto, F. J., Haim-Vilmovsky, L., Göttgens, B., & Marioni, J. C. (2017). Assessing the reliability of spike-in normalization for analyses of single-cell RNA sequencing data. *Genome Research*, 27(11). <https://doi.org/10.1101/gr.222877.117>
- Macica, C. M., von Hehn, C. A. A., Wang, L.-Y., Ho, C.-S., Yokoyama, S., Joho, R. H., & Kaczmarek, L. K. (2003). Modulation of the kv3.1b potassium channel isoform adjusts the fidelity of the firing pattern of auditory neurons. *The Journal of*

- Neuroscience : The Official Journal of the Society for Neuroscience*, 23(4), 1133–1141. <http://www.ncbi.nlm.nih.gov/pubmed/12598601>
- Magnusson, A. K., Kapfer, C., Grothe, B., & Koch, U. (2005). Maturation of glycinergic inhibition in the gerbil medial superior olive after hearing onset. *The Journal of Physiology*, 568(2), 497–512. <https://doi.org/10.1113/jphysiol.2005.094763>
- Martin, M. (2011). Cutadapt removes adapter sequences from high-throughput sequencing reads. *EMBnet.Journal*, 17(1). <https://doi.org/10.14806/ej.17.1.200>
- Mathews, P. J., Jercog, P. E., Rinzel, J., Scott, L. L., & Golding, N. L. (2010). Control of submillisecond synaptic timing in binaural coincidence detectors by Kv1 channels. *Nature Neuroscience*, 13(5), 601–609. <https://doi.org/10.1038/nn.2530>
- Mourot, A., Fehrentz, T., Le Feuvre, Y., Smith, C. M., Herold, C., Dalkara, D., Nagy, F., Trauner, D., & Kramer, R. H. (2012). Rapid optical control of nociception with an ion-channel photoswitch. *Nature Methods*, 9(4), 396–402. <https://doi.org/10.1038/nmeth.1897>
- O’Neil, J. N., Connelly, C. J., Limb, C. J., & Ryugo, D. K. (2011). Synaptic morphology and the influence of auditory experience. In *Hearing Research* (Vol. 279, Issues 1–2). <https://doi.org/10.1016/j.heares.2011.01.019>
- Plummer, N. W., & Meisler, M. H. (1999). Evolution and diversity of mammalian sodium channel genes. *Genomics*, 57. <https://doi.org/10.1006/geno.1998.5735>
- Pollack, I., & Pickett, J. M. (1957). Cocktail Party Effect. *The Journal of the Acoustical Society of America*, 29(11). <https://doi.org/10.1121/1.1919140>
- Puri, B. K. (2020). Calcium Signaling and Gene Expression. In *Advances in Experimental Medicine and Biology* (Vol. 1131, pp. 537–545). Springer New York LLC. https://doi.org/10.1007/978-3-030-12457-1_22
- Royeck, M., Horstmann, M.-T., Remy, S., Reitze, M., Yaari, Y., & Beck, H. (2008). Role of axonal NaV1.6 sodium channels in action potential initiation of CA1 pyramidal neurons. *Journal of Neurophysiology*. <https://doi.org/10.1152/jn.90332.2008>
- Rubel, E. W., & Fritzsche, B. (2002). Auditory System Development: Primary Auditory Neurons and Their Targets. *Annual Review of Neuroscience*, 25(1), 51–101. <https://doi.org/10.1146/annurev.neuro.25.112701.142849>
- Russell, F. A., & Moore, D. R. (1999). Effects of unilateral cochlear removal on dendrites in the gerbil medial superior olivary nucleus. *European Journal of Neuroscience*, 11(4), 1379–1390. <https://doi.org/10.1046/j.1460-9568.1999.00547.x>
- Ryugo, D. (2015). Auditory neuroplasticity, hearing loss and cochlear implants. In *Cell and Tissue Research* (Vol. 361, Issue 1). <https://doi.org/10.1007/s00441-014-2004-8>

- Scott, L. L., Mathews, P. J., & Golding, N. L. (2005). Posthearing developmental refinement of temporal processing in principal neurons of the medial superior olive. *The Journal of Neuroscience : The Official Journal of the Society for Neuroscience*, 25(35), 7887–7895. <https://doi.org/10.1523/JNEUROSCI.1016-05.2005>
- Seidl, A. H., & Grothe, B. (2005). Development of Sound Localization Mechanisms in the Mongolian Gerbil Is Shaped by Early Acoustic Experience. *Journal of Neurophysiology*, 94(2), 1028–1036. <https://doi.org/10.1152/jn.01143.2004>
- Sekerli, M., Del Negro, C. A., Lee, R. H., & Butera, R. J. (2004). Estimating action potential thresholds from neuronal time-series: New metrics and evaluation of methodologies. *IEEE Transactions on Biomedical Engineering*, 51(9). <https://doi.org/10.1109/TBME.2004.827531>
- Song, P., Yang, Y., Barnes-Davies, M., Bhattacharjee, A., Hamann, M., Forsythe, I. D., Oliver, D. L., & Kaczmarek, L. K. (2005). Acoustic environment determines phosphorylation state of the Kv3.1 potassium channel in auditory neurons. *Nature Neuroscience*, 8(10), 1335–1342. <https://doi.org/10.1038/nn1533>
- Spitzer, M. W., & Semple, M. N. (1995). Neurons sensitive to interaural phase disparity in gerbil superior olive: Diverse monaural and temporal response properties. *Journal of Neurophysiology*, 73(4), 1668–1690. <https://doi.org/10.1152/jn.1995.73.4.1668>
- Street, K., Risso, D., Fletcher, R. B., Das, D., Ngai, J., Yosef, N., Purdom, E., & Dudoit, S. (2018). Slingshot: Cell lineage and pseudotime inference for single-cell transcriptomics. *BMC Genomics*, 19(1). <https://doi.org/10.1186/s12864-018-4772-0>
- Trapnell, C., Cacchiarelli, D., Grimsby, J., Pokharel, P., Li, S., Morse, M., Lennon, N. J., Livak, K. J., Mikkelsen, T. S., & Rinn, J. L. (2014). The dynamics and regulators of cell fate decisions are revealed by pseudotemporal ordering of single cells. *Nature Biotechnology*, 32(4). <https://doi.org/10.1038/nbt.2859>
- Tritsch, N. X., Yi, E., Gale, J. E., Glowatzki, E., & Bergles, D. E. (2007). The origin of spontaneous activity in the developing auditory system. *Nature*, 450(7166), 50–55. <https://doi.org/10.1038/nature06233>
- van Hoesel, R. J. M., & Tyler, R. S. (2003). Speech perception, localization, and lateralization with bilateral cochlear implants. *The Journal of the Acoustical Society of America*, 113(3). <https://doi.org/10.1121/1.1539520>
- Vogel, C., De Sousa Abreu, R., Ko, D., Le, S. Y., Shapiro, B. A., Burns, S. C., Sandhu, D., Boutz, D. R., Marcotte, E. M., & Penalva, L. O. (2010). Sequence signatures and mRNA concentration can explain two-thirds of protein abundance variation in a human cell line. *Molecular Systems Biology*, 6. <https://doi.org/10.1038/msb.2010.59>

- Vogel, C., & Marcotte, E. M. (2012). Insights into the regulation of protein abundance from proteomic and transcriptomic analyses. *Nature Reviews Genetics*, *13*(4). <https://doi.org/10.1038/nrg3185>
- Werthat, F., Alexandrova, O., Grothe, B., & Koch, U. (2008). Experience-dependent refinement of the inhibitory axons projecting to the medial superior olive. *Developmental Neurobiology*, *68*(13), 1454–1462. <https://doi.org/10.1002/dneu.20660>
- Yin, T. C. T., & Chan, J. C. K. (1990). Interaural time sensitivity in medial superior olive of cat. *Journal of Neurophysiology*, *64*(2). <https://doi.org/10.1152/jn.1990.64.2.465>
- Yu, F. H., & Catterall, W. A. (2003). Overview of the voltage-gated sodium channel family. *Genome Biology*, *4*(3), 207. <https://doi.org/10.1186/gb-2003-4-3-207>